UNIVERSIDAD DE CHILE
FACULTAD DE CIENCIAS FÍSICAS Y MATEMÁTICAS
DEPARTAMENTO DE FÍSICA

SPATIAL STRUCTURES INDUCED IN A PHOTOSENSITIVE DYE-DOPED NEMATIC LIQUID CRYSTAL CELL

TESIS PARA OPTAR AL GRADO DE
MAGÍSTER EN CIENCIAS, MENCION FÍSICA

LUCCIANO ANTONIO LETELIER CARREÑO

PROFESOR GUÍA::
MARCEL CLERC GAVILÁN

MIEMBROS DE LA COMISIÓN:
KESTUTIS STALIUNAS
MARIO WILSON HERRÁN
MUSTAPHA TDILI
PAULINA HIDALGO CÓRDOVA

SANTIAGO DE CHILE
2024

Resumen

Estructuras espaciales inducidas en una celda fotosensible de cristal liquido nematico dopado con colorante.

El objetivo principal de esta tesis es investigar el efecto de un dopante fotosensible en una mezcla de cristal líquido, particularmente en el acoplamiento que ocurre durante variaciones térmicas o inyección de luz a una frecuencia definida en el material, lo que lleva a la formación de estructuras espaciales. Se realizaron experimentos utilizando microscopía óptica y técnicas láser para inducir las estructuras, y los resultados se compararon con modelos prototipo y universales asociados con cristales líquidos, obteniendo acuerdos cualitativos y cuantitativos con las observaciones experimentales. Se caracterizó la dinámica de las soluciones utilizando herramientas de la física no lineal y simulaciones numéricas.

En el caso de los fenómenos observados bajo interacción con la luz, se diseñó un montaje experimental con láseres. Además, se derivó un sistema de ecuaciones diferenciales parciales basado en los principios fundamentales de los cristales líquidos, incorporando efectos de disipación y absorción de energía para las moléculas del dopante. Posteriormente, se realizó una eliminación adiabática de este sistema acoplado para obtener una ecuación reducida. Se caracterizaron y simularon las bifurcaciones y la estabilidad de las soluciones para el modelo reducido. Esta ecuación ilustra cómo la energía inyectada en el sistema con un haz gaussiano conduce a la generación de patrones anulares a baja potencia de luz y patrones complejos para potencias más altas. También se proporciona una caracterización universal para entender los ingredientes principales para la emergencia y propagación de patrones anulares en un modelo no lineal prototipo.

Para efectos térmicos, la mezcla exhibe separación de fases cerca de la transición de fase, revelando, en el caso del dopante, una segunda fase nemática. El mismo experimento se realizó con una celda de cristal líquido puro, demostrando que también se generan estructuras debido a una dinámica de separación de fases, que conduce a inhomogeneidades en la concentración de moléculas en la mezcla. En este escenario, se derivó un modelo que incorpora los principios de los cristales líquidos y se acopla con una ecuación tipo Cahn-Hilliard que tiene en cuenta cómo se redistribuye la concentración de la mezcla sin un cambio en la masa total con el tiempo. Los resultados experimentales se comparan con el modelo propuesto, obteniendo acuerdos cualitativos y cuantitativos con las observaciones experimentales.

Abstract

Spatial Structures Induced in a Photosensitive Dye-Doped Nematic Liquid Crystal Cell

The main objective of this dissertation is to investigate the effect of a photosensitive dopant on a liquid crystal mixture, particularly in the coupling that occurs during thermal variations or light injection at a defined frequency into the material, leading to the formation of spatial structures. Experiments were conducted using optical microscopy and laser techniques to induce the structures, and the results were compared with prototype and universal models associated with liquid crystals, obtaining qualitative and quantitative agreements with the experimental observations. The dynamics of the solutions were characterized using tools from nonlinear physics and numerical simulations.

In the case of phenomena observed under light interaction, an experimental setup with lasers was designed. Additionally, a system of partial differential equations was derived based on first principles of liquid crystals, incorporating dissipation and energy absorption effects for the dopant molecules. Subsequently, an adiabatic elimination of this coupled system was performed to obtain a reduced equation. The bifurcation and stability of solutions for the reduced model were characterized and simulated. This equation illustrates how the injection energy into the system with a Gaussian beam leads to the generation of ring-like patterns at low light power, and complex pattern for higher powers. Also an universal characterization is given to understand the main ingredients to get emergence and propagation of ring patterns in an prototype nonlinear model.

For thermal effects, the mixture exhibits phase separation near the phase transition, revealing, in the case of the dopant, a second nematic phase. The same experiment was conducted with a pure liquid crystal cell, demonstrating that structures are also generated due to a phase separation dynamics, leading to inhomogeneities in the concentration of molecules in the mixture. In this scenario, a model was derived that incorporates the principles of liquid crystals and is coupled with a Cahn-Hilliard-type equation accounting for how the mixture concentration redistributes without a change in total mass over time. The experimental results are compared with the proposed model, obtaining qualitative and quantitative agreements with the experimental observations.

When you were here before, Couldn't look you in the eye

Acknowledgments

En el cierre de esta significativa etapa de mi vida, siento la necesidad de expresar mi sincero agradecimiento a las personas importantes que han sido parte de mi trayecto, tanto aquellas que continúan a mi lado como aquellas que, por diferentes motivos, ya no lo están.

Quiero agradecer a mi pareja Victoria, a quien amo, por brindarme apoyo en los momentos difíciles de este año, su presencia es fundamental y significativa para mi. A mi mejor amigo Sebastián, agradezco su constante compañía a lo largo de muchos momentos de mi vida. A mis amigos del colegio, que continúan siendo un apoyo sólido. A mis amigos y compañeros tanto de universidad como de carrera, con quienes compartí tanto momentos estresantes como divertidos (muchas anécdotas que con el tiempo aprendimos a disfrutar) durante este período y parte de ellos me han dado un apoyo que no esperaba y fue fundamental en ciertos momentos. Ellos han contribuido a hacer de esta etapa de mi vida una experiencia memorable, y puedo afirmar que fui feliz gracias a ellos.

Expreso mi gratitud a mi tía y a mi nona por el cariño que me han brindado. Un especial agradecimiento a mi gatito Conan por ser mi fiel compañero, acompañándome día y noche en mi rutina diaria.

Además, quiero reconocer y agradecer al profesor Marcel Clerc por su apoyo incondicional y comprensión. No solo es un excelente científico, sino también un mentor excepcional. Aunque a veces disfruta molestando, siempre ha demostrado ser una persona con un gran sentido humano. Cuando necesité consejo, independientemente del tema, él estuvo ahí para ofrecer su orientación.

Quiero agradecer de manera general a los profesores del departamento que me brindaron conocimientos fundamentales en mi trayecto, tanto los que fueron mis profesores de cátedra como con los que tuve el agrado de participar en el mismo equipo docente.

En resumen, agradezco a cada uno de quienes han contribuido de manera significativa a esta etapa de mi vida, cuya presencia y apoyo han dejado huellas imborrables, y estoy feliz por las experiencias compartidas y los momentos vividos juntos.

Table of Content

List of Figures

Chapter 1

Introduction

Throughout human history, our relentless curiosity has driven us to unravel the complex workings of the world around us. At the scale is possible to perceive, various elements come together to form systems constantly exchanging energy. This dynamic interplay gives rise to a multitude of phenomena, such as the orchestrated movements of marine and atmospheric currents influenced by the sun, nurturing the diverse tapestry of vegetation and fauna. Instead of adhering to the limitations of thermodynamic equilibrium, these systems follow the nuanced principles of out-of-equilibrium physics [1, 2, 3]. This dissertation is anchored in the exploration of these intricate dynamics, with a specific focus on the realm of liquid crystal physics [4, 5, 6, 7].

Nature exhibits diverse macroscopic phenomena when systems depart from thermodynamic equilibrium, driven by continuous energy injection and dissipation. These include self-organization examples like ring patterns in bacterial biofilms, wood, spirals in vegetables (e.g., cabbage), and phase separation in liquids with differing densities [8, 9, 10, 11]. Explore these phenomena in Figure 1.1.

Figure 1.1: Illustrative Macroscopic Self-Organization Phenomena: (a) Bacterial biofilm ring pattern [12], (b) Wood cross-section ring structure, (c) Cabbage cross-section with multiple Fibonacci spirals, (d) Oil and vinegar phase separation.

Many of the aforementioned phenomena can be mathematically described using amplitude equations that transcend specific physical systems [13]. This characteristic defines them as robust phenomena, allowing for their replication, observation, and study in the laboratory. The robustness of these phenomena facilitates careful characterization of their dynamical behaviors.

This dissertation delves into two key phenomena: the propagation of ring patterns and phase separation [12, 14, 15, 16, 17, 18]. Recognized as propagative radial waves in optics, vegetation, biological systems, and chemical reactions, these patterns, though previously studied, still harbor unexplored aspects in their emergence and stabilization. Understanding these mechanisms is crucial for effective control in various observed phenomena. Additionally, the phenomenon of phase separation extends from the mixing of polymers and magnetic materials to biological membranes, cellular processes, and colloidal systems, playing a pivotal role across scientific and industrial domains and significantly impacting system stability and properties [19, 20, 21, 22, 23, 24]. This exploration contributes to a broader interdisciplinary understanding of fundamental principles governing diverse systems.

In this dissertation, the investigation focused on the formation of ring patterns and phase separation within the framework of nematic liquid crystals. Nematic liquid crystals represent a unique state of matter that shows characteristics of both liquids and crystals [4, 5, 6]. Notably, these materials exhibit a strong interaction with electromagnetic fields, a property that renders them suitable for the advancement of technological devices, particularly in the development of displays. The exploration of structures in nonlinear media, with a specific emphasis on the context of liquid crystals, holds significant implications for the evolution of technologies in optics and photonics, where liquid crystal devices play a relevant role.

1.1 Dissertation Structure

The present document comprises four chapters and a general conclusion section. The second and third chapters are based on previously published papers, these chapter offers a more detailed and nuanced exploration of the underlying physical phenomena (Appendix A and Appendix B).

The dissertation structure, beginning with Chapter 2, unfolds by thoroughly reviewing fundamental concepts. This chapter delves into theoretical foundations and the establishment of an experimental context. The focus lies on enhancing comprehension within the intricate domains of liquid crystals and nonlinear physics, specifically focused in give enough tools to understand ring patterns and phase separation observations.

Advancing to Chapter 3, presents the examination of two distinct azo-dopant molecules within a Dye-Doped liquid crystal subjected to monochromatic light excitation. This process initiates the formation of radial structures, specifically materializing as ring patterns through photoisomerization phenomena. Furthermore, the chapter seamlessly integrates a theoretical model aimed at deepening the understanding of the observed behavior, drawing insightful comparisons with simulations.

Chapter 4 study the essential components required for emergence and propagation of rings patterns within a nonlinear system. Here, a prototype model is employed, alongside theoretical tools derived from nonlinear physics. The veracity of these findings is validated through simulations, ensuring robustness and reliability in the obtained results.

In Chapter 5, the dynamic closure of the nematic transition in a mixture of liquid crystals is studied. This investigation specifically observes the effect of Dye-dopants in proximity to the transition, and also the dynamics in a Nematic liquid crystal mixture. Notably, two coexisting mechanisms: phase separation and phase transition are identified and meticulously compared with a proposed model.

Finally Chapter 6 encapsulates the main results of the dissertation, presenting the main conclusions drawn from the comprehensive exploration of the aforementioned topics.

1.2 Objectives

The objective of this dissertation is the study and mainly experimental characterization, complemented by theory and simulations, of the photoisomerization phenomena in liquid crystals for different cells and dopants, under the monochromatic light pump and thermal control.

1.2.1 Specific Objectives

The specific objectives of this dissertation were carefully selected to align seamlessly with the main objective, encompassing the following aims:

1. Design experiments to showcase and characterize the formation of patterns, along with spatial and/or temporal effects resulting from photoisomerization induced by light and temperature.
2. Experimentally and theoretically, study the emergence of spatial structures, specifically ring patterns, induced by photoisomerization effects.
3. Check the stability of the experimentally observed ring patterns.
4. Explore, experimentally and theoretically, the equilibria resulting from the interaction between liquid crystal molecules and the dopant.
5. Provide a universal explanation for the occurrence of ring patterns in nonlinear systems.
6. Examine the organization of liquid crystal mixtures when exposed to critical temperatures, and give a theoretical description for this observations..

1.3 Referring and abbreviations

To refer a figure or an equation, in this dissertation, is denoted as:

$$\text{Fig. or Eq.} \quad Chapter.Number,$$

where *Chapter* is the number of the rescpetive chapter and *Number* is the number of the figure/equation in the chapter, for example, Fig. 3.1 refer to the first figure in the chapter 3.

Is important to clarify the abbreviations used in this dissertation are:

1. **LC:** Liquid Crystal.
2. **NLC:** Nematic Liquid Crystal.
3. **DDLCC:** Dye-Doped Liquid Crystal Cell.
4. **NI:** Nematic-Isotropic.
5. **DSC:** Differential Scanning Calorimetry.
6. **DM:** Dichroic Mirror.
7. **CCD:** Charge-Coupled Device.
8. **SH:** Swift-Hohenberg.
9. **CH:** Cahn-Hilliard.
10. **SP:** Spatial Pattern.
11. **PDE:** Partial Differential Equation.
12. **FEA:** Finite Element Analysis.
13. **RK4:** Runge-Kutta Order 4 Method.

Chapter 2

Conceptual Framework

In this chapter main concepts and tools needed are introduced to discuss the topics covered in this dissertation.

2.1 Equilibrium and Stability

Is possible to comprehend the equilibrium of a dynamic system [25], described by the equation

$$\frac{du}{dt} = F(u; \{\sigma_i\}). \tag{2.1}$$

Where $F(u)$ is a well defined function of u and σ_i are the parameters of the system. An equilibrium point u_0 (or steady) is given by

$$\frac{du}{dt}|_{u_0} = 0 \quad \Longrightarrow \quad F(u_0; \{\sigma\}) = 0. \tag{2.2}$$

This equilibrium point is not necessarily unique, and the points u_0 can be divided into two categories: stable or unstable. The point u_0 can be considered asymptotically stable if, for any solution $u(t)$ that starts sufficiently close to u_0, it converges to u_0 as $t \to \infty$. The point u_0 is unstable if the solution u_0 does not converge.
The stability of this solution can be studied by a linear stability analysis around u_0, giving the ansatz

$$u(t) = u_0 + \varepsilon(t). \tag{2.3}$$

where $\varepsilon(t) << 1$, at first order, using this ansatz in Eq. 2.1, having for $\varepsilon(t)$

$$\frac{d\varepsilon}{dt} = \varepsilon \frac{dF}{du}(u_0). \tag{2.4}$$

and the solution to this equation is $\varepsilon(t) = \varepsilon(0)e^{\lambda t}$ with the eigenvalue $\lambda(\{\sigma\}) = (dF/du)(u_0)$. With this, it is easy to see that stability can be defined solely by the sign of the eigenvalue, where if $\lambda > 0$, the solution repels trajectories from the equilibrium point, making it unstable; and conversely, if $\lambda < 0$, it converges to the equilibrium point, making it stable. In the case $\lambda = 0$, stability cannot be directly defined, and nonlinear analysis is necessary to study the dynamics at the equilibrium point.

To generalize this concept in multidimensional systems, examining the case of a system of n equations

$$\frac{du_i}{dt} = f_i(\vec{u}), \tag{2.5}$$

where $\vec{u} = \vec{u}(t)$ is a $n-$dimensional vector where each component u_i is a function of time and f is a $n-$dimensional vector containing functions of $\vec{u}$. An equilibrium point, or steady state $\vec{u}_0$, satisfies $f_i(\vec{u}_0) = 0$ for $i = 1, ..., n$. Similarly to the previous case, is possible to perform a linear stability analisis around $\vec{u_0}$ by writing $\vec{u}(t) = \vec{u_0} + \delta\vec{u(t)}$. The functions $\delta\vec{u}(t)$ obeys, at first order the equation

$$\frac{d\delta u_i}{dt} = \mathbb{J}_{ik}\delta u_k, \tag{2.6}$$

where the term $\mathbb{J}_{ik} = (df_i/du_k)(\vec{u_0})$ is the $ik–th$ element of the Jacobian matrix $\mathbb{J}$. Here, assuming the Einstein notation convention, which is that summation over a index is implicit whenever the index appears twice in a single term. To solve equation postulating that $\delta\vec{u}(t) = \vec{v}e^{\lambda t}$. It follows that λ satisfies

$$(\lambda\mathbb{I} - \mathbb{J})\vec{v} = 0. \tag{2.7}$$

where $\mathbb{I}$ is the identity matrix. The equation as nontrivial solutions only when

$$det(\lambda\mathbb{I} - \mathbb{J}) = 0. \tag{2.8}$$

This equation leads to find the zeros of a polynomial function in λ, which is called the characteristic polynomial of the system. This problem has n complex solutions for λ which can be degenerated or not. Each eigenvalue λ_l has its own associated eigenvector $\vec{v}_l$ which satisfies 2.7. The set $\{\lambda\}_{l=1}^{n}$ is commonly known as the spectrum of the state which can be represented in the complex plane. Then, the perturbations near the state evolve as

$$\delta\vec{u}(t) = \sum_{l=1}^{n} Re(a_l e^{\lambda_l t}\vec{v}_l), \tag{2.9}$$

where $\{a_l\}_{k=1}^{m}$ are constants that must be fixed by the initial condition $\delta\vec{u}(0)$. The information about the stability of a state is contained in the real part of its spectrum, which is related to the temporal growth of the perturbations. Instead, the imaginary part of the spectrum is related with temporal oscillations of the solution. In the case that all eigenvalues have negative real parts, then the steady state is stable and the perturbations decay. If there is an eigenvalue with positive real part, then, the state is unstable and the perturbations diverges exponentially in the direction defined by its respective eigenvector.

2.2 Bifurcations

Bifurcation is a concept in dynamical systems theory that refers to a qualitative change in the behavior of a system as a parameter is varied. In simpler terms, it describes the occurrence of distinct and often dramatic changes in the system's behavior or structure [11].

When a system undergoes bifurcation, it may transition from one stable state to multiple stable states, or it may exhibit chaotic behavior, depending on the specific type of bifurcation that occurs. Bifurcation points are often associated with the emergence of new patterns, oscillations, or equilibrium states in the system[26].

2.2.1 Saddle-node bifurcation

To introduce the concept of bifurcation in a way that is closer to our context, considering a system for a single variable u and parameter r:

$$\frac{du}{dt} = r + u^2. \tag{2.10}$$

This system represents a simple example of a saddle-node bifurcation. Now, analyzing the equilibrium points of the system where $\frac{du}{dt} = 0$ [27]:

$$r + u^2 = 0 \tag{2.11}$$

Solving this equation yields two solutions $u_s = -\sqrt{-r}$ and $u_u = \sqrt{-r}$. Here, u_s and u_u are the solutions corresponding to the and unstable equilibrium points, respectively.

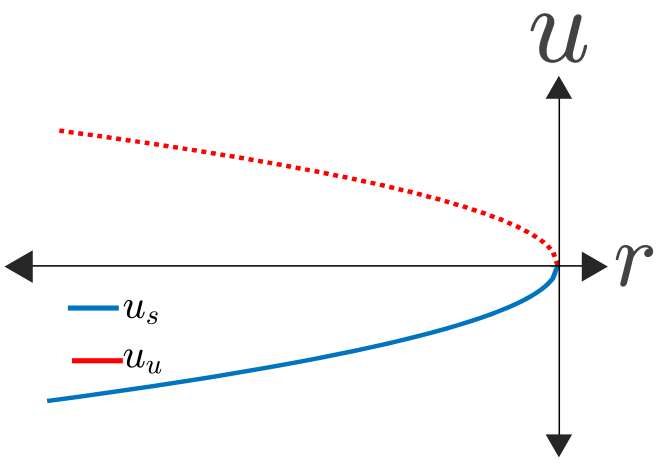

Figure 2.1: Saddle-node Bifurcation: Solid lines represent stable solutions, while dashed lines signify unstable solutions.

Now, examining how these equilibria change as is varied the parameter r. For $r > 0$, the solutions u_s and u_u are complex imaginary numbers, resulting in the absence of real equilibrium points. As r decreases and approaches zero, the solutions u_s and u_u move towards zero.

When $r = 0$, the solutions u_s and u_u coincide at $u = 0$, creating a bifurcation point. This is an example of a saddle-node bifurcation. For $r < 0$, the solutions u_s and u_u become real and opposite. There are now two real equilibrium points: one stable (u_s) and one unstable (u_u).

This scenario represents a saddle-node bifurcation, where the two equilibrium points annihilate at $r = 0$ and then separate in opposite directions as r changes sign as shown in the figure 2.1. This type of bifurcation is characteristic of a saddle-node.

2.2.2 Transcritical Bifurcation

A transcritical bifurcation is a type of phenomenon in the theory of nonlinear dynamical systems, which is a Key component in this dissertation, where the qualitative behavior of the system changes significantly as a parameter varies [11].

In a transcritical bifurcation, two equilibrium points (or stationary solutions) of a system approach each other and exchange stability as the controlling parameter changes.

To better understand this, considering the following simple differential equation that models a transcritical bifurcation, now using u as the variable and parameter r:

$$\frac{du}{dt} = ru - u^2. \tag{2.12}$$

The equilibrium points of the equation are $u_1 = r$ and $u_2 = 0$. When r is negative, the equilibrium point at $u_1 = r$ is unstable, and the system tends to converge towards that point. When r is positive, the equilibrium point at $u_1 = r$ becomes stable, and the system tends to move away from that point.

In the context of a transcritical bifurcation, a noteworthy phenomenon unfolds as the parameter r goes to $r = 0$. The two equilibrium points $u_1 = r$ and $u_2 = 0$ dynamically converge, ultimately undergoing a switch in their stability characteristics, illustrated in Figure 2.2. Post-bifurcation, the equilibrium point the stable solution change into an unstable state, while the other solution experiences a reciprocal alteration.

The implications of this bifurcation type resonate deeply within the realm of dynamical systems, imparting a profound impact on diverse natural phenomena and mathematical models. The intricate dance of stability exchange showcased in transcritical bifurcation adds a layer of complexity and richness to our understanding of dynamic systems.

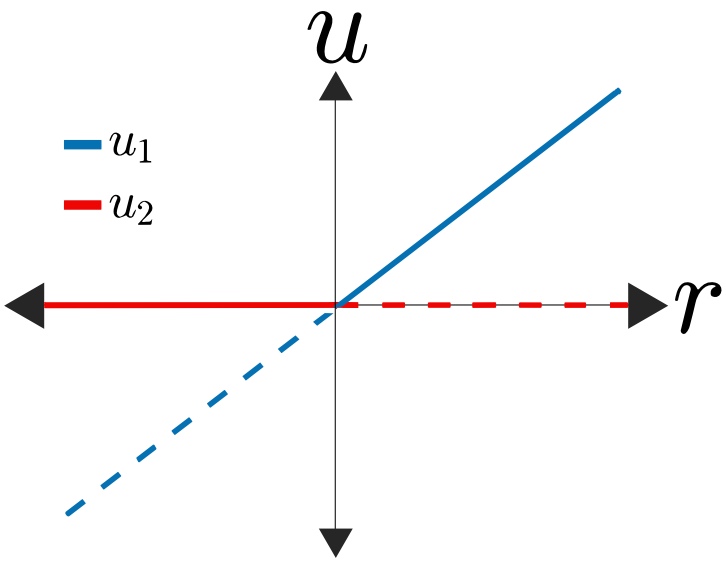

Figure 2.2: Transcritical Bifurcation: Solid lines represent stable solutions, while dashed lines signify unstable solutions.

2.2.3 Pitchfork Bifurcation

A Pitchfork bifurcation involves an instability of a equilibrium while a pair of states is created or destroyed. There are two cases of Pitchfork bifurcation, supercritical and subcritical case [11].

Supercritical Bifurcation

As a simple example of a supercritical bifurcation is the following differential equation.

$$\frac{du}{dt} = ru - u^3. \tag{2.13}$$

Here, u is the state variable, and r is a parameter. This equation represents a simplified model that exhibits a supercritical bifurcation. When $r < 0$, the only solution to this equation is $u_0 = 0$, which is a stable equilibrium point. However, as $r = 0$, a bifurcation occurs.

The supercritical bifurcation manifests because, after crossing the bifurcation point, the stable equilibrium at $u_0 = 0$ loses stability in a smooth manner. The differential equation can be rewritten as:

$$\frac{du}{dt} = (r - u^2)u. \tag{2.14}$$

Now, there are two possible equilibria: $u_0 = 0$ (unstable) and $u_\pm = \pm\sqrt{r}$ (stable for $r > 0$. This smooth transition from a single stable equilibrium to two stable equilibria is characteristic of a supercritical bifurcation.

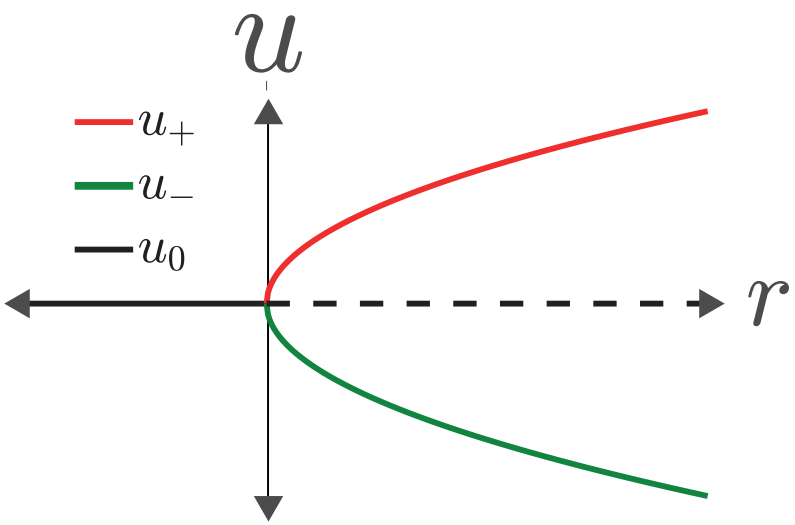

Figure 2.3: Supercritical Bifurcation: Solid lines represent stable solutions, while dashed lines signify unstable solutions.

In a nutshell, a supercritical bifurcation in physics denotes a smooth and significant transition within a system. When the linear parameter r change, the system shifts from a state of stable equilibrium to a configuration showing multiple stable equilibria.

Subcritical Bifurcation

Contrary to supercritical bifurcation, subcritical bifurcation involves a different dynamic transition in a system. The following differential equation serves as an illustration of a subcritical bifurcation:

$$\frac{du}{dt} = ru + u^3. \tag{2.15}$$

Similar to the supercritical example, here, u is the state variable, and r is a parameter. In this subcritical case, when $r < 0$, the only stable solution to the equation is $u_0 = 0$. However, the behavior changes significantly as r becomes positive.

After crossing the bifurcation point at $r = 0$, a subcritical bifurcation results in the destabilization of the previously stable equilibrium at $u_0 = 0$. The differential equation can be reformulated as:

$$\frac{du}{dt} = (r + u^2)u. \tag{2.16}$$

Now, the equilibrium at $u_0 = 0$ becomes unstable, and two new stable equilibria emerge at $u_\pm = \pm\sqrt{-r}$ for $r > 0$. This transition from a single stable equilibrium to two stable equilibria characterizes a subcritical bifurcation.

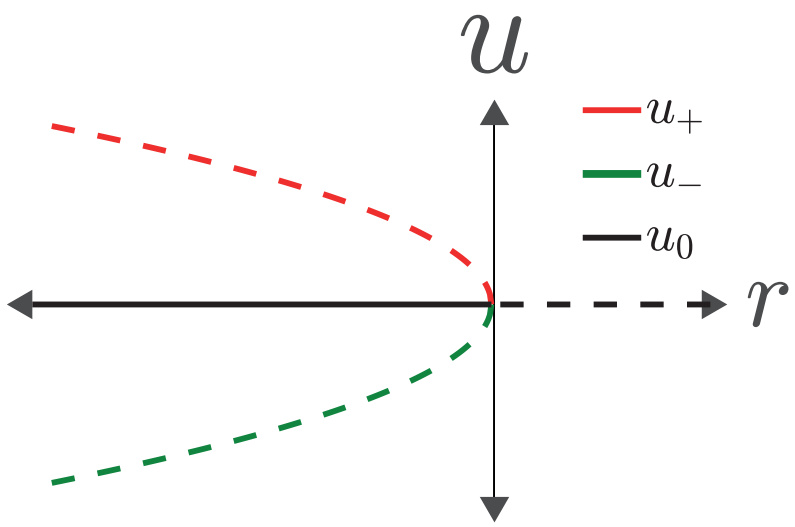

Figure 2.4: Sub Bifurcation: Solid lines represent stable solutions, while dashed lines signify unstable solutions.

In summary, a subcritical bifurcation in physics signifies a sudden and significant transformation within a system as a parameter is adjusted. This adjustment leads the system from a state of stable equilibrium to a configuration with multiple stable equilibria, distinguishing it from the smooth transition observed in a supercritical bifurcation.

This phenomenon is discernible through the gradual evolution of the system's behavior. As the relevant parameter undergoes systematic changes, the system smoothly traverses various states, each characterized by distinct and stable equilibria.

2.3 Spatial Instabilities in Homogeneous Phases

In order to understand complex system, is necessary to use partial differential equations (PDEs), this equations let study n^{th} dimensional systems. In this systems spatial instabilities within homogeneous phases shows complex phenomena where uniformity gives way to the emergence of intricate patterns or structures [11]. This section delves into a rigorous exploration of spatial instabilities, with a primary focus on the Swift-Hohenberg equation as an analytical tool [28, 29]. This equation is a fourth-order partial differential equation:

$$\frac{\partial u}{\partial t} = ru - (1 + \nu\nabla^2)^2 u - \beta u^3. \tag{2.17}$$

Here, u represents the scalar field denoting deviations from the homogeneous state, r is a linear parameter, and ν is associated to the diffusion, is possible to notice that $u = 0$ is solution. Assuming a small perturbation $u = \varepsilon e^{i(kx-\omega t)}$ around the solution $u = 0$, where the amplitude $\varepsilon << 1$ allows to avoid the non-linear terms. Substituting the perturbation into the Swift-Hohenberg equation and linearizing, is obtained a dispersion relation in terms of ε and ω:

$$\omega = r - (1 + \nu k^2)^2. \tag{2.18}$$

This represents the growth rate of the perturbation when $Re(\omega) > 0$. Instability arises from the condition $d\omega/dk(k_c) = 0$ that gives the critical values $k_c = \pm\sqrt{\nu}$. Replacing the k_c in the condition $\omega(k_c) = 0$ the dispersion relation provides insights into the critical values of r_c where instability initiates, in particular if the system have a intrinsic wavelength, this spatial instability is called Turing instability [30]). Determining the critical value $r_c = 0$ involves finding the threshold where the dispersion relation becomes positive. This threshold signifies the transition from a stable to an unstable homogeneous state.

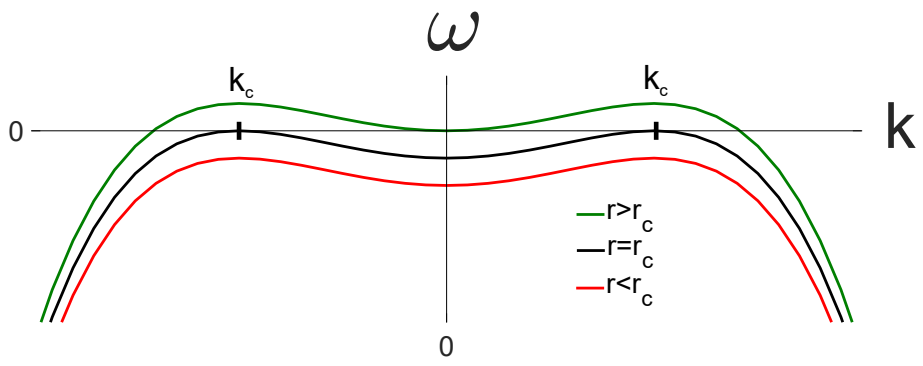

Figure 2.5: Dispersion relation for Swift-Hohenberg model around r_c.

2.4 Pattern Formation & Amplitude equation

To comprehend the mechanism of pattern formation, modal theory is employed when a spatial instability (specifically, Turing instability) emerges [10]. This discussion utilizes the Swift-Hohenberg equation (Equation 2.17). Notably, considering that $r_c = 0$ represents an instability, it becomes possible to derive an amplitude equation around this critical point. For simplicity, assuming only a single mode with wave number is $k_c = 1$ (calculated in the previous section), and employ the following ansatz:

$$u \approx A(T)\, e^{ix} + \text{c.c.} + \text{h.o.t.} \tag{2.19}$$

Here, A is a complex variable, and $T = |r|t$ represents the slow variable, where $\frac{dT}{dt} = |r|$. Applying this ansatz to the Swift-Hohenberg equation and taking the dominant order e^{ix} while uncoupling A and its complex conjugate, is obtained the following amplitude equation:

$$\frac{dA}{dt} = r\, A - 3\beta\, A\, |A|^2 \tag{2.20}$$

This amplitude equation exhibits two distinct behaviors based on the sign of the linear parameter, which is binary in the context of the amplitude equation (although continuous in the original equation). Specifically, The solutions of this amplitude equation for any value of r follows:

$$A_\pm = \pm\sqrt{\frac{r}{3\beta}} \qquad \& \qquad A_0 = 0 \tag{2.21}$$

If $r = 0$, the system undergoes a supercritical bifurcation (or subcritical if $\beta < 0$). For $r > 0$ the stable solutions are $A_\pm$, while A_0 is unstable. On the other hand, if $r < 0$, $A_\pm$ disappear, and A_0 becomes the stable solution (the stability exchange if $\beta < 0$).

It is crucial to note that the instability of a single mode does not necessarily imply the absence of pattern formation. Even when individual modes are unstable, the emergence of stable multimode patterns is a possibility. These multimode patterns can effectively connect and stabilize the individual mode solutions, contributing to the overall pattern formation process.

This analysis provides insights into the bifurcation behavior of the system, offering a deeper understanding of the pattern formation.

2.5 Maxwell Point

The study of free energy is used understand some variational systems [31]. To comprehend the Maxwell point, it becomes imperative to employ a representative model, encapsulated by the following differential equation:

$$\frac{du}{dt} = \frac{d^2u}{dx^2} - \frac{\delta V}{\delta u}. \tag{2.22}$$

In this context, the Maxwell point materializes through the qualitative change of the potential energy function $V(u;\{\lambda\})$ along with its parameters. An example of such a model is given by:

$$V(u) = -\varepsilon u - \frac{u^2}{2} + \frac{u^4}{4}. \tag{2.23}$$

Here, the free energy assumes the form of a fourth-order polynomial, leading to a transition at the Maxwell point characterized by a shift between the value of two local minimum potential . The critical value marking this transition in the presented example is calculated when $V(u_1) = V(u_2)$ where u_1 and u_2 are potential minimum, giving the Maxwell point :

$$\varepsilon_M = 0 \tag{2.24}$$

To visualize this intriguing transition, Figure 2.6 depicts the Maxwell point with this fourh-order potential example.

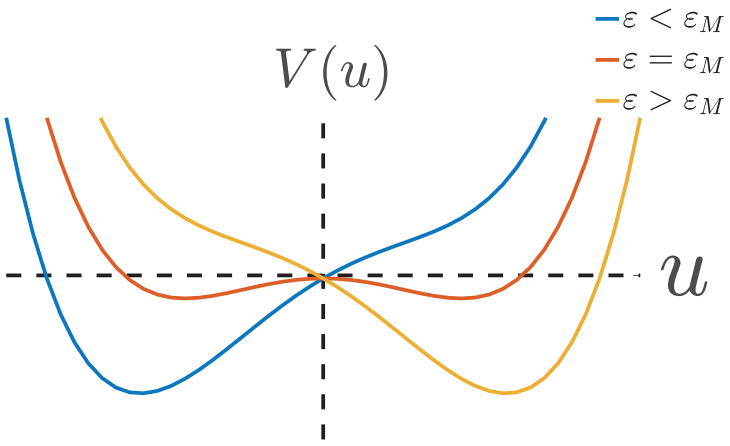

Figure 2.6: Maxwell point transition for a fourth order potential.

As illustrated in Figure 2.6, the free energy landscape surrounding the Maxwell point showcases the coexistence of competing non-symmetric stable solutions and the shift in the global minimum potential. This dynamic interplay underscores the intricate behavior inherent in variational systems.

2.6 Liquid Crystals

Liquid crystals (LC) is an interesting state of matter. In addition to the solid crystalline and liquid phases, liquid crystals exhibit intermediate phases where they flow like liquids, yet posses some heritage properties from crystal structures [4, 5]. In a LC, molecules have a tendency to align in ordered directions, forming regions or domains where molecular orientation is relatively uniform.
In particular in this dissertation is studyied phenomena related to Nematic Liquid Crystals (NLC). As a matter of fact, NLC is the best example of dual nature when is refering to LC.

2.6.1 Order Parameter

The physics of LC can be described in terms of the order parameter. Using the main axis of the molecule (considering a preferential direction in the molecular structure) as a reference and denote it as $\hat{k}$ (Fig. 2.7), the microscopic scalar order parameter S is defined as follows:

$$S = \frac{1}{2}\left\langle 3(\hat{k}\cdot\hat{n})(\hat{k}\cdot\hat{n}) - 1\right\rangle = \frac{1}{2}\left\langle 3cos^2\theta - 1\right\rangle . \tag{2.25}$$

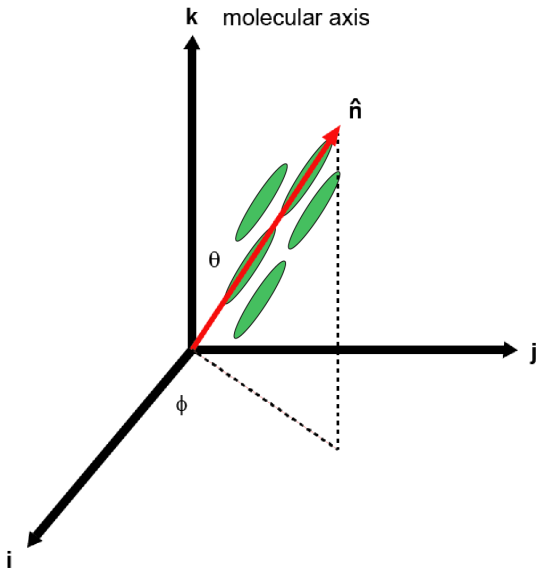

Figure 2.7: Coordinate system for a LC Molecule

The order parameter can be translated into expressions of the energy in terms of the anisotropies in the physical parameters such as magnetic, electric, and optical susceptibilities.
This parameter is an average over a considerable region and provides a measure of the long-range orientation order. The smaller fluctuation of the molecular axis from the director, means that S represent a well aligned LC, that means $S = 1$; on the other hand, in a perfect isotropic system (for example as a liquid), the alignment is expected to be random for the molecules, so the order parameter value is $S = 0$.
An important characteristic of this parameter is that show critical dependences as the temperature approaches the phase transition temperature T_c from the respective directions [4, 5].

2.6.2 Planar Anchoring

A relevant concept employed in the experimental setup of this research is planar anchoring, where the molecules of a liquid crystal exhibit a preferential alignment parallel or tangential to a substrate or surface. This alignment direction is typically established through specific treatments applied to the substrate, such as rubbing or coating with alignment layers, and is referred to as the rubbing direction.

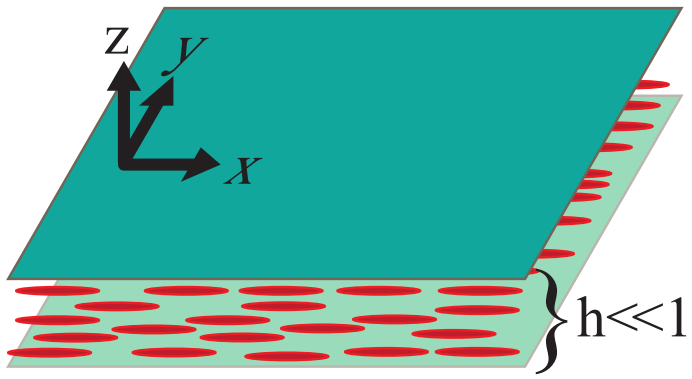

Figure 2.8: Diagram illustrating Planar Anchoring in a sample with a width smaller than the dimensions of the surface [32].

The preferred alignment direction, often referred to as the rubbing direction, is induced by treatments applied to the substrate. For instance, rubbing the substrate in a specific direction imparts a preferred alignment to the liquid crystal molecules. Additionally, coatings or alignment layers deposited on the substrate contribute to the anchoring effect.

The anchoring of liquid crystal molecules at the substrate surface holds critical significance for the effective operation of liquid crystal devices, notably in applications like liquid crystal displays (LCDs). The orientation of liquid crystal molecules significantly influences the optical properties of the material, and precise control over this alignment allows for the attainment of specific optical effects.

It is noteworthy that various anchoring conditions exist, with planar anchoring being just one of them. Other anchoring conditions, such as homeotropic anchoring, or twisted anchoring, contribute to the diverse ways in which liquid crystal materials can be manipulated to achieve desired functionalities in different applications.

2.6.3 NLC & Isotropic Phases

To understand the behavior of a NLC system is necessary to observe the different configurations of molecules.
When is studied the order parameter in each phase, how was mentioned in the previous subsection, the order parameter change when the distribution of the direction change, being $S = 1$ when is perfectly aligned and $S \approx 0$ for a random distribution. In order to this is possible to represent the isotropic phase when having a disordered system (random directions) and a NLC phase when $S \approx 1$, i.e. the system presents some directional order

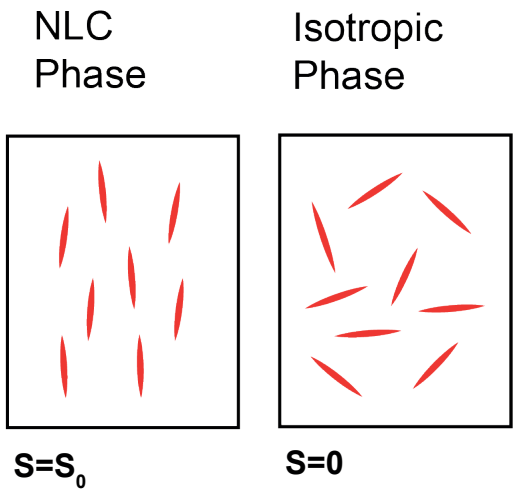

Figure 2.9: Alignment for NLC and Isotropic Phases; $S_0 > 0$ indicates a preferential orientation order in the NLC phase.

To elucidate the phase transition between these two states and the order parameter's behavior in proximity to T_c (this is a first order transition), physical models have been employed. In these models, Liquid Crystal (LC) molecules are treated as rigid rods, exhibiting correlation through electrical interactions. This approach facilitates a comprehensive understanding of the intricate behaviors exhibited by the system near the critical temperature (T_c).

2.6.4 E7 Liquid Crystal

The E7 nematic liquid crystal mixture, employed as the matrix in the presented experiments, is composed of cyanobiphenyl and cyanoterphenol components in a specific composition (Figure 2.10). This formulation imparts notable characteristics to the liquid crystal, as high birefringence and positive dielectric anisotropy .

As previously mentioned, liquid crystals undergo a Nematic-Isotropic transition. In the case of E7, this transition occurs at a temperature of $63.3°C$, while the isotropic-nematic transition takes place at $61.0°C$ [33, 34]. Notably, there is a hysteresis with respect to the critical temperature, a phenomenon quantified through Differential Scanning Calorimetry (DSC) as depicted in Figure 2.11.

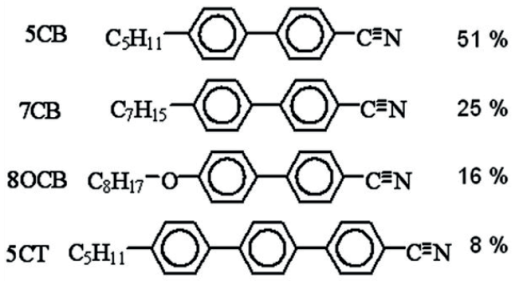

Figure 2.10: Molecular structure of the components of E7 liquid crystal from Merck [33, 34].

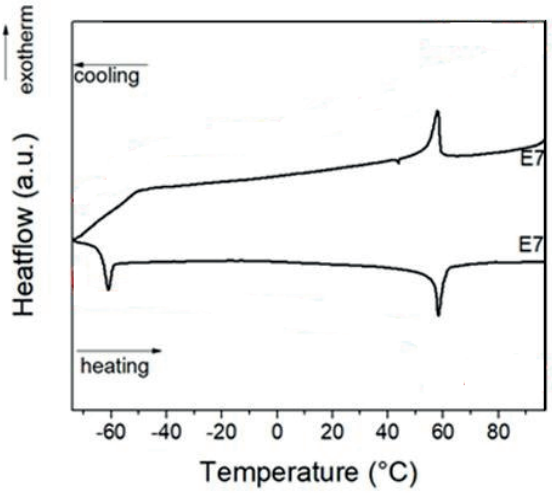

Figure 2.11: Differential Scanning Calorimetry of E7 liquid crystal [33, 34, 35].

This DSC analysis provides valuable insights into the thermal behavior of E7, specifically highlighting the temperature range associated with phase transitions. The hysteresis observed in the DSC curve underscores the significance of carefully characterizing the thermal properties of liquid crystals..

2.6.5 Landau-DeGennes Model

To study the transition from a nematic to an isotropic phase, it is imperative to analyze the free energy within the continuum Landau-de Gennes theory. The free energy is expressed as a series expansion in powers of the nematic order parameter $S = S(x, y, t)$, as outlined by deGennes [4]:

$$F_1 = AS^2 - BS^3 + S^4. \tag{2.26}$$

Here, the parameters A and B play a crucial role in characterizing the transition, where $A \propto (T - T_c)$. Additionally, a component accounting for the interaction between molecules is introduced to the energy:

$$F_2 = (\nabla^2 S)^2. \tag{2.27}$$

Consequently, the total energy is described as the sum of these contributions:

$$F = AS^2 - BS^3 + S^4 + (\nabla^2 S)^2. \tag{2.28}$$

In the context of a dynamic system, the following variational equation describe the temporal evolution of the order parameter:

$$\frac{dS}{dt} = -\int_V \frac{\partial F}{\partial S} dV. \tag{2.29}$$

Here, the continuous order parameter is considered over a substantial volume, facilitating the exploration of local dynamics in space. This variational equation yields the following expression:

$$\frac{dS}{dt} = -AS + BS^2 - S^3 + \nabla^2 S. \tag{2.30}$$

It is noteworthy that this model predicts the nematic-isotropic transition as a subcritical bifurcation. Furthermore, the last term in the equation accounts for the diffusion process.

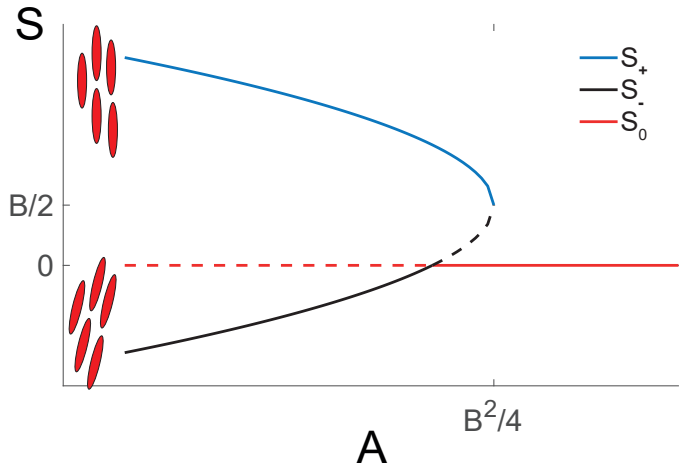

Figure 2.12: Bifurcation Diagram illustrating solution stability: Continuous lines denote stability, while dashed lines indicate instability. $S = 0$ corresponds to the isotropic solution, while S_+ and S_- represent the nematic phases.

The solutions presented in Figure 2.12 have been described in prior studies, providing insights into the stability of isotropic and nematic states within a typical nematic liquid crystal system [4, 5]. This diagram illustrates the general stability of a nematic liquid crystal (NLC) system, revealing a subcritical transition defined by the parameter B. The solutions S_+ and S_- exist only when $A < B^2/4$ showing a saddle-node bifurcation, while the transition between $S = 0$ and S_- corresponds to a subcritical transition.

2.7 Photoisomerizable Dopant

A important topic in this dissertation is about the use of a photoisomerizable molecule, that refers to a substance or material that can undergo isomerization (a change in its molecular structure) when exposed to light [36]. In the context provided earlier, a "photoisomerization" involves a change in molecular structure induced by light, typically leading to observable effects in a liquid crystal system [5].
Two different azo molecules were studied, Methyl-Red (Sigma-Aldrich Inc., St. Louis, MO, USA), and Methyl-Red-Methyl-Ester (synthesized by Paulina Hidalgo and Jorge Vergara, University of Concepcion, Chile) [37, 38].

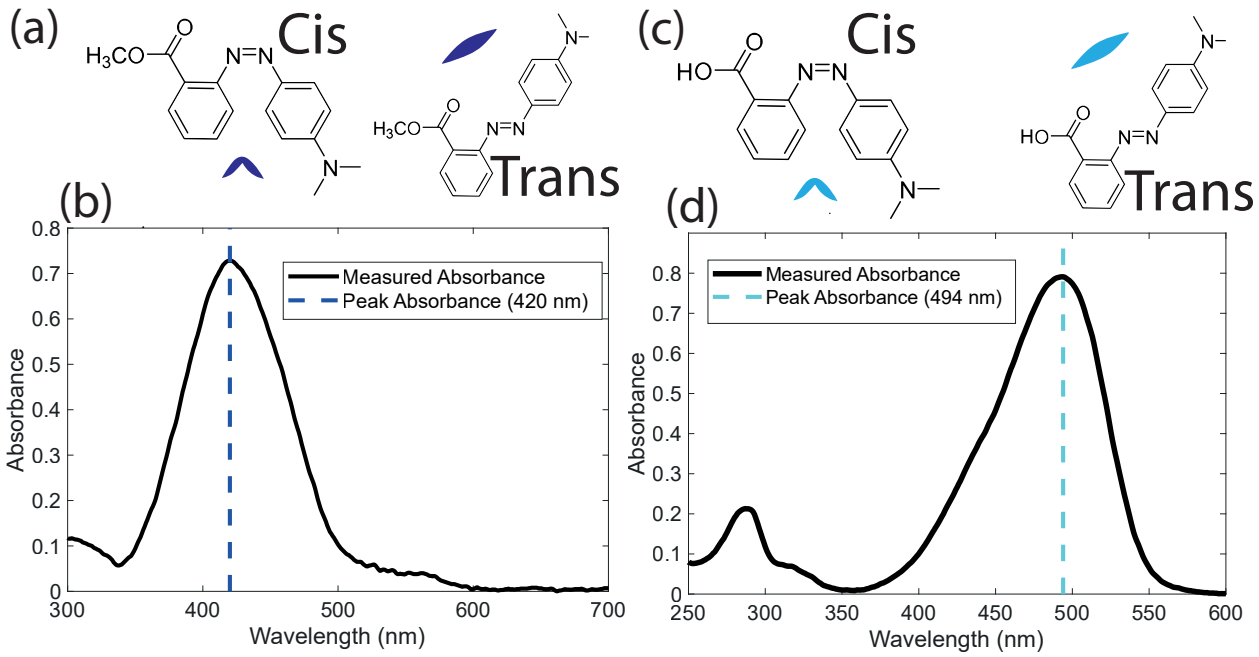

Figure 2.13: Dopant molecules configuration and absorbance spectrum methyl-red-methyl-ester (a),(b) and methyl-red (c),(d).

In Figure 2.13 is illustrated a representation of the molecular configuration of each dopant in (a) and (c), where is showed the Cis and Trans states (left and right respectively). Also is showed the absorbance spectrum for each one (b) and (d), noticing that the maximum absorption is at 420 nm for methyl-red-methyl-ester and 494 nm for methyl-red.
It is crucial to emphasize that the transition between both states is reversible. This implies that, through heat fluctuations, molecules have the capability to revert to the original trans state [36].

2.7.1 Dopant transition model

The azo-dopants in general are the main ingredient in this experiment, because the trans state is possible to be miscible in the mixture, that allow to conserve the NLC..

As depicted in Figure 2.13(a)(c), azo-dopants exhibit two distinct states, namely trans and cis states. Understanding the role of these dye-dopants necessitates delving into the concentration of molecules in the cis state, denoted as $C(x, y, t)$. This emphasis on the cis state stems from the observation that the trans state molecule shares a structural similarity with the nematic liquid crystal form, contributing to a lack of disorder. In the other hand, the cis state, characterized by its boomerang form, induces disorder in the surrounding molecular environment as result of molecular interaction.

The concentration $C(x, y, t)$ satisfies a relaxation and diffusion equation, capturing the intricate dynamics of the system. This equation takes the form [36]

$$\frac{dC}{dt} = -\lambda[C - C_0(I)] + \delta\nabla^2 C. \tag{2.31}$$

In the context of the transition from the trans to cis state, the parameter λ characterizes the decay rate. The steady state concentration $C_0 = C_0(T, I)$ of the cis state is dependent of temperature and intensity of the incident beam, denoted as I. The diffusion coefficient of the concentration of molecules in the cis state is represented by δ. The model for the steady concentration is [36].

$$C_0 = C_T + \frac{\gamma I}{1 + \eta I}. \tag{2.32}$$

Here, γ and η are dimensional parameters, and C_T signifies the equilibrium concentration of molecules in the cis state at temperature T. Notably, the concentration C_0 exhibits linear growth with light intensity for small intensities. However, it saturates at $C_T + \gamma/\eta$ for higher intensities, revealing an intriguing behavior in response to varying light conditions.
The inclusion of dye-dopants increases the nonlinear response of liquid crystals under the excitation of external fields [36, 39, 40, 41, 42, 43].

In general the I shape, for a laser is a Gaussian beam, that means:

$$I(r) = I_0 e^{-r^2/w^2}. \tag{2.33}$$

Where I_0 is the laser intensity in the central part, and w is the laser weist.

2.8 Onsager Reciprocal Relations

Onsager reciprocal relations [44] emerge from the fundamental principle that the equations governing irreversible processes should remain unchanged under time reversal. In a system featuring two conserved quantities, namely x_1 and x_2, with associated fluxes denoted as J_1 and J_2, the reciprocal relations take the form:

$$\begin{aligned} J_1 &= L_{11}\nabla x_1 + L_{12}\nabla x_2, \\ J_2 &= L_{21}\nabla x_1 + L_{22}\nabla x_2. \end{aligned} \tag{2.34}$$

Here, L_{ij} signifies the coefficients of interaction between the two systems. When each system manifests its distinct dynamics, the interaction between them can be articulated through the following expressions ($i \in \{1, 2\}$):

$$\begin{aligned} \frac{dx_1}{dt} &= -\frac{\delta F}{\delta x_1}(x_i, \nabla x_i) + \nabla J_1, \\ \frac{dx_2}{dt} &= -\frac{\delta F}{\delta x_2}(x_i, \nabla x_i) + \nabla J_2. \end{aligned} \tag{2.35}$$

Where F represent the free energy of the system, and L_{11} and L_{22} stand for self-interaction terms. In scenarios involving reciprocal interaction between the systems (characterized by $L_{12} = L_{21} = D$) and the absence of self-interaction within each system ($L_{11} = L_{22} = 0$), the equations can be recast as, replacing 2.34 in 2.35 :

$$\begin{aligned} \frac{dx_1}{dt} &= -\frac{\delta F}{\delta x_1}(x_i, \nabla x_i) + D\nabla^2 x_2, \\ \frac{dx_2}{dt} &= -\frac{\delta F}{\delta x_2}(x_i, \nabla x_i) + D\nabla^2 x_1. \end{aligned} \tag{2.36}$$

These relations not only provide insights into the dynamics of interacting systems but also underscore the elegance of Onsager's reciprocal principles in understanding the behavior of conserved quantities and associated fluxes.

2.9 Adiabatic Elimination

Adiabatic elimination serves as an efficient method for simplifying complex systems, offering researchers a valuable tool to focus on the most relevant dynamics [45]. However, ensuring the fidelity of the approximation is paramount. Rigorous assessment of the validity of the approximation is necessary to ascertain that the simplified model accurately represents the intricate behavior of the original system within the specified timescales. This involves meticulous consideration of the chosen small parameter ε and a thorough examination of the separation of timescales to guarantee the reliability of the adiabatic approximation. Only through this careful evaluation can researchers confidently proceed with the simplified model, confident that it faithfully captures the essential features of the original system.

To delve into this concept, consider a system of equations featuring a fast variable x and a slow variable y:

$$\begin{aligned} \frac{dx}{dt} &= -\varepsilon(x + sin(t)), \\ \frac{dy}{dt} &= x^2 - y. \end{aligned} \tag{2.37}$$

Here, $\varepsilon >> 1$ serves as a large parameter, signifying the separation of timescales. Notably, x slow responds to the term $-\varepsilon x$, while y evolves faster.

To apply adiabatic elimination, it is imperative to first identify fast and slow variables. In this case, x is the slow variable, and y is the fast variable. Subsequently, assuming ε is sufficiently large to warrant a distinct separation of timescales, leading to $x = -\sin(t)$.

Upon substituting this adiabatic approximation into the equation for y, the resulting reduced equation takes the form:

$$\frac{dy}{dt} = \sin^2(t) - y.$$

The adiabatic elimination remains valid when ε is large, justifying the separation of timescales.

In summary, the application of adiabatic elimination empowers the elimination of the slow variable x, yielding a simplified equation for the fast variable y. This technique proves particularly valuable in systems marked by distinct timescales.

2.10 Phase Separation

In the materials science, phase separation stands out as a captivating phenomenon that unfolds when a system experiences shifts in its environmental conditions, be it alterations in temperature, pressure, or composition. This dynamic process gives rise to the spontaneous coexistence of distinct regions or phases within the material, each characterized by its physical properties or molecular arrangements [19].

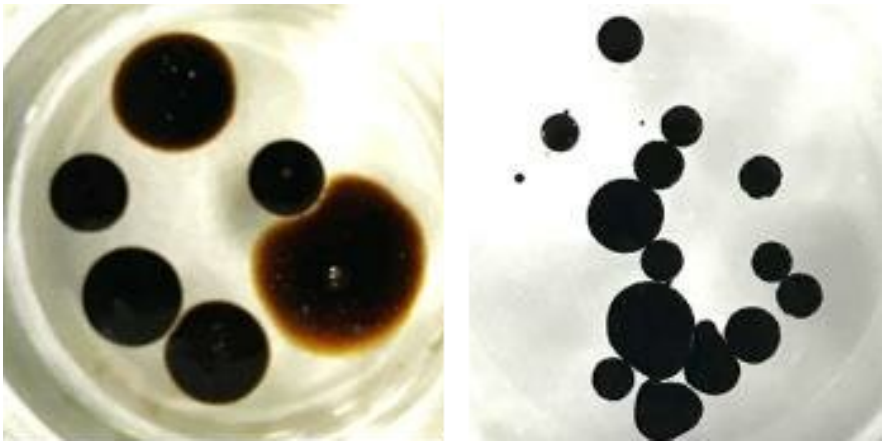

Figure 2.14: Phase separation of oil-water system, the red represents the oil and the blue is water. Oil droplets in pure water and oil droplets in water containing surfactant (left and right respectively) [46].

The nature of phase separation exhibits variability, presenting different types based on the characteristics of the separating phases. In certain instances, the separation may result in the creation of distinct layers, while in others, the phases may coexist in a dispersed manner throughout the material. A nuanced understanding of these variations becomes imperative for predicting and interpreting the behavior of materials under different conditions.

As phase separation progresses, it often culminates in the formation of intricate patterns and structures within the material. These patterns, ranging from simple domain formations to complex configurations, depend on the specific properties of the material and the conditions dictating the phase separation process. The observation and characterization of these patterns yield valuable insights into the underlying material dynamics. A prototype model to understand this behaviour is the Cahn-Hilliard equation (CH) [47], this explain the coexistence of two domains.

2.11 Cahn-Hilliard Equation

The Cahn–Hilliard equation, introduced by Cahn and Hilliard in 1958 [47], serves as a fundamental model for understanding phase separation dynamics, revealing distinct domains within a fluid. If N denotes the concentration of the metal alloy, the equation is expressed as:

$$\frac{dN}{dt} = D\nabla^2\mu(N) = -D\nabla^2\frac{\delta F}{\delta N}, \tag{2.38}$$

where D is the diffusion coefficient and $\mu(N)$ represents the chemical potential defined by the variation of free energy:

$$\mu(N) = -\frac{\delta F}{\delta N} = -N + N^3 - \gamma^2\nabla^2 N, \tag{2.39}$$

Here, the parameter γ delineates the length of transition regions between domains. The evolution of the concentration field N over time is governed by the partial differential equation:

$$\frac{dN}{dt} = -D\nabla^2\left(N - N^3 + \gamma^2\nabla^2 N\right). \tag{2.40}$$

The Cahn–Hilliard equation adopts a conservation law form, with $\mathbf{J}$ the energy flux, signifying the preservation of total concentration:

$$\frac{dN}{dt} = -\nabla\cdot\mathbf{J} \quad \text{with} \quad \mathbf{J} = D\nabla\mu. \tag{2.41}$$

This conservation law implies the constant total concentration N_0, defined as:

$$N_0 = \int_V N(\vec{r}, t)\, dV. \tag{2.42}$$

In scenarios where one phase dominates, the Cahn–Hilliard equation may exhibit Ostwald ripening, a phenomenon where the minority phase forms spherical droplets. These smaller droplets undergo absorption through diffusion into the larger ones, resulting in distinctive morphological changes in the system [48, 49].

An intriguing observation associated with the Cahn–Hilliard equation is the growth of segregated domains over time, following the Lifshitz–Slyozov law [48, 50]. If $L(t)$ represents a typical domain size at time t, then the relationship $L(t)\propto t^{1/3}$ characterizes the evolution of these domains. This power-law growth provides valuable insights into the temporal behavior of phase separation in systems described by the Cahn–Hilliard equation.

2.12 Finite Element Analysis

This section aims to elucidate the algorithm employed in the FlexPDE program, which serves as the simulation tool in this research [51].

Fundamental concept behind finite element analysis (FEA) involves partitioning the domain of interest into sub-regions or cells of simple shapes and solving the equations concurrently within each of these regions. In the adaptive method, the domain is subdivided into triangles or prisms with triangular cross-sections adjusting the nodes each iteration to improve the calculus. Notably, cells in contact with the boundary might feature slightly curved outer sides, and the cells displayed on the screen represent projections of the prisms onto the viewing plane.

The simulation aims to solve partial differential equations (PDEs) by determining the values of dependent variables at discrete points or nodes—specifically, at the corners of the triangles and the midpoints between corners. The solution process results in a record of values exclusively at these nodes. To extrapolate function values and derivatives at other points within a triangular cell, the program employs an interpolation algorithm [52].

2.12.1 Interpolating to Obtain a Solution

Once the simulation has produced a solution, it stores it in a table where the values of the dependent variable (or variables) are given for each node point. To compute the solution at any point in space the program interpolates this table by a quadratic algorithm. The procedure involved in this interpolation is simple. For each triangular region the program uses a polynomial of the following form

$$P(x, y) = a_0 + a_1 x + a_2 y + a_3 xy + a_4 x^2 + a_5 y^2. \tag{2.43}$$

Function values are known at three corners and three midpoints, a total of six points, corresponding exactly to the number of coefficients in $P(x, y)$. In order to determine the coefficients a a_i the method just solves a system of six linear equations.

2.12.2 Nodes values

In FEA, knowing the node values of the dependent variables is equivalent to having a solution to the problem. If the dependent variables are known at all the nodes of the grid, interpolating to obtain values at any point of the solution domain and also differen- tiate the polynomials to obtain derivatives of first and second order. The crucial task of calculating the values pertaining to the nodes is much more difficult than to interpolate the results. A general, linear PDE of second order reads.

$$E_q = \frac{\partial^2 u}{\partial x^2} + f_1 \frac{\partial^2 u}{\partial x \partial y} + f_2 \frac{\partial^2 u}{\partial y^2} + f_3 \frac{\partial u}{\partial x} + f_4 \frac{\partial u}{\partial y} + f_5 u + f_6 = 0. \tag{2.44}$$

where f_k are functions of x, y.If $u(x, y)$ is an exact solution to the PDE, then E_q remains zero over all of the solution domain D. Integrating over this domain also having:

$$\iint_D E_q dx dy = 0. \tag{2.45}$$

It is *not* true, however, that a function $u(x, y)$ that satisfies this relation must be a solution: E_q might take positive as well as negative values, which could cancel in the integral. If, on the other hand, taking the square of the PDE, the condition

$$\iint_D E_q^2 dx dy = 0, \tag{2.46}$$

it implies that $u(x, y)$ is a solution. In fact, it is possible to use this relation for solving the equation numerically. For a given PDE, the above integral of E_q^2 may be regarded as a function of the node values.

$$I(u_1, u_2, ..., u_n) = \iint_D E_q^2 dx dy = 0. \tag{2.47}$$

Of course, in view of the limited accuracy of numerical computation could never hope to find a set of node values ui which makes the integral $I(u_1, u_2, ..., u_n)$ exactly equal to zero, so contenting with a set that minimizes the integral. This is equivalent to finding the minimum of a function of many variables, and there are standard methods available for solving this type of problem. The effect of taking the square of E_q , however, is to make the integrand more complicated and also non-linear.

An alternative method, which only involves linear analysis, as long as the PDE itself and its boundary values are linear, proceeds as follows. Instead of condensing the problem into a single integral expression as in the scheme above, now introducing a whole set of equations of the same type (numbered $j = 1, 2, ..., m$):

$$I_j(u_1, u_2, ..., u_n) = \iint_D W_j(x, y) E_q dx dy = 0. \tag{2.48}$$

The equations involved are no longer squared. The weight function, denoted as $W_j(x, y)$, plays a crucial role in emphasizing specific sub-domains (cells) within the overall solution domain, D. The choice of weight functions is flexible, and a straightforward strategy often involves assigning either 0 or 1 as weights. For instance, unit weight might be applied within one triangular cell and zero in all others in the first equation. This approach aims to enforce the trial function, and eventually the solution, to satisfy the partial differential equation (PDE) across every cell.

A common application of the method is to use unit weight in cell number j and zero elsewhere, resulting in m equations for various parts of the solution domain. However, a challenge arises as the number of cells (m) is typically much smaller than the number of nodes (n). Assuming a single dependent variable (u) and boundary conditions specified by values around the boundary, is necessary to solve for interior node values, which are generally more numerous than the cells. To address this, sophisticated weighting schemes are required, particularly in cases involving multiple dependent variables.

Several rules guide the choice of weight functions. If a node (j) is a midpoint, W_j is set to 1 for the two cells sharing this point and 0 elsewhere. For a corner node, W_j is set to 1 for the cells sharing that corner and 0 elsewhere. On the boundary, only one cell is used. This method ensures the correct number of equations and yields independent equations by treating all sub-domains for integration as distinct.

In scenarios where the PDE and boundary conditions are linear, the analysis results in a system of linear equations. For non-linear cases, a more general system of algebraic equations is obtained. The simulation addresses non-linear systems using iterative methods, although these methods may take longer and exhibit capricious behavior.

2.12.3 Natural Boundary Conditions

So far assuming that the values of the solution are given on the entire boundary. If the problem involves natural conditions over the entire boundary or part of it, this information must be incorporated by special means. A well-known theorem that connects the integral of a PDE with the outward normal component of a field $\mathbf{F}$ is:

$$\iiint \nabla^2 U dV = \iiint \nabla \cdot (\nabla U) dV = \iiint \nabla \cdot \mathbf{F} V = \oiint \mathbf{F} \cdot dS. \tag{2.49}$$

When integrating the PDE over a sub-domain, incorporating the Laplacian's volume integral entails replacing it with a surface integral that involves the natural boundary condition. The remaining two surfaces of the cell necessitate integrals that should align with those from adjacent cells. In the presence of natural boundary conditions, it becomes crucial to acknowledge that multiplying the PDE by a specific factor inevitably alters the volume integral, thereby impacting the surface integral over the boundary. Consequently, when multiplying the PDE by a factor ff, it is imperative to apply the same factor to the corresponding natural boundary condition.

2.13 Runge-Kutta 4th Order Method for 2D PDEs

The Runge-Kutta method, typically used for ordinary differential equations (ODEs), can also be extended to solve partial differential equations (PDEs) [53]. When dealing with 2D PDEs, such as those involving two spatial dimensions, the method becomes more involved but follows the same fundamental principles. Let's explore the basic concept of the Runge-Kutta method for 2D PDEs.

Consider a 2D PDE of the form:

$$\frac{\partial u}{\partial t} = F(t, x, y, u, \frac{\partial u}{\partial x}, \frac{\partial u}{\partial y})$$

Here, $u(t, x, y)$ represents the solution field, and F is a given function describing the evolution of u with respect to time t and the spatial variables (x and y). The partial derivatives $\frac{\partial u}{\partial x}$ and $\frac{\partial u}{\partial y}$ represent the spatial gradients of u.

Now, to apply the Runge-Kutta method to solve this 2D PDE, discretizing the spatial and temporal dimensions. Let t_n be the current time, x_i and y_j be spatial grid points, and u_{ij}^n be the approximate solution at time t_n and position (x_i, y_j).

The general form of the Runge-Kutta method for 2D PDEs can be expressed as follows:

$$u_{ij}^{n+1} = u_{ij}^n + \frac{1}{6}(k_1 + 2k_2 + 2k_3 + k_4). \tag{2.50}$$

Where

$$\begin{aligned}
k_1 &= \Delta t \cdot F(t_n, x_i, y_j, u_{ij}^n, \frac{\partial u_{ij}^n}{\partial x}, \frac{\partial u_{ij}^n}{\partial y}) \\
k_2 &= \Delta t \cdot F(t_n + \frac{\Delta t}{2}, x_i + \frac{\Delta x}{2}, y_j + \frac{\Delta y}{2}, u_{ij}^n + \frac{k_1}{2}, \frac{\partial u_{ij}^n}{\partial x}, \frac{\partial u_{ij}^n}{\partial y}) \\
k_3 &= \Delta t \cdot F(t_n + \frac{\Delta t}{2}, x_i + \frac{\Delta x}{2}, y_j + \frac{\Delta y}{2}, u_{ij}^n + \frac{k_2}{2}, \frac{\partial u_{ij}^n}{\partial x}, \frac{\partial u_{ij}^n}{\partial y}) \\
k_4 &= \Delta t \cdot F(t_n + \Delta t, x_i + \Delta x, y_j + \Delta y, u_{ij}^n + k_3, \frac{\partial u_{ij}^n}{\partial x}, \frac{\partial u_{ij}^n}{\partial y})
\end{aligned}$$

In this expression:

k_1, k_2, k_3, and k_4 are intermediate values calculated using the function F and the current state of the solution. Δt is the time step, and Δx and Δy are the spatial step sizes. The term u_{ij}^{n+1} is a weighted average of these intermediate values.

This process is repeated for each grid point (x_i, y_j) and each time step to evolve the solution over time. It's important to note that the specific details may vary based on the nature of the PDE and the discretization scheme used. The above formulation provides a general idea of how the Runge-Kutta method can be adapted for 2D PDEs.

2.14 Spectral Method for 2D PDEs

The spectral method excels in solving 2D partial differential equations by efficiently decomposing solutions with orthogonal basis functions, like trigonometric or polynomial functions. Utilizing fast transforms such as the 2D Fourier Transform enhances computational efficiency, enabling rapid convergence with fewer modes for smooth solutions. Success hinges on careful consideration of tailored basis functions for specific boundary conditions [54].

2.14.1 Example of Spectral Method Implementation

Consider the generic 2D advection-diffusion equation given by:

$$\frac{\partial u}{\partial t} + \mathbf{v} \cdot \nabla u = D\nabla^2 u$$

Here, $u(x, y, t)$ represents the unknown quantity, $\mathbf{v} = (v_x, v_y)$ is the advection velocity vector, and D is the diffusion coefficient. The specifications for the considered problem are outlined in this section. The spatial and temporal domains, denoted by x, y, and t, are defined within the intervals $[0, L]$ and $[0, T]$ respectively. The initial condition

$$u(x, y, 0) = \sin(\pi x)\cos(\pi y),$$

Characterizing the initial state of the system illustrates a specific distribution of the unknown quantity u across the spatial domain. These specifications set the context for implementing the spectral method, which utilizes 2D Fourier modes as basis functions:

$$\phi_{m,n}(x, y) = e^{i(2\pi mx/L + 2\pi ny/L)}.$$

Discretize the spatial domain with grid points, express the initial condition in the spectral domain using Fourier series, and calculate Fourier coefficients $\hat{u}_{m,n}$. Apply a time-stepping method like the Runge-Kutta method to evolve the solution in time. Leverage the 2D Fourier Transform for efficient computation in the spectral domain, obtaining $\hat{u}_{m,n}$.

$$\hat{u}_{m,n} = \mathcal{F}[u(x, y)] = \int_S u(x, y)\phi_{m,n}(x, y)dS \quad \text{and} \quad u(x, y) = \mathcal{F}^{-1}[\hat{u}_{m,n}].$$

It is also necessary to implement periodic boundary conditions in both x and y directions.

In summary, the spectral method proves its efficacy through the application to a 2D diffusion equation, showcasing its ability to accurately capture complex spatiotemporal dynamics.

Chapter 3

Light-Induced Ring Pattern

This chapter presents the experimental behavior of a dye-doped liquid crystal cell (DDLCC) when subjected to a Gaussian-light pump. Additionally, a numerical model is provided from first principles. The study of this model aims to enhance our understanding of the system. To understand this system, is important to notice that the utilization of a DDLCC enables the amplification of the coupling between light and liquid crystals, a coupling that is considerably low in a typical NLC. Light has the capability to induce self-organization in the molecular order.
This coupling between light and liquid crystal gives rise to the emergence of spatial patterns that reach an equilibrium. In this experiment, the primary outcome is the presence of ring patterns. This phenomenon was observed with two different photosensitive dopants and was subsequently compared with numerical simulations of a proposed model.

The phenomena observed in this chapter is based in prior investigations [17, 41] focusing on the emergence and propagation of specific structures. However, these earlier studies faced limitations as they employed a single pump laser for both inducing and observing effects.

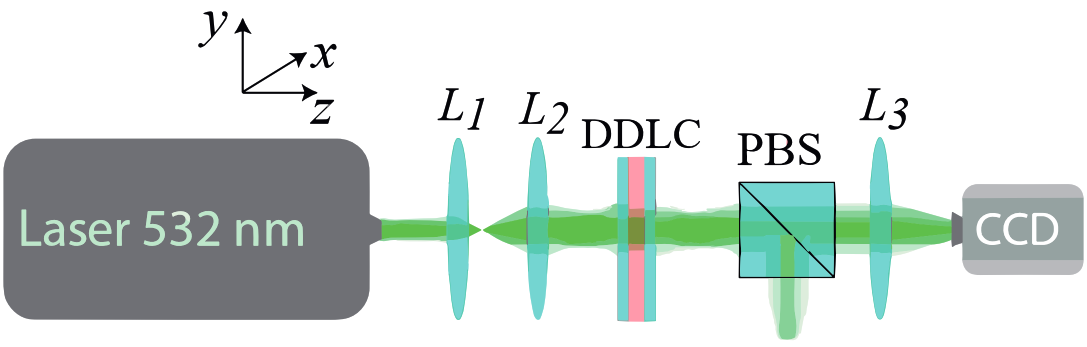

Figure 3.1: Experimental setup for photo-isomerization featuring a single-beam configuration [17]. Lenses L_1 and L_2 function as a telescope, fine-tuning the beam waist. The sample, DDLC, undergoes photo-isomerization. A polarizer beam splitter (PBS) minimizes the intensity directed towards the camera. Lens L_3 is strategically positioned to capture the entire beam on the camera's CCD.

The experimental setup depicted in Figure 3.1 illustrates a single-beam configuration, as described in [17]. Lenses L_1 and L_2 act as a telescope, adjusting the beam waist, while the sample, DDLC, undergoes photo-isomerization process. A polarizer beam splitter (PBS) reduces the intensity directed towards the camera, and lens L_3 is strategically placed to capture the entire beam on the CCD.

Nevertheless, this setup has drawbacks. It primarily showcases the effect at the pump location, limiting the observation of the entire sample. Additionally, the intensity recorded by the CCD camera varies with the pumping intensity. This variability poses challenges in comparing transmittance across different pump intensities, and certain structures may become saturated, leading to a loss of dynamic information.

3.1 Experimental Ring Pattern

3.1.1 Experimental Setup

Employing a planar anchoring DDLCC in the experimental setup (Figure 3.2). These cells consist of a mixture of nematic E7 liquid crystal and an azo-dye dopant, (methyl-red or methyl-red-methyl-ester which have different absorbance curves) between two glass plates with a thickness of 25 μm. The dopant molecules are introduced to enhance the coupling between the liquid crystal and light within the absorption curve of the photoisomerization transition of the dopant. Consequently, the addition of the dopant reduces the required input light to induce a phase transition of the liquid crystal. The weight concentration of the dopant in the liquid crystal ranges from 0.25 % to 1 %.
In the typical way of detecting phototropic transitions, is common to use a method involving a laser beam and special microscopy. This method loses information about how the liquid crystal behaves outside of the central illuminated area. This makes it hard to tell the difference between changes in the light that the microscope filters out and the light absorbed by the sample.
To solve these problems, a new setup is designed using two parallel laser beams on the DDLCC sample. The sample only reacts to one beam (the pumping one), and the other beam (the probing one) does not affect it, because choosing the wavelength of each one due to the absorption curve (Fig. 2.13). This way, is possible to study the sample behavior more effectively.
It is important to note that the wavelengths of the probe and pump lasers depend significantly on the absorbance spectrum of the dopant. In this case, it is essential that the probe laser exhibits low absorbance for the dopant, and its power should be kept low to prevent secondary photoisomerization effects. On the other hand, the pump laser needs to have a substantial absorbance and sufficient power to initiate dynamics in the system.

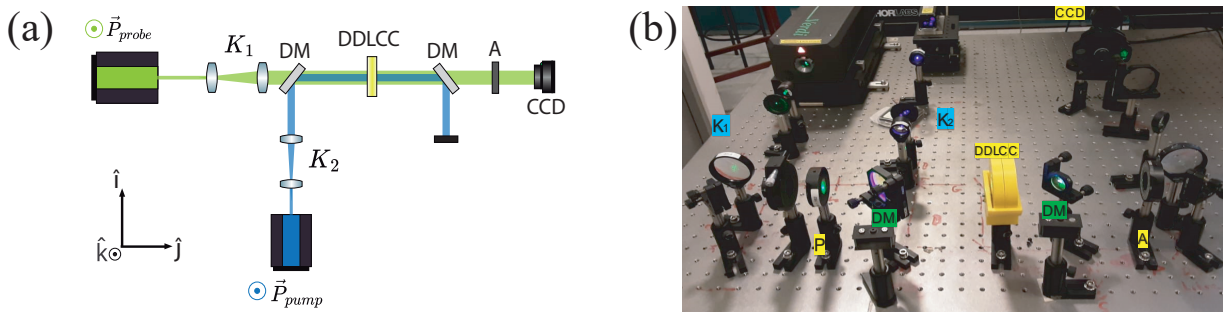

Figure 3.2: (a) Experimental setup diagram for DDLCC sample photoisomerization involves simultaneous irradiation with a pump laser and illumination by a probe laser. A Kepler telescope configuration (K_1, K_2) of lenses expands and collimates the laser beams, both exhibiting vertical polarization. Long-wave pass dichroic mirrors (DM) align and filter the beams, and an analyzer (A) in a crossed orientation allows observation on a CCD camera, ensuring precise control of the photoisomerization process. (b) Snapshot of the experimental setup.

Analyzing Figure 3.3, it is evident that methyl-red-methyl-ester exhibits peak absorbance at 420 nm. Consequently, a blue laser source (445 nm) is suitable as a pump, and a green laser (532 nm) can serve as a probe due to the absorbance in that wavelength being lower than 0.1 (ensuring the output power is set to a minimum). A similar analysis can be conducted for methyl-red, wherein the absorbance peak occurs at 494 nm. In this case, either laser can be employed as a pump or probe. However, it is crucial to consider the maximum output power of each laser. The green laser (Verdi V-2) boasts a maximum power of 2.2 W, while the blue laser (Cobolt 04) has a maximum power of only 100 mW. To achieve a broader measurement range, the green laser is setted as the pump and the blue laser as the probe for methyl-red.

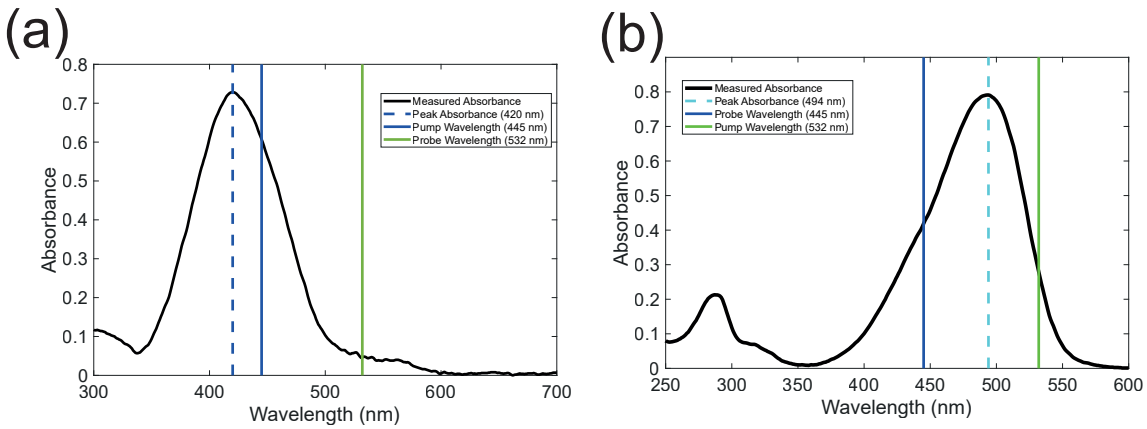

Figure 3.3: Absorbance spectrum of each dopant: (a) methyl-red-methyl-ester and (b) methyl-red. Pump and probe wavelength is marked as solid lines, and showing the maximum absorbance as dashed line.

3.1.2 Methyl-red-methyl-ester dopant observations

Using the configuration showed in figure 3.2 for each DDLCC, it is possible to explore a range of powers (from 0 mW to the maximum pump laser power). Therefore, in the first instance, the setup was prepared for the DDLCC with 1 % of methyl-red-methyl-ester (blue laser as a pump). Studying the effect of different light intensities, it is possible to observe some stable spatial structures.

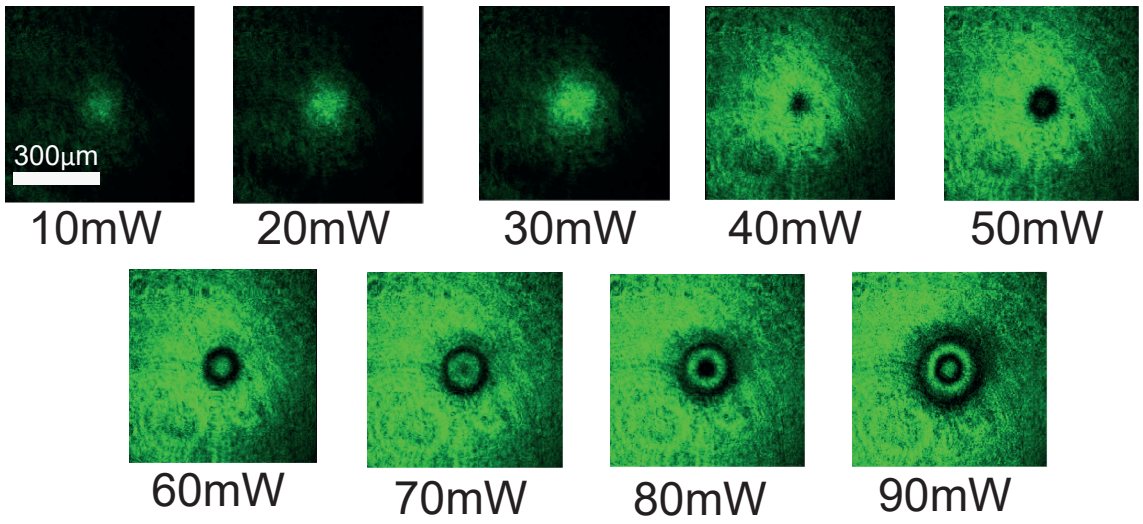

Figure 3.4: Stable spatial structures induced in a DDLCC with Methyl-red-methyl-ester

Injecting pump light into the DDLCC with methyl-red-methyl-ester, three distinct regimes can be identified in figure 3.4. Below 30 mW, the system exhibits solely a modulation of the Gaussian beam. Between 40 mW and 50 mW, the emergence of a localized spot in the center is observed. Subsequently, in the range of 60 mW to 90 mW, a radial modulation is emerged (ring pattern). It is essential to note that technical limitations impose a maximum power constraint on the pump laser, restricting observations to a narrow range of light power, particularly when compared to the broader range of green laser power.

In this experiment, a important behavior is the emergence and stabilization of ring patterns. To comprehensively study these structures, it is necessary to investigate the characteristic time for these patterns to reach stability. Figure 3.5 presents the results of the 90 mW experiment.

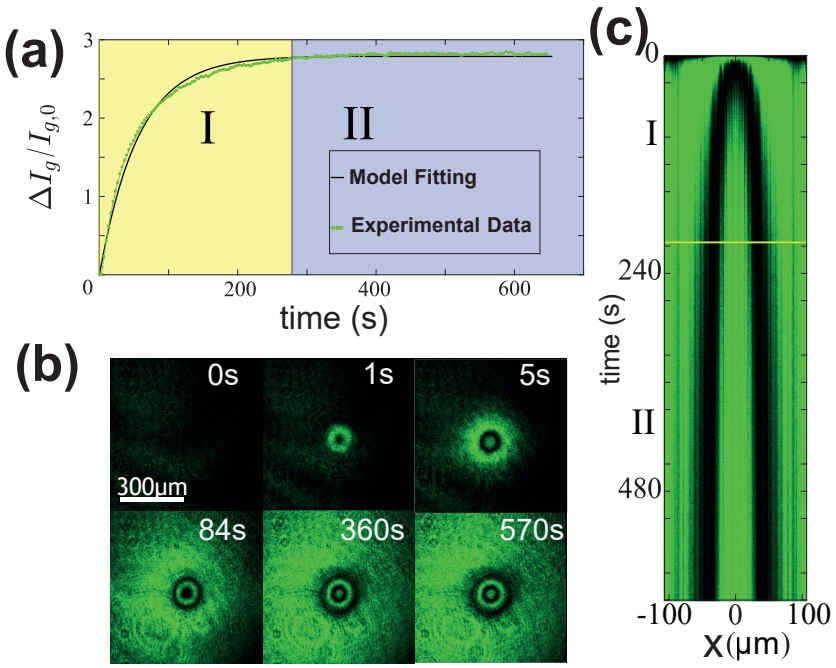

Figure 3.5: Experimental emergence and evolution of ring patterns induced by blue light applied to a DDLCC with methyl-red-methyl-ester.(a) illustrates the evolution of the quotient between the intensity of green light transmitted and the initially transmitted green light with no blue light. The fitted curve $T_{fit} = A(1 - e^{t/\tau})$ is included, where $A = 2.79$ and $\tau = 55.71\ s$ are computed (τ represents the time taken to reach equilibrium). The shaded areas I and II correspond to the growth and saturation regions, respectively. (b) Snapshots from temporal evolution, (c) spatiotemporal diagram of a cut in a diameter of the ring pattern.

To understand the process of spot emergence and ring propagation, analyzing the spatiotemporal evolution of a diameter cut section. Figure 3.5(c) illustrates the observed spatiotemporal diagram evolution, providing insights into how the dark rings emerge, propagate, and eventually come to a halt.

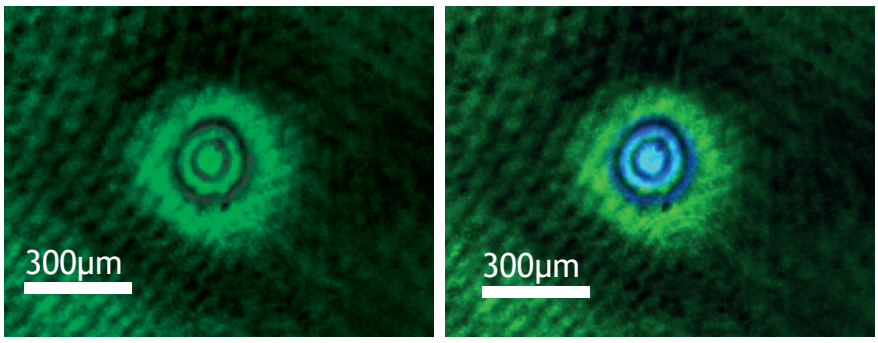

Figure 3.6: Waist comparison between pump and probe laser (removing the second DM from the experimental setup)

Upon exposure to blue light, a light green region with a dark spot in the center emerges. Subsequently, the initial dark spot evolving into an expanding ring. Notably, the illuminated area continued to grow, surpassing even the waist of the blue laser (Fig.3.6).

Figure 3.6 provides a visual comparison between the light green region and the waist size of the blue laser. Over time, the dark ring gradually propagates outward from the center, giving rise to a new dark spot in the center. This newly formed spot then evolves into another dark ring. This sequence is depicted in Figure 3.5(b).

3.1.3 Methyl-red dopant observations

As outlined in this chapter, there has been a switch in the configuration of the pump and probe lasers for the methyl-red dopant compared to the previous configuration of the setup. In this instance, a blue laser is employed for observation, while a green laser is utilized to induce the phenomena. This configuration adjustment enables the observation of a broader power range for in-depth study.

In this scenario, the sample is a planar anchoring DDLCC with a 1 % concentration of methyl-red. As depicted in Figure 3.3(b), the absorbance peak occurs at $494nm$. Therefore, employing blue light as the probe and green light as the pump enables the exploration of structure emergence in this particular sample.

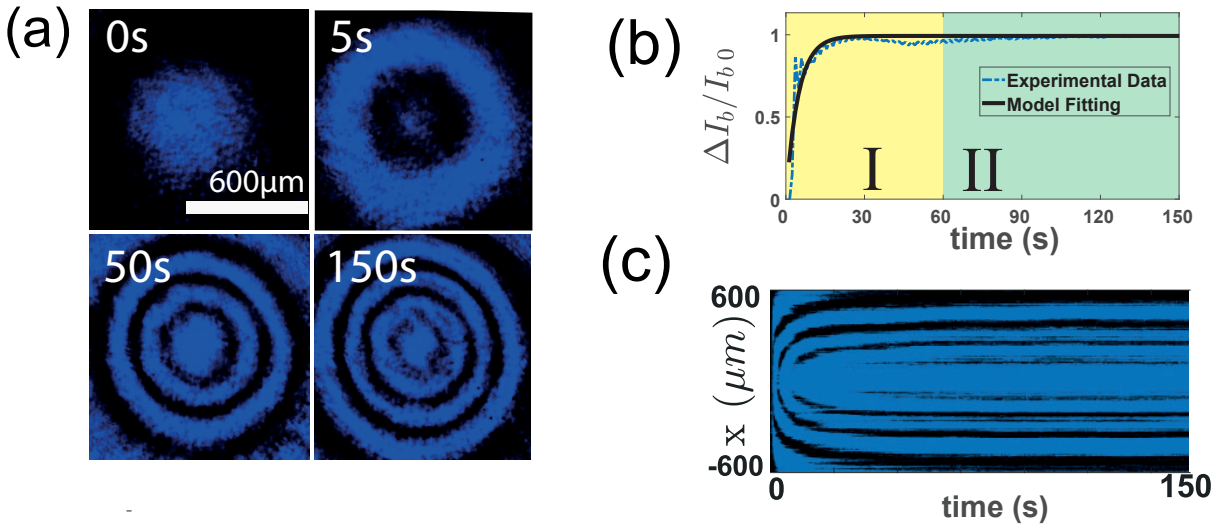

Figure 3.7: Experimental emergence and evolution of ring patterns induced by green light applied ($0.67\ W$) to a DDLCC with methyl-red: (a) Snapshots from temporal evolution, (b) evolution of transmitted blue light and saturation, (c) spatiotemporal diagram of a cut in a diameter of the ring pattern.

Comparing both dopants, noticing that at lower power, particularly at 0.67 W, the structures display essentially the same behavior as Methyl-red-methyl-ester. Notable differences are evident; for instance, as illustrated in Figure 3.7(b), the model $T_{fit} = A(1 - e^{t/\tau})$ with $A = 0.98$ $\tau = 14.74$ s indicates that the equilibrium is achieved around 60 s, representing a faster stabilization compared to the previous case. Also is are identified the growth and saturation (I & II in Fig. 3.7(b)) evolution in the transmitted light. The possibility to reach higher powers enables the observation of a greater quantity of rings.

Rings instability.

As previously mentioned, the behavior from 0 W to 0.68 W aligns with the observed in methyl-red-methyl-ester. However, reaching higher powers a new dynamic—the instability of the ring patterns.

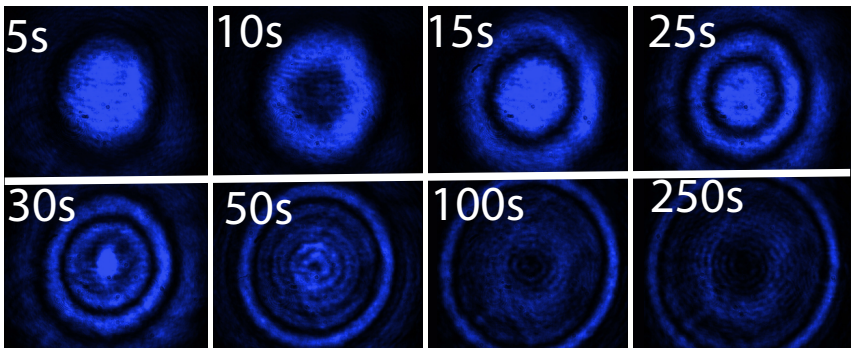

Figure 3.8: Snapshots of experimental evolution that shows instability of rings at 0.69 W for DDLCC mixture of E7 with 1 % of methyl-red.

Figure 3.8 reveals a notable transition occurring at a power level of 0.69 W. Beyond this critical power threshold, the previously observable ring pattern dynamics abruptly cease. Previous observations have explored the unstable front associated with this transition [17], it primarily represents the initial instability of the rings. The unexplored realm beyond 1 W remains a significant gap in current research. As illustrated in Figure 3.9, the structures observed at higher power levels exhibit increased interaction, suggesting a promising avenue for future research endeavors.

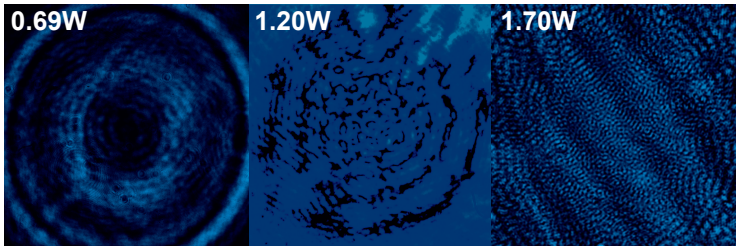

Figure 3.9: Snapshots of different behavior induced by High power of pump laser.

3.2 Dye-Doped Liquid Crystal Model

To elucidate the dynamical behavior stemming from the photoisomerization process within a DDLCC, is introduced a comprehensive model coupling the concentration of molecules in the cis state (equations 2.30 and 2.31) also considering a reciprocal interaction relation between both of them [44] (introducing equations 2.36 to the model), denoted as $C(x, y, t)$, and the scalar order parameter $S(x, y, t)$. This model is expressed as follows:

$$\begin{aligned} \frac{dC}{dt} &= -\lambda[C - C_0(I) + \alpha S] + \delta\nabla^2 C + D\nabla^2 S, \\ \frac{dS}{dt} &= -(A + \beta C)S + BS^2 - S^3 + \nabla^2 S + D\nabla^2 C. \end{aligned} \tag{3.1}$$

In this model, the boundary condition is determined by the non-homogeneous pump waist. If the simulation is far from it, the effect is negligible, allowing the boundary condition to be defined as $u(r = 5\omega, 0) = 0$, where ω denotes the Gaussian waist. The parameter α captures the reduction in $C(x, y, t)$ due to increased alignment in the liquid crystal molecules (larger S), influenced by the transition from cis to trans [36]. The diffusion coefficients δ represent dopant concentration dispersion in parallel and orthogonal directions to the incident light's electric field. The entropic effect of photoisomerization, denoted by β, indicates that a higher concentration of cis molecules favors a disordered state. The parameter D accounts for mutual transport processes within the system, embodying the dynamic interplay of various contributing factors.
In the regime of temporal scale separation between the order parameter, denoted as S, and the concentration of the cis-state ($\lambda \gg 1$), with small α and intensity I as implicated in explaining the observed emergence and propagation of rings in the previous section, the cis-state concentration is:

$$C \approx C_0(I) \approx \gamma I, \tag{3.2}$$

This manifestation arises from the intricate interplay of large-scale separation, modest α, and the incident light intensity I. Concurrently, the light's intensity follows a spatial distribution governed by:

$$I = I_0 e^{-\frac{r^2}{w^2}}, \tag{3.3}$$

Here, w and I_0 represent the light beam's waist and intensity at its center, respectively. Consequently, the cis-state concentration assumes a Gaussian profile. Substituting this expression into the order parameter equation, S adheres to the Landau–De-Gennes model for the nematic to isotropic transition induced by photoisomerization. Notably, the bifurcation parameter $A(I) \equiv A + \beta\gamma I$ is modulated by the spatial profile of light intensity. In the absence of illumination, the system resides in a NLC phase. Conversely, when subjected to light, the induced front propagation triggers a transition from the isotropic to the nematic phase.

3.2.1 Adiabatic Elimination and Reduced Model

To study the dynamics in Equation 3.1, is possible to employ adiabatic elimination to comprehend the effect of cis-state concentration [45, 55]. This approach assumes that the temporal evolution of the cis-state concentration is significantly faster compared to the dynamics of the order parameter, denoted as $\lambda \gg 1$. By applying Neumann series in cis-concentration equation (Eq. 3.1), is possible to express the cis concentration in a dominant order as:

$$C \approx C_0(I) - \alpha S + \frac{D - \alpha\delta}{\lambda}\nabla^2 S. \tag{3.4}$$

Substituting this expression into the equation governing the order parameter S (Eq. 3.1), is obtained, at a dominant order:

$$\begin{aligned}\frac{dS}{dt} = &-[A + \beta C_0(I)]S + (B - \alpha\beta)S^2 - S^3 + (1 - D\alpha)\nabla^2 S \\ &+\frac{D(D - \alpha\delta)}{\lambda}\nabla^4 S + \frac{\beta(D - \delta\alpha)}{\lambda}S\nabla^2 S + D\nabla^2 C_0(I).\end{aligned} \tag{3.5}$$

It is possible to re-normalize the space using $\vec{r} = \vec{r'}[\lambda/(\delta\alpha D - D^2)]$, leading to the reduced model:

$$\frac{dS}{dt} = -\tilde{A}S + \tilde{B}S^2 - S^3 + \nu\nabla^2 S + \nabla^4 S + bS\nabla^2 S + \eta. \tag{3.6}$$

Introducing the re-normalized coordinate, are obtained the following relations:

$$\begin{aligned}\tilde{A}(\vec{r'}) \equiv A + \beta C_0(I(\vec{r'})), \qquad & \tilde{B} \equiv B - \alpha\beta, \\ \nu \equiv D\alpha - \sqrt{\tfrac{\lambda}{D(\delta\alpha - D)}}, \qquad & b \equiv \beta\tfrac{D - \delta\alpha}{\sqrt{\lambda D(\delta\alpha - D)}}, \\ \eta(\vec{r'}) \equiv \sqrt{\tfrac{D\lambda}{(\delta\alpha - D)}}\nabla^2 C_0(I(\vec{r'})) & .\end{aligned}$$

These relations express the modified parameters in terms of the original variables. It is crucial to emphasize that $\eta(\vec{r'})$ is contingent upon the specific shape of the Gaussian beam; however, it remains temporally constant when the beam remains with the same intensity.

The equation presented in 3.6 characterizes a non-variational Swift–Hohenberg-type model [56, 57, 29, 58]. This mathematical representation has proven instrumental in the exploration of various phenomena, including patterns [59, 60], localized and stationary structures [56, 61], propagative formations [62], as well as spatiotemporal chaotic extended and localized structures [60, 62]. These investigations span multiple disciplines, from physics and chemistry to biology.

The emergence of spatial structures in this model is attributed to the presence of an anti-diffusion coefficient ($\nu > 0$). This coefficient encapsulates the distinct scales of transport processes for the cis order and state parameter, introducing an inherent characteristic scale known as the Turing mechanism [30]. Essentially, the system, governed by two transport processes with differing scales, undergoes self-organization, preventing homogeneous propagation of the order parameter and the cis-state. This interplay results in the formation of the mentioned patterns.

3.2.2 Stability Analysis of Non-Variational Swift-Hohenberg Model.

To investigate the behavior of this model, it is crucial to examine various characteristics. Beginning by consider the impact of homogeneous illumination, denoted as $C_0(I(x,y)) = C_0$, implying $\nabla^2 C_0 = 0$. The resulting effective model is expressed as:

$$\frac{dS}{dt} = -\tilde{A}S + \tilde{B}S^2 - S^3 + \nu\nabla^2 S + \nabla^4 S + bS\nabla^2 S, \tag{3.7}$$

Analyzing the homogeneous solution, following equation for the order parameter is derived:

$$0 = -\tilde{A}S + \tilde{B}S^2 - S^3. \tag{3.8}$$

This equation yields three solutions for S, $S_0 = 0$ representing the isotropic state, and two phases corresponding to nematic states:

$$S_{\pm} = \frac{\tilde{B} \pm \sqrt{\tilde{B}^2 - 4\tilde{A}}}{2}. \tag{3.9}$$

Nematic solutions exhibit a real part when $\tilde{A} < A_{SN} = \tilde{B}^2/4$. To initiate the study of the dynamical properties of this model, is possible to determine the Maxwell point A_M [31] by analyzing the free energy:

$$F(S) = -\frac{\tilde{A}}{2}S^2 + \frac{\tilde{B}}{3}S^3 - \frac{1}{4}S^4. \tag{3.10}$$

Upon inspection, it becomes apparent that $S = 0$ is a solution with multiplicity two, and two real solutions exist, given by $S = \left(2\tilde{B} \pm \sqrt{2}\sqrt{2\tilde{B}^2 - 9\tilde{A}}\right)/3$. The Maxwell point occurs when the discriminant is $\Delta = 0$, resulting in:

$$A_M = \frac{2}{9}\tilde{B}^2. \tag{3.11}$$

To further explore relevant points for the linear parameter, it is necessary to calculate the Turing instability of each solution [30]. The instabilities are study by linearizing the equation 3.7 around the solutions. For $S_0 = 0$, using the ansatz $S(\vec{r}, t) = S' e^{i\vec{r}\cdot\vec{k}+\sigma_0 t}$, the growth rate equation replacing this in 3.7, and linearizing

$$\sigma_0 = -\tilde{A} + \nu\vec{k}^2 - \vec{k}^4, \tag{3.12}$$

The condition for instability is given by $d\sigma_0(k_c)/dk = 0$, where $\sigma_0(k_c)$ provides the value of the Turing instability parameter A_{sp} for the isotropic solution. The first condition determines the critical length, and the second defines the critical parameter relationship for spatial instability.

$$\frac{d\sigma_0}{dk} = 2\nu\vec{k} - 4\vec{k}^3 = 0 \quad \text{, i.e.,} \quad k_c = \sqrt{\frac{\nu}{2}}, \tag{3.13}$$

$$\sigma_0(\vec{k}_c) = -\tilde{A} + \frac{\nu^2}{2} - \frac{\nu^2}{4} \quad \text{, i.e.,} \quad \tilde{A}_{sp} = \frac{\nu^2}{4}. \tag{3.14}$$

A weakly nonlinear analysis reveals that this instability is of a supercritical nature for small $\tilde{B}$, which is easily observed as the solutions exhibit pitchfork bistability in the case when $\tilde{B} = 0$. Thus, despite the fact that the linear term is positive, $0 < \tilde{A} < A_{sp}$, the isotropic liquid state is unstable. For $\tilde{A} = 0$, the system presents a transcritical bifurcation between unstable states.

For the nematic solutions, considering a small perturbation around the solutions $S(\vec{r}, t) = S_\pm + \varepsilon e^{i\vec{r}\cdot\vec{k}+\sigma_\pm t}$, where $0 < \varepsilon << 1$. Substituting this ansatz into Eq. 3.7, the growth rate is given by:

$$\sigma_\pm = -\tilde{A} + 2\tilde{B} - 3S_\pm^2 + (\nu + bS_\pm)\vec{k}^2 - \vec{k}^4. \tag{3.15}$$

By imposing the spatial instability conditions, as in the previous case:

$$k_c = \sqrt{\frac{\nu + bS_\pm}{2}} \tag{3.16}$$

With the second condition, the spatial instability $A_{sp}^\pm$ is given by:

$$2\tilde{A}_{sp}^\pm + \tilde{B}S_\pm = -\frac{(\nu + bS_\pm)^2}{4} \tag{3.17}$$

It is important to note that the solutions $S_\pm$ are dependent on $\tilde{A}$ and $\tilde{B}$. Obtaining an explicit value for $A_{sp}^\pm$ can be challenging, and a numerical Newton method is required for this purpose [63]. A importan issue of this model is that the non symmetry of $A_{sp}^\pm$ is produced by the presence of the non variational term $bS\nabla^2 S$.

This critical point allows us to construct a comprehensive understanding of the behavior of this effective model. Such insight is crucial for conducting numerical simulations, as it enables the study of particular parameter values that exhibit bistability and a characteristic wavelength (gven by the wave number) that can produce the desired structures.

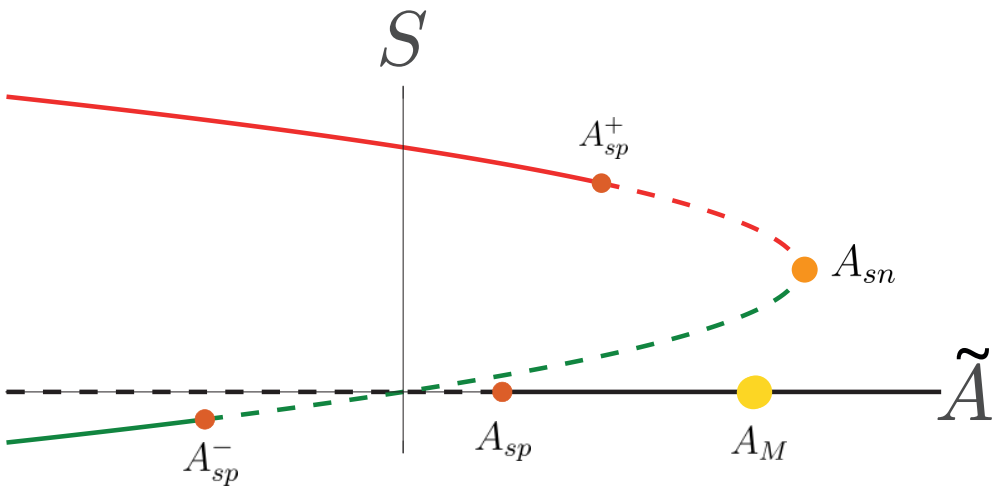

Figure 3.10: Bifurcation diagram of the effective model given by Equation 3.7 with constant coefficients. The plot illustrates the order parameter S as a function of the bifurcation parameter $\tilde{A}$. In this diagram, S_0 (black line), S_+ (red line), and S_- (green line) represent the isotropic liquid and nematic phases, respectively. Continuous and dashed lines correspond to stable and unstable states, respectively. The critical points A_{sn} and A_M denote the emergence of the nematic phase and the Maxwell point respectively. Additionally, A_{sp}, A_{sp}^{+}, and A_{sp}^{-} account for the spatial instabilities of the homogeneous phases.

3.2.3 Light-Induced Ring Pattern Simulations

The model representing the system exhibits a coexistence region between the nematic state and a pattern, as revealed in the prior analysis. This pattern alternates between areas of higher and lower orientation order [18]. The presence of this pattern has a notable impact on the sample's refractive index. Consequently, when a light beam traverses the sample in a patterned state, interference fringes are expected to manifest.

As the light intensity increases, the bifurcation parameter $\tilde{A}$ also grows. Considering a light intensity with a Gaussian profile, the parameter $\tilde{A}(I) = A + \beta C_0(I)$ becomes inhomogeneous, resembling a bell-shaped curve. Consequently, if the cell is in a nematic phase during illumination, the central part of the light beam can induce the cell to move out the coexistence region, stabilizing only the pattern. In such scenarios, one anticipates observing patterns in the illuminated area due to the circular central region of the light beam. For a small-waist beam, ring-like patterns are expected. Figure 3.11 illustrates a ring pattern equilibrium observed numerically for the model given by Equation 3.6.

All numerical simulations presented here are conducted using finite differences and the RK4 algorithm [53].

To facilitate a meaningful comparison between the model simulation and the experiments illustrated in 3.5 and 3.7, it is crucial to recognize the indistinguishability of the nematic phases in the experimental data. Therefore, for a relevant simulation, the observed field is set to S^2.
As an example figure 3.11 is obtained from the following parameters: $A = -0.5$, $\tilde{B} = 0.3$, $\nu = 1.05$, $b = 0.1$, $\beta = 1$. The cis-state concentration is determined by $C_0(I) = \gamma I_0 e^{-r^2/\omega^2}$, with $\gamma = 1$, the intensity $I_0 = 1.45$, and the waist of the beam $\omega = 4$.

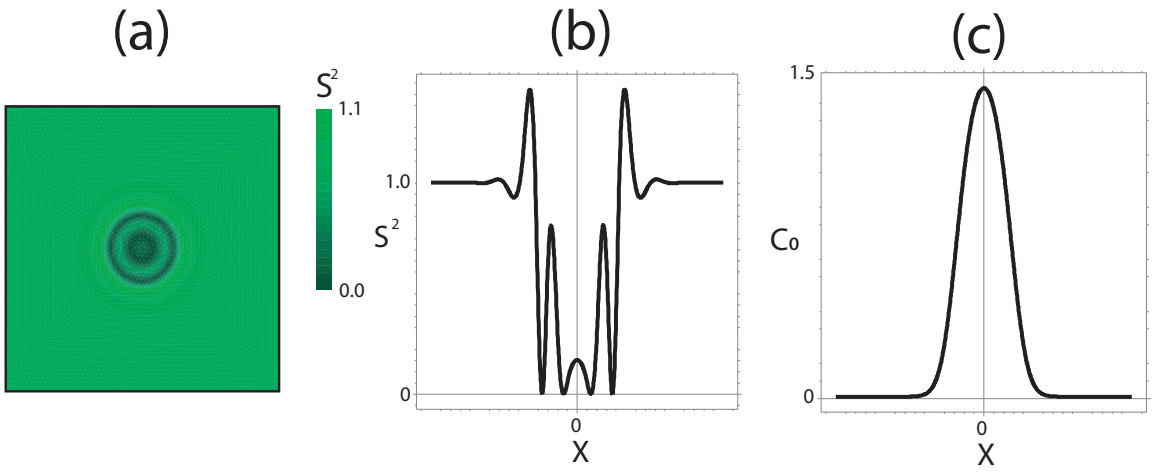

Figure 3.11: Simulation results of the effective model 3.6: (a) Visualization of the S^2 field exhibiting a ring pattern structure, (b) Horizontal cross-section of the structure, and (c) Spatial density representation of the cis state molecules C_0.

If the system is not illuminated ($I_0 = 0$), the equilibrium state is a uniform nematic phase, and settting $\tilde{A} < A_{sp}$ to ensure the instability of the isotropic state. Upon illuminating the system with low intensity, numerical simulations revealed a slight reduction in the reorientation order and an increase in the cis concentration in the central part of the Gaussian.

As the intensity I_0 increased, the central spot exhibited greater orientation disorder; specifically, the order parameter S decreased in the central zone with increasing I_0. Notably, the region of orientational disorder remained smaller than the waist of the Gaussian forcing; this occurs when $A + \beta C_0(I_0) < A_{sp}^-$.

However, when I_0 is controlled, it becomes feasible to explore other regions. If $A_{sp} < A + \beta C_0(I_0) < A_{sp}^+$, rings connecting the isotropic and one nematic phase can be observed, as illustrated in Figure 3.11. These rings are also modulated by the Gaussian form. A crucial observation regarding Figure 3.11 is that the presence of modulated rings by the inhomogeneous parameter could be attributed to the non-variational term $bS\nabla^2 S$. Without this term, the instability of S_+ would not manifest, and the solution would remain stable until reaching A_{sn}. Beyond this point, without the non-variational term, the system would directly transition to the isotropic state, and the observed modulated ring patterns would not occur.

If $A_{sp}^+ < A + \beta C_0(I_0)$, the only stable state is $S_0 = 0$. In this case, the region where the spatial inhomogeneity is effective should eventually converge to zero.

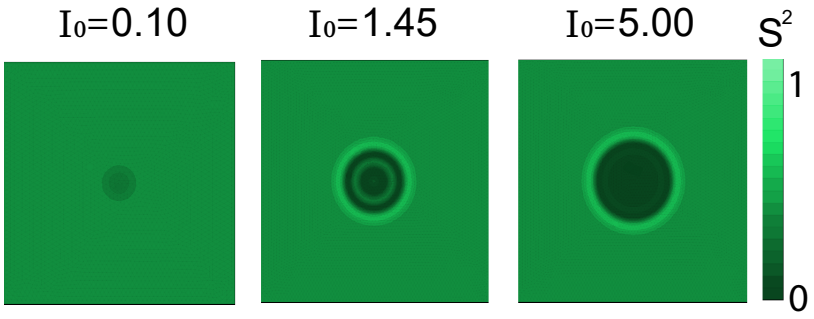

Figure 3.12: Steady state representing different values of light pumping (I_0) in the simulation, changing the effective linear parameter.

In the range $A_{sp}^{-} < A + \beta C_0(I_0) < A_{sp}$, the system exhibits the presence of permanently propagating rings, which is dissimilar to the experiment where the rings saturate (Figure 3.13). Unlike Figure 3.11, these rings have the same amplitude and are not modulated by the Gaussian inhomogeneity. Importantly, this is the only scenario where structures evolve beyond the Gaussian inhomogeneity, and the rings start to deform when approaching the boundaries.

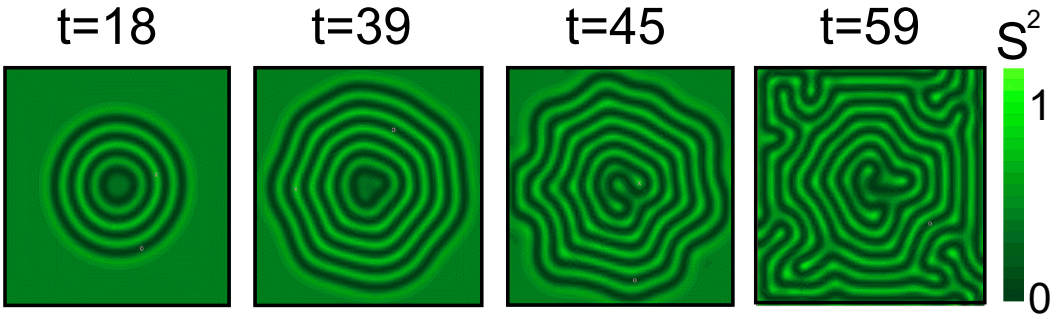

Figure 3.13: Simulation (temporal evolution) illustrating the competition between instabilities of S_0 and S_- in the range $max(\tilde{A} \in [A_{sp}^{-}, A_{sp}])$.

In Summary, the model described by Equation 3.6 adeptly captures the qualitative dynamics of the light-induced ring pattern in a dye-doped nematic liquid crystal, especially within the range $A_{sp} < \tilde{A} < A_{sp}^{+}$. In the regime $A_{sp}^{-} < \tilde{A} < A_{sp}$, the ring propagates over a greater distance than $r = 5\omega$, resulting in destabilization attributed to boundary effects (3.13). For higher values of $\tilde{A}$, the isotropic state becomes the sole stable configuration, while for $\tilde{A} < A_{sp}^{-}$, it is modulated by the Gaussian.

Chapter 4

Universal Description of Rings Patterns in Dynamical Systems

This chapter offers a comprehensive exploration of ring patterns in nonlinear systems. The previous chapter, discuss about the observation of emergence, and stabilization of ring patterns within a DDLCC experiment. To elucidate this phenomenon, a theoretical model is proposed and studied. However, it is important to note that ring patterns extend beyond the discussed experiment and manifest in various nonequilibrium systems.

Nonlinear systems undergoing nonequilibrium processes often manifest dissipative structures in nature [2, 1, 64, 10]. Throughout history, pattern formation is observed in diverse natural phenomena, including the creation of mountains, dunes, plants, clouds, snowflakes, stalactites, and the distinctive skin patterns of mammals, insects, fish, and seashells [64, 10, 9, 65, 66].

Patterns, in a general sense, are dominated by a characteristic wavelength. This wavelength is often shaped by two primary mechanisms: external factors, such as the geometric properties of the system (width, thickness, etc.), and internal factors, like transport, diffusion, and diffraction. Notably, the intrinsic length associated with the latter mechanism, proposed by Turing [30], significantly contributes to shaping patterns.

Concentric ring patterns, observed across various contexts, serve as an illustrative example in the DDLCC experiment. Despite their prevalence in physical systems, concentric ring patterns are commonly considered unstable from the perspective of amplitude equations [17, 67]. Consequently, the precise mechanisms governing the origin and properties of these patterns were not completely understood.

In summary, this chapter demonstrate that concentric ring patterns exhibit stability beyond the Turing instability. Specifically, this phenomenon occurs either after or before a Turing instability, rather than precisely at its onset. Employing a prototype mathematical model for pattern formation, we provide evidence that these solutions can indeed be stable. Additionally, we identify the crucial ingredients necessary for their stability.

4.1 2D Swift-Hohenberg prototype model

The Swift-Hohenberg equation [28, 29, 58] serves as a prototype model for pattern formation [18]. This isotropic and reflection symmetric nonlinear equation features a real order parameter. Applicable to a large variety of systems experiencing spatial symmetry-breaking instability—commonly known as Turing instability [1, 64, 10] it becomes particularly relevant in proximity to a second-order critical point, demarcating the initiation of a hysteresis loop denoted as a Lifshitz point [10, 48]. The formulation of the Swift-Hohenberg equation follows:

$$\frac{du}{dt} = \varepsilon u - u^3 - \nu\nabla^2 u - \nabla^4 u, \tag{4.1}$$

In the given equation $u = u(x, y, t)$, where u represents a real scalar field, x and y denote spatial coordinates, and t signifies time. The interpretation of the scalar field $u = u(x, y, t)$ varies depending on the specific context in which this equation has been derived. It could represent the electric field, molecular orientations, phytomass density, chemical concentration, or other physical quantities.

The parameter ε serves as a control or bifurcation parameter, measuring the input field amplitude, aridity parameter, or chemical concentration depending of the context. Cubic term account for nonlinear saturation or response. Additionally, the parameter ν corresponds to the diffusion coefficient, where $\nu < 0$. When $\nu > 0$, it induces an antidiffusion process, characterized by the emergence of patterns with a characteristic wavelength [11]. Finally the last term, accounts the hyper-diffusion of the system.

4.1.1 Stability Analysis and Amplitude Equation

To analyze this model, it is necessary to calculate its solutions and check their stability. The homogeneous solutions are $u = 0$ and $u_\pm = \pm\sqrt{\varepsilon}$. Stability can be investigated through a linear analysis.

For $u = 0$, assuming a small perturbation $u = u_0 e^{i\vec{k}\cdot\vec{r}+\sigma t}$ with $u_0 << 1$, the dispersion relation is given by:

$$\sigma = \varepsilon + \nu k^2 - k^4, \tag{4.2}$$

where $k = |\vec{k}|$. Utilizing relations that account for the critical length $d\sigma/dk|_{k_c} = 0$ and spatial instability $\sigma(k_c) = 0$, we obtain:

$$k_c = \sqrt{\frac{\nu}{2}} \quad \text{and} \quad \varepsilon_{c_0} = -\frac{\nu^2}{4}, \tag{4.3}$$

indicating that for $\varepsilon > \varepsilon_{c_0}$, a spatial instability (Turing instability) emerges from this point generating a stripe pattern solution with a wave number $\sqrt{\nu/2}$.

To gain a deeper understanding, it is necessary to employ a single-mode ansatz, particularly when ring patterns are expected. The 2D ansatz takes the form [10]:

$$u(r,t) \approx A\left(\left|\varepsilon + \frac{\nu^2}{4}\right| t\right) e^{ik_r r} + \text{c.c.} + \text{h.o.t.} \tag{4.4}$$

It's important to highlight that this ansatz is valid only in the vicinity of the Turing instability. This leads to the result for the two-dimensional amplitude equation calculating at dominant order $e^{ik_r r}$:

$$\frac{dA}{dt} = \left(\varepsilon + \frac{\nu^2}{4}\right) A - 3A|A|^2. \tag{4.5}$$

Given that the Turing point is $\varepsilon_{c_0} = -\nu^2/4 < 0$. The amplitude equation reveals a supercritical bifurcation for $\varepsilon_c = -\nu^2/4$ and this equation have as solution :

$$A_\pm = \pm\sqrt{\frac{\varepsilon}{3} + \frac{\nu^2}{12}}, \quad A_0 = 0., \tag{4.6}$$

In this context, $A_\pm$ only exist as a real solution for $\varepsilon > \varepsilon_{c_0} = -\nu^2/4$. This is illustrated in Fig. 4.1(a). Close to the Turing instability, the concentric rings are unstable due to the interaction of spatial modes. It's noteworthy that a ring pattern structure lacks stability in radius, as observed in Fig. 4.2.

It is crucial to emphasize that, despite the unstability of mono-modal solutions, patterns can still emerge due to multi-modal interactions [10].far from the instability, the modal theory can not explain the observed evidence of stable ring patterns for $\varepsilon > 0$.

In order to continue with the positive ε region, considering the solutions $\pm\sqrt{\varepsilon}$, as this model lacks any non-variational term, it becomes evident that both solutions exhibit symmetry with respect to the x-axis. Consequently, the stability analysis can be conducted for one of these solutions, allowing to draw conclusions that apply to the other solution as well.

For $\sqrt{\varepsilon}$, introducing a small perturbation into the equation $u = \sqrt{\varepsilon} + e^{i\vec{k}\cdot\vec{r}+\sigma t}$ yields the following dispersion relation:

$$\sigma = -2\varepsilon + \nu k^2 - k^4. \tag{4.7}$$

Applying the same relations to determine the critical values are obtained:

$$k_c = \sqrt{\frac{\nu}{2}} \quad \text{and} \quad \varepsilon_{c_1} = \frac{\nu^2}{8}, \tag{4.8}$$

Signifying that the solution $u = \sqrt{\varepsilon}$ is stable for $\varepsilon > \nu^2/8$, similarly, $u = -\sqrt{\varepsilon}$ demonstrates analogous stability. Additionally, the system exhibits bistability between the uniform solutions and the pattern states. This analysis is depicted in Figure 4.1(a) showing the bifurcation diagram.

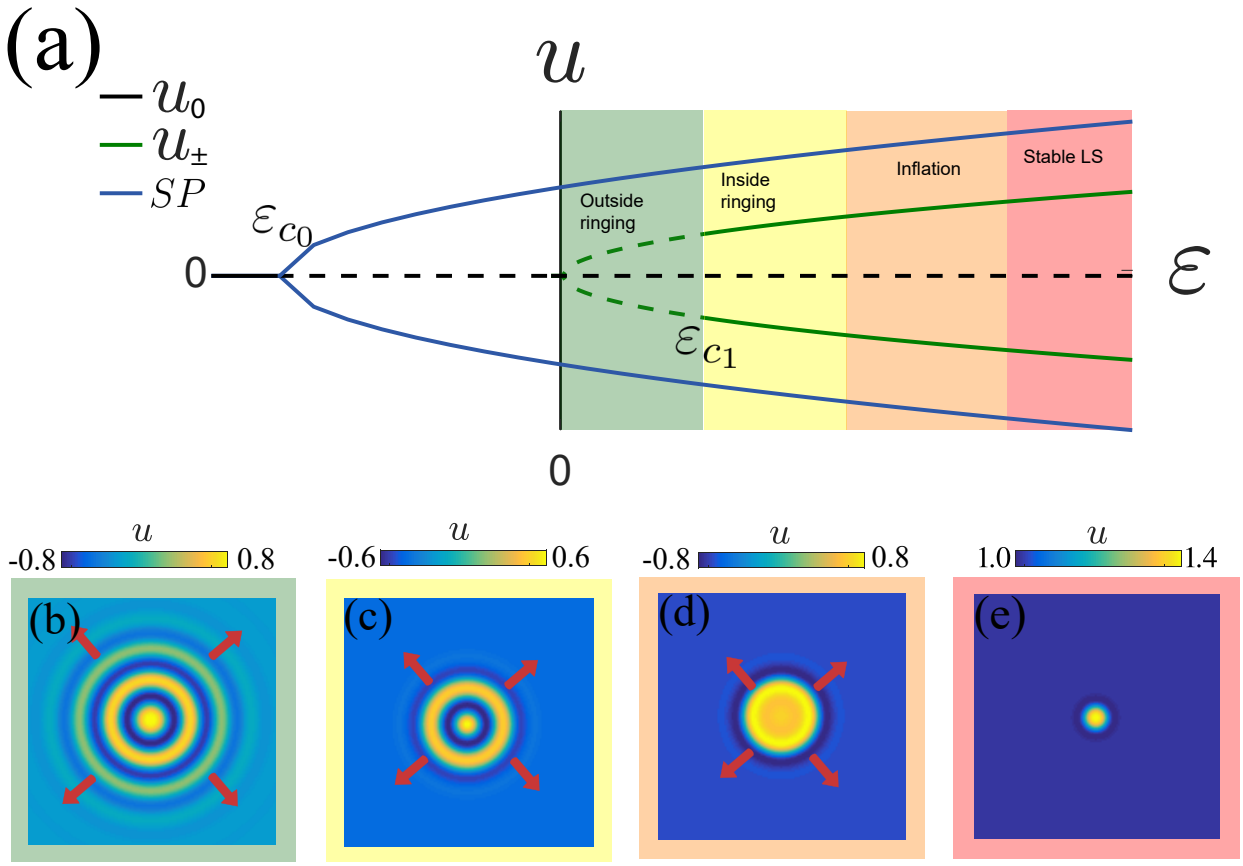

Figure 4.1: (a) Bifurcation diagram of the Swift-Hohenberg Equation: Maximum value of u versus ε. The green line corresponds to $\pm\sqrt{\varepsilon}$ states, the blue curve represents a single-mode pattern (SP), and the black line signifies the zero solution. Dashed and solid lines indicate that the corresponding state is unstable and stable, respectively. Simulations shows different stable structures when the homogeneous solution exist with $\nu = 1$: (b) Outside ringing, (c) Inside ringing, (d) Inflation, (e) Stable localized structure (LS).

Numerically, is considered the uniform state $-\sqrt{\varepsilon}$, and perturbing it locally with a Gaussian function as initial condition(with a width of the pattern wavelength, see Fig. 4.1(e)), in this case this perturbation just can be implemented when $\varepsilon > 0$, where is possible to connect two homogeneous state. Depending on ε, are observed different behaviors.

In the region where uniform states doe not exist ($\varepsilon_{c_0} \leqslant \varepsilon \leqslant 0$), is observed the propagation of unstable concentric rings . This propagation is distinguished by the emergence of outer rings that become attached. Concurrently, concentric rings begin to destabilize (Fig. 4.2). To ensure that this destabilization is not a boundary effect, the boundaries are set as free conditions for $r = R$.

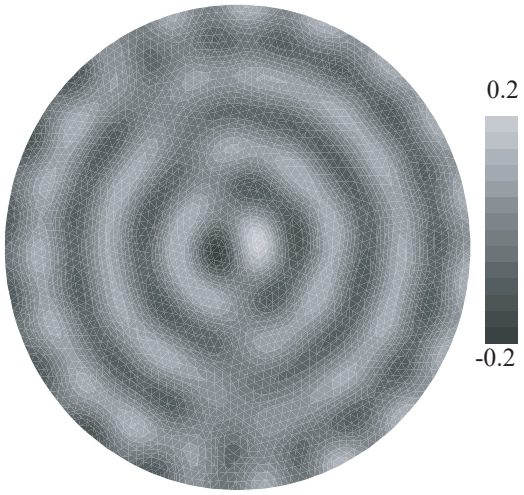

Figure 4.2: Unstable ring pattern simulation for $\varepsilon \in [\varepsilon_{c_0}, 0]$ and $\nu = 1$

As ε increases, the dynamics change. Initially, observing a propagation similar to the previously described scenario, featuring stable concentric ring patterns (for $0 < \varepsilon < \varepsilon_{c_1}$, Fig. 4.1(b)). The parameter ε in Fig. 4.1(a) characterizes the spatial region where this behavior is observed, termed "outside ringing." With further increments in ε and the system residing in the bistability region, the propagation takes on a distinct form. Rings emerge from the center, displacing the concentric ring structure (Fig. 4.1(c)), occurring for $\varepsilon_{c_1} < \varepsilon$. This region is labeled "inside ringing."

Upon further increases in ε, the system no longer exhibits the formation of a concentric ring pattern. Instead, there is a propagation of one homogeneous state over the other, denoted as the "inflation" region (Fig. 4.1(d)). As ε continues to rise, the initial perturbation stabilizes into a localized structure (Fig. 4.1(e)). Additionally, numerical simulations consider a circular geometry to mitigate edge effects and investigate the stability of concentric ring patterns.

It is noteworthy that stable concentric ring patterns are observed beyond Turing instability $\varepsilon > \varepsilon_{c_1} >> \varepsilon_{c_0}$). This observation may be associated with a shift in the Turing boundary resulting from the axisymmetric (radial) constraint on the initial condition. Numerical simulations were performed using the RK4 algorithm for time integration and a finite-difference scheme for spatial discretization.

4.2 1D Model Reduction

To gain insight into concentric ring patterns, a one-dimensional model that incorporates essential elements—curvature, bistability, and a characteristic wavelength—to observe these patterns and their dynamics is deduced from the rotation invariance of patterns, proposing the ansatz $u(x, y, t) = u(r, t)$, where r is the radial coordinate. Consequently, Eq. 4.1 can be re-expressed as

$$\frac{du}{dt} = \varepsilon u - u^3 - \nu \left(\frac{1}{r}\frac{d}{dr} + \frac{d^2}{dr^2} \right) u - \left(\frac{1}{r^3}\frac{d}{dr} - \frac{2}{r^2}\frac{d^2}{dr^2} + \frac{2}{r}\frac{d^3}{dr^3} + \frac{d^4}{dr^4} \right) u. \tag{4.9}$$

The Eq. 4.9 is an one-dimensional Swift-Hohenberg model with curvature. The presence of terms $1/r^n$ are corrections due to the dimension reduction. Within this model, the impact of curvature is regulated by terms that are inversely proportional to powers of r. This formulation offers solutions comprising uniform states $\mu = \{0, \pm\sqrt{\varepsilon}\}$ and distinct one-dimensional patterns, specifically manifesting as concentric ring states. The meaning of the critical value $\varepsilon = \varepsilon_{c_0} = -\nu^2/4$ becomes evident, representing the threshold for Turing instability—signifying a supercritical spatial instability within the context of Eq. 4.9 [64, 10].

This model, incorporating curvature, captures the essence of ring pattern formation to trying to explain the previous observed behaviours. The critical value ε_{c_0} serves as a trigger of the phenomena, indicating the onset of Turing instability and the evolution of distinct patterns. This comprehensive understanding set the first step to explore the dynamics of concentric ring patterns in one-dimensional systems, offering valuable insights about mechanisms that drive spatial instabilities.

For our simulations, the initial conditions are carefully chosen to capture the dynamics of the concentric ring patterns. The characteristic wavelength, denoted by λ_c and defined as twice the characteristic wave number, is expressed as $\lambda_c = 2\pi/k_c = \pi\sqrt{8}/\sqrt{\nu}$ with $\nu = 1$. This ensures that the simulations encompass the relevant spatial scales for the system under consideration. The chosen initial conditions involve a Gaussian perturbation ($u_G(0, r)$) and a domain wall ($u_{DW}(0, r)$), both of which are set to connect the homogeneous solutions $-\sqrt{\varepsilon}$ and $\sqrt{\varepsilon}$:

$$u_G(0, r) = -\sqrt{\varepsilon} + 2\sqrt{\varepsilon} e^{\frac{-r^2}{32\pi^2}}, \tag{4.10}$$

$$u_{DW}(0, r) = -\sqrt{\varepsilon} + 2\sqrt{\varepsilon} H(r). \tag{4.11}$$

Here, $H(r)$ denotes the Heaviside function, defined as $H(r < 0) = 0$ and $H(r \geqslant 0) = 1$. These initial conditions serve to initiate the simulation with a Gaussian perturbation and a domain wall, respectively, providing insight into how the system evolves from these distinct starting configurations. The careful selection of initial conditions enhances the capability of our simulations to capture and elucidate the dynamics of the equations.

4.2.1 No Curvature Dynamics

If the curvature terms are neglected, the equations follows the typical one dimensional Swift-Hohenberg equation, and scenarios where curvature effects are disregarded, patterns propagate by giving rise to spatial oscillations at the end of the pattern.

$$\frac{du}{dt} = \varepsilon u - u^3 - \nu\frac{d^2u}{dr^2} - \frac{d^4u}{dr^4} \tag{4.12}$$

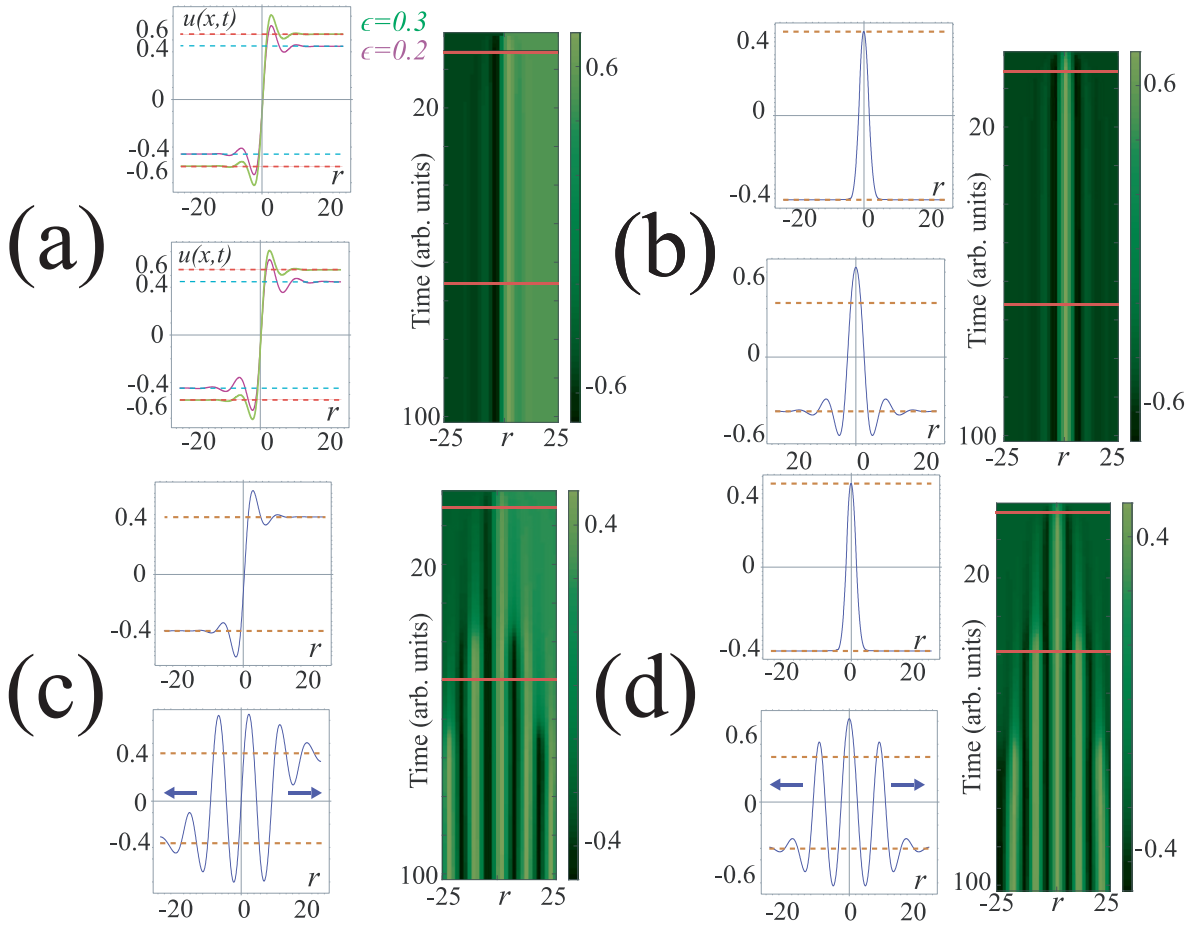

Figure 4.3: Domain walls and localized structures of the one-dimensional Swift-Hohenberg Eq. 4.12 for $\nu = 1$, without curvature corrections. (a) Domain wall profile and spatiotemporal evolution between symmetrical uniform states $u = \pm\sqrt{\varepsilon}$ for $\varepsilon = \{0.2, 0.3\}$. (b) Profiles of localized structures and spatiotemporal evolution ($\varepsilon = 0.2$). (c) Pattern propagation from a domain wall solution ($\varepsilon = 0.15$) or a (d) localized structure ($\varepsilon = 0.15$). The red lines on the spatiotemporal diagram show the instant where the profiles are obtained. The dashed horizontal lines account for the homogeneous equilibria.

Figure 4.3 illustrates pattern propagation in the absence of curvature by integrating Eq. 4.12 across the entire spatial range (negative and positive values of r). This behavior resembles that observed in concentric ring patterns in two dimensions in the outside ringing region, as depicted in Fig. 4.1(a).

For ε within the bistability region between uniform and pattern states, the system exhibits a domain wall solution connecting two symmetric states (Fig. 4.3(a)). The amplitudes of damped spatial oscillations increase with ε.

Additionally, the model Eq. 4.12, without curvature effects, produces localized structures for higher values of ε, supported by homogeneous states (Fig. 4.3(b)). As ε decreases, the pattern state becomes more stable than the homogeneous one, initiating pattern propagation from the center of the domain wall or the localized structure (bottom panels of Fig. 4.3(c) and 4.3(d), respectively).

Noteworthy that the existence of the concentric pattern persists, independent if the initial condition is a Gaussian or any other form. However, when the parameter ε is in the localized structures region, the evolution of the pattern is characterized by does not change the shape of the initial condition.

4.2.2 Curvature Effect

The dynamic behavior shows a significant change when curvature effects exist. Is possible to observe a localized structure with a pattern propagation is characterized by the emergence of spatial oscillations outside the pattern, for ε in the outside ringing region, comparing with the case without curvature effects (Fig. 4.4(a)). However, as ε increases, transitioning to inside ringing region, the propagation dynamics change dramatically. Spatial oscillations initiated at the center of the perturbation, subsequently giving rise to new oscillations at the center (Fig. 4.4(b)). Upon further increasing ε, the curvature-induced effect becomes evident as one homogeneous state invades the other, as illustrated in Fig. 4.4(c).

The observed dynamic behavior aligns with the characteristics of the inflation region depicted in Fig. 4.1(a). With a further increase in ε, stable localized structures emerge, and propagation of patterns or homogeneous states is no longer observed (Fig. 4.4(d)). The solutions shown in Fig. 4.3 were obtained through numerical integration for $r > 0$, with reflection at $r = 0$ (RK4).

The interplay between curvature and bistability, involving uniform and pattern states, lets the stabilization of propagating concentric ring patterns. Transitioning from the inflation mode to a stationary localized structure, as previously reported [29], elucidates the role of curvature in phase domain dynamics within the context of a Swift-Hohenberg model. It is crucial to note that in scenarios characterized by inside and outside ringing (Fig. 4.1(a)), the local approximation using amplitude equation becomes invalid. Consequently, the dynamics of concentric ring patterns depends on nonlocal interactions, showing the complexity of their behavior.

This study demonstrates the stability of concentric ring patterns beyond the Turing instability. The essential prerequisite for the manifestation of these patterns is the bistability between patterns and homogeneous states. Utilizing the Swift-Hohenberg equation as a prototype model, the stability of these solutions is established, identifying the main ingredients for their existence. Close to the Turing instability, the concentric rings experience instability due to the interaction of spatial modes.

However, beyond the Turing instability, these patterns can be stabilized and showing a characteristic wavelength induced by the spatial instability. The proposed mechanism of pattern formation, namely inside ringing, is triggered by curvature effects. This mechanism is supported by theoretical findings, affirming the emergence of stable concentric ring patterns in the inside ringing region.

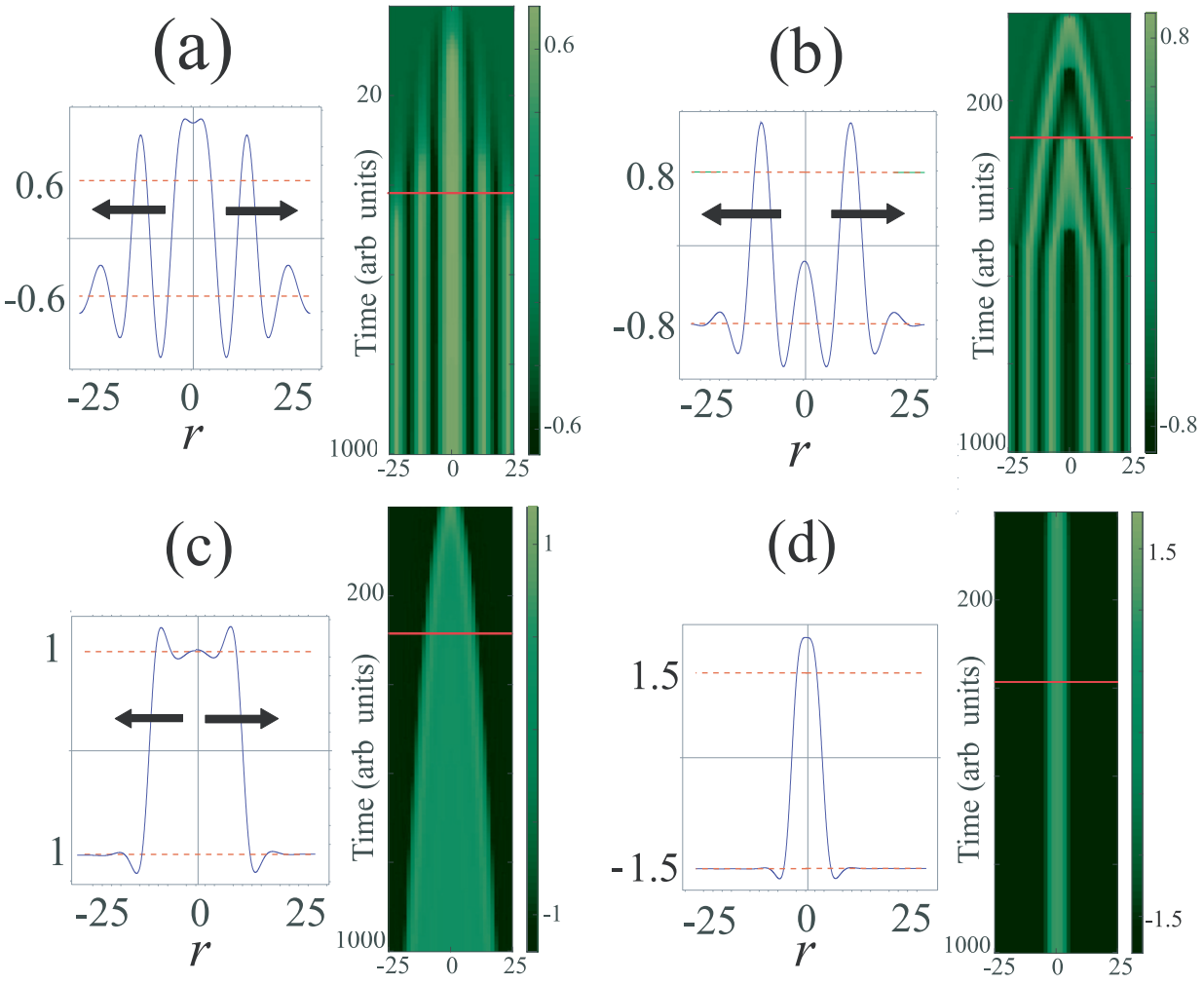

Figure 4.4: Pattern propagation and profiles from a localized structure of the one-dimensional Swift-Hohenberg model Eq. (2) for $\nu = 1$. (a) Depicts pattern propagation for $\varepsilon = 0.1$ with spatial oscillations in the outer part of the pattern. (b) Illustrates pattern propagation for $\varepsilon = 0.2$ characterized by spatial oscillations emerging from the center and pushing the pattern structure outward. (c) Shows front propagation of one homogeneous state over the other, for $\varepsilon = 0.5$. (d) Presents stable localized structures for $\varepsilon = 0.9$. The red lines on the spatiotemporal diagrams indicate the instant when the profiles are obtained. The dashed horizontal lines represent the homogeneous equilibria. The domain of integration is from $r = 0$ to $r = 25$, reflected at $r = 0$.

4.2.3 N^{th} Dimensional Ring Patterns

In the previous sections, the emergence and propagation for a two-dimensional system were discussed. It is possible to generalize this explanation to an N-dimensional system using the same idea. Consider a prototype model in N dimensions, and impose $N-1$ constraints related to angular symmetries. The model simplifies to a one-dimensional equation, as shown before. Let's analyze this in the same way, using an n-coordinates system [68]:

$$\begin{aligned}
x_1 &= r\cos(\varphi_1),\\
x_2 &= r\sin(\varphi_1)\cos(\varphi_2),\\
x_3 &= r\sin(\varphi_1)\sin(\varphi_2)\cos(\varphi_3),\\
&\vdots\\
x_{n-1} &= r\sin(\varphi_1)\cdots\sin(\varphi_{n-2})\cos(\varphi_{n-1}),\\
x_n &= r\sin(\varphi_1)\cdots\sin(\varphi_{n-2})\sin(\varphi_{n-1}).
\end{aligned}$$

This case is described by the inverse transformation:

$$\begin{aligned}
r &= \sqrt{x_n^2 + x_{n-1}^2 + \cdots + x_2^2 + x_1^2},\\
\varphi_1 &= \operatorname{atan2}\left(\sqrt{x_n^2 + x_{n-1}^2 + \cdots + x_2^2}, x_1\right),\\
\varphi_2 &= \operatorname{atan2}\left(\sqrt{x_n^2 + x_{n-1}^2 + \cdots + x_3^2}, x_2\right),\\
&\vdots\\
\varphi_{n-2} &= \operatorname{atan2}\left(\sqrt{x_n^2 + x_{n-1}^2}, x_{n-2}\right),\\
\varphi_{n-1} &= \operatorname{atan2}\left(x_n, x_{n-1}\right).
\end{aligned}$$

Where atan2 is the two-argument arctangent function. There the inverse transform is not unique; φ_k for any k will be ambiguous whenever all of $x_k, x_{k+1}, \ldots, x_n$ are zero; in this case, φ_k may be chosen to be zero. The ∇_N should be determined for $N-$spherical system to obtain the curvature corrections ($\propto 1/r^n$) for each $N-$dimensional system.

It is important to note that the homogeneous solutions and the mono-modal pattern, along with their calculated stabilities as discussed earlier, do not depend on curvature effects, this just affect the angular constrain. This observation validates the reduction of the model to one dimension ($1D$) for N^{th} ring patterns if system presents bistability, curvature effects, and a characteristic wavelength, the $1D$ model remains a valid representation of the system.

The process of dimension reduction opens avenues for studying various systems. In the context of LC systems, this reduction holds promise for creating some optical devices like adaptive irises. Here, parameters can be controlled both during manufacturing and through external pumping mechanisms, as was discussed in Chapter 3.

Chapter 5

Phase Separation Close to NI Transition.

This chapter delves into the experimental observations and numerical modeling of a Dye-Doped Liquid Crystal Cell (DDLCC) under temperature control. In contrast to Chapter 3, where the DDLCC was examined without temperature variations, this study introduces a controlled temperature element to the experimental setup, not considering a light pump on the cell. Furthermore, a detailed phenomenological model is developed based on first principles, aiming to comprehend the physical system.

This configuration introduces a new molecular component, leading to distinct behaviors, particularly close to the nematic-isotropic transition (NI). This experiment draws a comparison between a DDLCC and a typical Nematic Liquid Crystal (NLC), unveiling intricate behaviors during the transition—specifically, a phenomenon called phase separation [24]. Phase separation manifests in the form of two spatial inhomogeneities: bubbles or spinodal decomposition, indicating the coexistence of different molecular concentrations within the system.

To elucidate this intricate behavior, employing a coupled model between Landau-deGennes and Cahn-Hilliard equations to add mass conservation in the system. This modeling approach offers valuable insights into the mechanisms governing the observed phase separation phenomena.

5.1 Experimental observations

5.1.1 Experimental Setup

Employing a planar anchoring cell with either an E7 nematic liquid crystal (NLC) or the previously introduced DDLC (discussed in preceding chapters) between two glass plates, each with a thickness of 25 μm. A typical approach for studying the NI transition involves the use of optical microscopy, thermal control, and cross-polarization, as illustrated in Fig.

5.1.

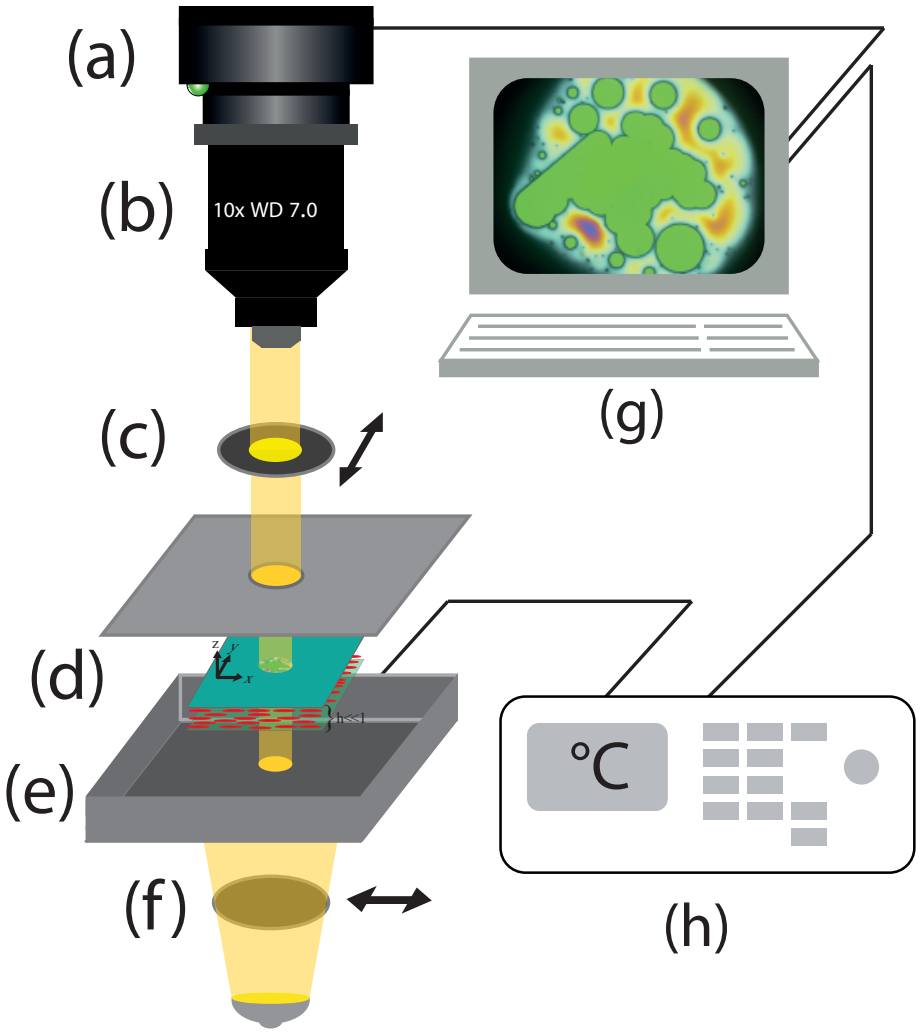

Figure 5.1: Experimental setup for phase separation, illustrating the following components: (a) CCD camera, (b) 10x optical objective, (c) & (f) polarizers setted for cross polarization, (d) DDLCC or NLC sample, (e) & (h) thermal chamber and control device. Finally, (g) represents the computer for controlling the thermal device and receiving images from the CCD camera.

In the experimental setup, temperature control is facilitated using the Linkam software [69], while imaging is acquired through the ThorCam software [70]. This process occurs subsequent to cross-polarization and employs a 10x magnification objective.

To study this system, the thermal chamber is programmed with a temperature ramp of $0.1°C/min$ from $56°C$ to $61°C$. This setup enables the examination of cell behavior (E7 or DDLCCs) in the vicinity of the critical temperature T_c. Comparative analysis of snapshots representing distinct states is conducted until the isotropic state completely pervades the system (see Figure 5.2).

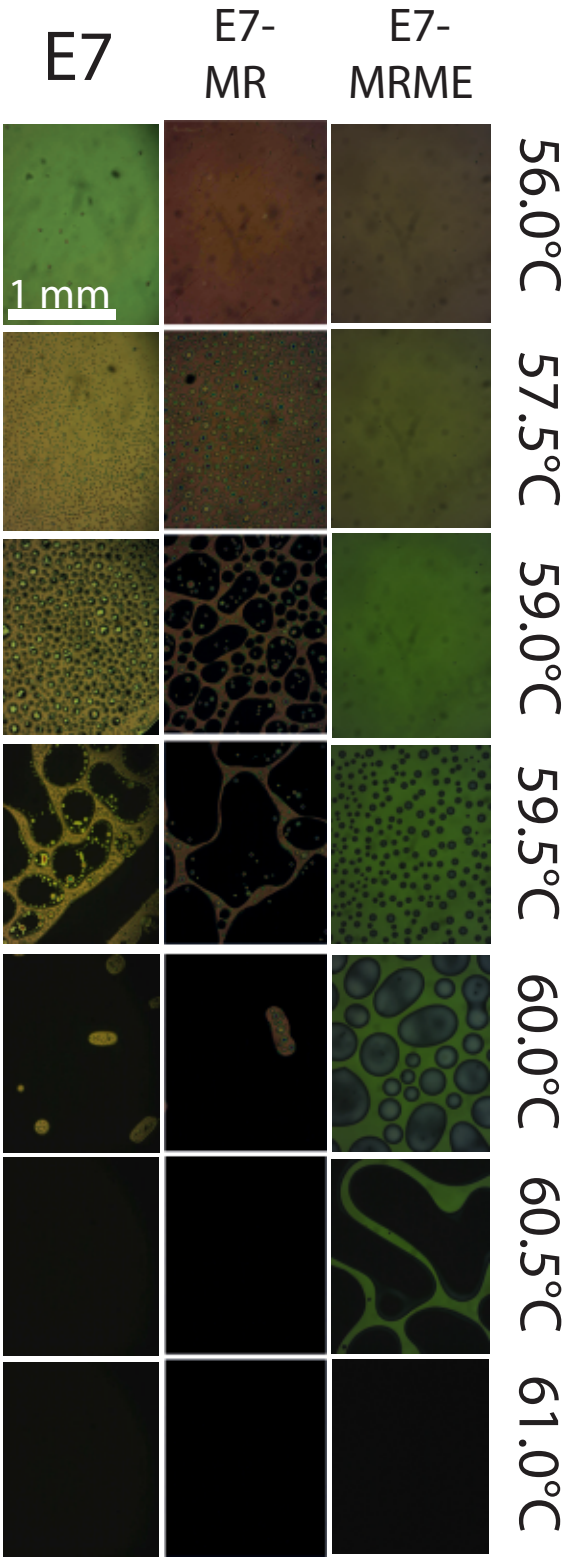

Figure 5.2: Experimental snapshots, of the spatial behaviour for E7, E7-MR, and E7-MRME mixtures, where the DDDLCC are composed by 99% of E7 LC and 1% of Dye-Dopant. The different states are induced by a temperature ramp of $0.1°C/min$.

In Figure 5.2, the comparison of different states across the three mixtures reveals a notable observation. The isotropic state invades the system at a lower temperature than expected (traditionally at 61.0° for E7 [33, 34, 35]), indicating that the presence of the dopant in the mixture alters the system's critical temperature and the observed dynamics. An even more significant finding is the emergence of a distinct nematic phase as bubbles coexist before the isotropic phase takes over, persisting alongside the regular nematic phase, resulting in the coexistence of three states simultaneously (from $57.5°C$ to $60.0°C$).

Due to the utilization of a temperature ramp, distinguishing between various behaviors is challenging. However, it is possible to check that at temperatures below $59.0°C$, the DDLCCs exhibit only two distinct nematic phases. Between $59.0°C$ and $60.0°C$, three states coexisting, and at higher temperatures, the isotropic state invades the system. On the other hand, pure E7 LC demonstrates a singular nematic phase up to $59.0°C$, with observable isotropic bubbles after that temperature Note that the observation of the bubbles is unexpected, because this is a manifestation of a typical wavelength which is not included on Landau-deGennes theory. As the temperature rises, these bubbles invades the system, and finally goes to the isotropic at the critical temperature T_C. The delineation of these temperature ranges is crucial for the ongoing exploration of this phenomenon. In regions where only two nematic bubbles coexist, the occurrence can be characterized as a "phase separation" phenomenon. For the E7 mixture, it is imperative to investigate the potential presence of this phenomenon since bubbles are observed at temperatures below T_c.

5.1.2 E7 Phase Separation

Given the observed diverse behaviors, it becomes imperative to conduct a detailed examination of both, the DDLCC and the E7 mixture in different temperature ranges. Specifically, for E7, a measurement in the temperature range $T_{ps} < T < T_c$, where T_{ps} signifies the temperature at which bubbles emerge and T_c denotes the temperature of the nematic-isotropic (NI) transition. This targeted study is essential for a comprehensive understanding of the system's behavior within the specified temperature interval.

In this case, the selected temperature is $T = 60.3°C$ for NLC. The study focuses on the system's dynamics, initiating from a nematic state and rapidly reaching the chosen temperature. Subsequently, the system evolves over a duration of 60 hours, and the evolution of the characteristic length is examined over time.

To calculate the characteristic length of the system, a region in the homogeneous mixture is observed, it is essential to isolate the green bubbles and focus solely on their evolution. As a white region surrounds the bubbles, employing image processing techniques allows us to generate binary images of the isolated bubbles, as illustrated in Fig. 5.3(b). This binary image is then compared with the experimental snapshot for analysis.

The characteristic length $L(t)$ is determined using a Fourier method [50], calculating the 2D-structure length from the Fourier transform of the image. Obtaining the probability distribution $p(q,t)$ of q-vectors by integration over all directions. Taking the inverse of the mean value of q over this distribution gives the characteristic length as:

$$L(t) = 2\pi / \left(\int qp(q,t)dq \right) \tag{5.1}$$

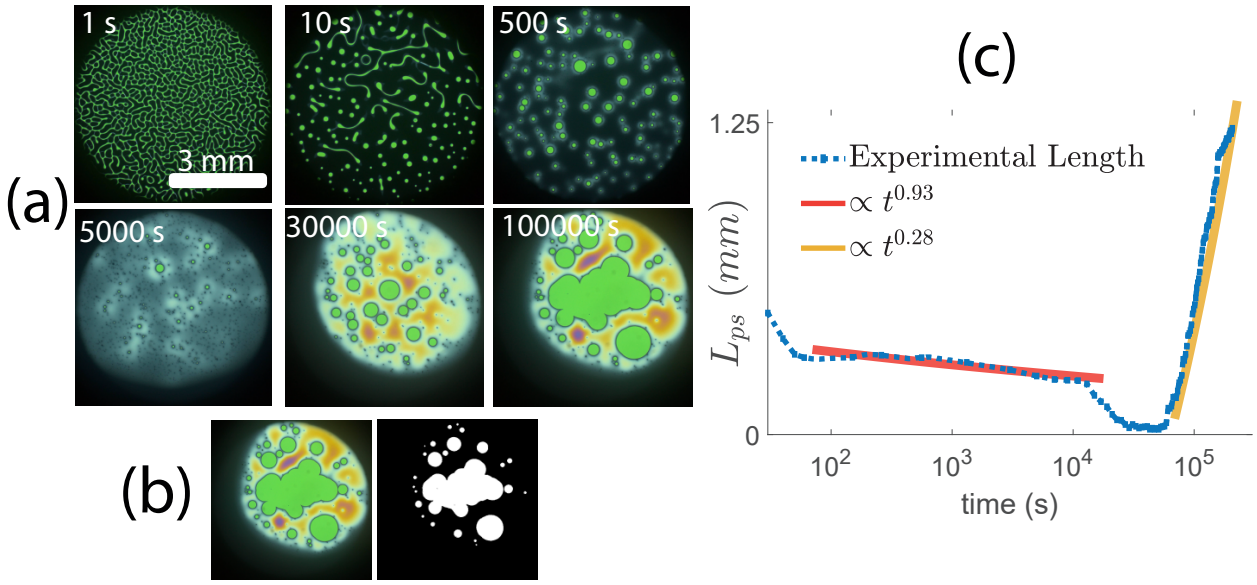

Figure 5.3: Evolution of the E7 liquid crystal sample at a temperature of $60.3°C$. (a) Snapshots at various time points illustrating the emergence and interaction of structures. (b) Binarization of the green nematic structures. (c) Experimental length calculation, along with the exponential fit depicting isotropic front propagation, and the phase separation regimes (represented by orange and yellow curves, respectively).

An important observation is that the evolution is governed by two distinct mechanisms at different stages. Initially, the evolution exhibits an exponent of approximately $-t^1$, indicating a front propagation dynamic of the isotropic state over the nematic one [71], which is typically of front propagation, because the speed is constant.

Subsequently, after a prolonged period (in comparison to the isotropic front time), a new regime emerges involving the interaction of green bubbles. These green bubbles display two intriguing behaviors: interaction with other bubbles and the emergence of a white region around them. The interaction among bubbles is attributed to phase separation dynamics, as evidenced by an exponent in the characteristic length regime of approximately $t^{1/3}$—following the Lifshitz–Slyozov law [48]. The emergence of the white region is attributed to the spatial inhomogeneity of the green structures.

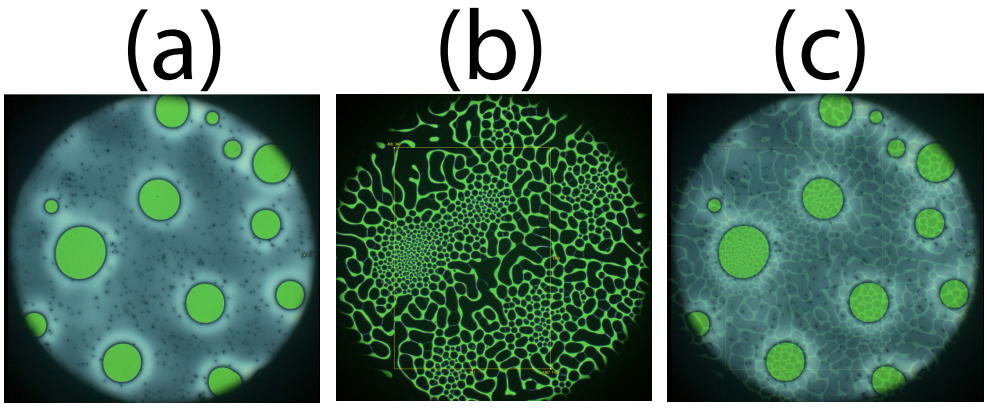

Figure 5.4: Concentration Inhomogeneity: (a) Structures of green bubbles, (b) Emergence of isotropic front initially after cooling down and reheating, (c) Overlapping of (a) and (b).

In this instance, phase separation is not attributed to two distinct liquids or materials, as is commonly observed in several mixtures [24], such as oil and vinegar. Instead, it is attributed to local concentration variations within the sample. Specifically, the green structures would be a different molecular concentration than the rest of the sample, as evident in Fig. 5.4. The emergence of the isotropic front after cooling down, when the bubbles are present in the sample, indicates a modulation of the size of the initial isotropic front by the form of the bubbles. This is distinct from the emergence observed when heating a homogeneous sample (refer to Fig. 5.3 (a)). Addressing this variation becomes crucial for experiment replication, necessitating heating to higher temperatures to restore a homogeneous medium.

5.1.3 DDLCC Phase separation

In this case, the E7-MRME sample is chosen for the experiment due to its brighter colors compared to the E7-MR, which facilitates the study.

To investigate the impact of the dopant in the sample, a similar analysis is conducted. However, executing the experiment becomes challenging due to the coexistence of three states. At a temperature of $56.5°C$, the system is observed to explore Nematic-Nematic interactions (Fig. 5.5(a)), with the experiment lasting for only 8 h. During the initial phase, a new nematic phase emerges over the original one, characterized by front propagation for up to 800 s. Following this, the nematic bubbles over the nematic medium exhibit the Lifshitz–Slyozov law until 8000 s. Subsequently, from 10000 s until the end, certain bubble concentrations become sufficient to induce the NI transition, becoming dominant in the system. The experiment is halted at this point, as the phase separation behavior of a pure liquid crystal was previously discussed in the last section.

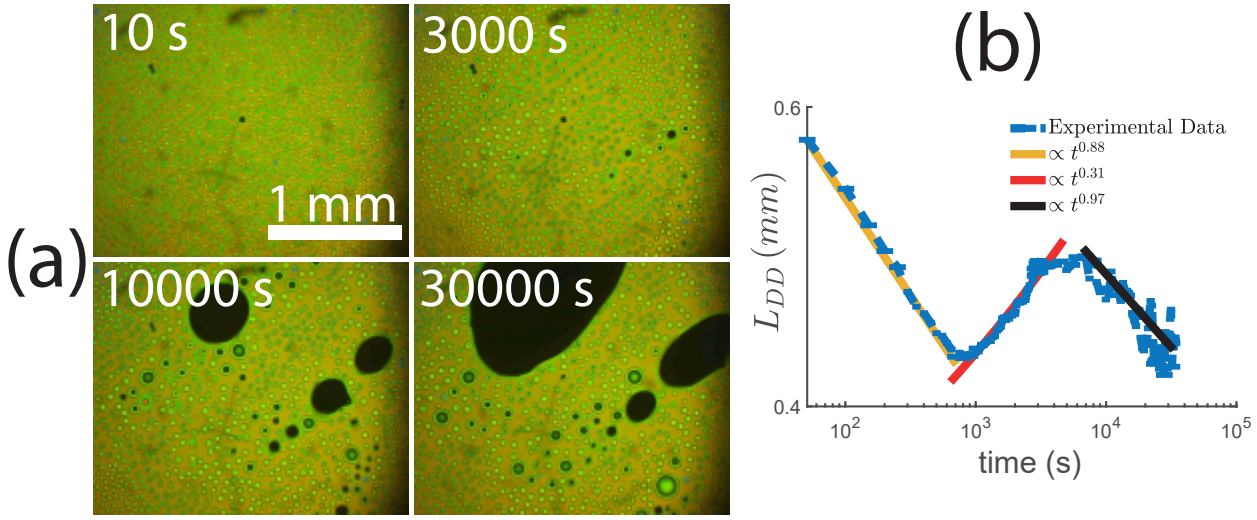

Figure 5.5: Evolution of the MRME-E7 LC sample at a temperature of 56.5°C. (a) Snapshots at various time points illustrating the emergence and interaction of structures. (b) Experimental length calculation, along with the exponential fit depicting nematic-nematic front propagation, phase separation and isotropic front propagation regimes (represented by yellow, red and black curves, respectively).

An important observation is that the presence of nematic-nematic coexistence is a result of the phase separation of the dopant, which modified the transition temperatures compared to the pure LC sample. This allows for the independent observation of the phase separation of the dopant. However, for large enough time, the LC transition and potentially the LC phase separation will become evident. This indicates that the order parameter is intricately linked to the molecular concentration of the LC mixture and the concentration of the dopant in the system, resulting in a triple-coupled system.

One challenge in the experiment is the inability to directly measure local concentration, as transmitted light is proportional to S^2 (order parameter). Thus, the experiment relies on observing the indirect effects of local concentration.

It is noteworthy that the execution of this experiment demands extended measurement times, guided by a slow dynamic process. This show that the understanding of the Nematic-Isotropic (NI) transition and the behavior in proximity to this transition is not entirely comprehensive within the context of liquid crystals. The observed phenomena are more intricate in various aspects than initially expected and not discussed on the litterature. Note that the NI transition is one of more relevant transitions in liquid crystal.

5.2 LC Phase Separation Model

To elucidate the dynamics of the previous experiment, the Cahn-Hilliard equation [47] is employed to describe the evolution of molecular concentration N, and is coupled with the Landau-deGennes equation for the order parameter S [4]. For simplicity, the model is initially applied to a pure liquid crystal (LC).

The Cahn-Hilliard model, being mass-conservative, is represented by the equation [47]:

$$\frac{dN}{dt} = \nabla^2 \left(\mu N - N^3 - \nabla^2 C\right) \tag{5.2}$$

Here, $\mu = \mu(T)$ is temperature-dependent parameter that account for diffusion, and $N = N(\vec{r}, t)$ signifies the deviation from the average concentration N. On the other hand, utilizing a typical Landau-deGennes equation for the order parameter S coupled with the concentration follows:

$$\tau \frac{dS}{dt} = -(\varepsilon + \alpha(N_0 + N))S + \beta S^2 - S^3 + \nabla^2 S \tag{5.3}$$

Here, τ represents the timescale of the phase separation, N_0 is the initial homogeneous concentration and α represents the coupling between concentration variation and the order parameter (Note that the change in the concentration induce a change of the parameter value for the NI transition), while the other parameters were previously discussed in this dissertation.

The timescale since the experiment show that the phase separation regime occurs after a long time, is setted for big values of τ, because the S parameter does not reach the isotropic state before the phase separation regime.

The coupled system for the phase separation is given by:

$$\begin{aligned} \tau \frac{dS}{dt} &= -(\varepsilon + \alpha(N_0 + N))S + \beta S^2 - S^3 + \nabla^2 S \\ \frac{dN}{dt} &= \nabla^2 \left(\mu N - N^3 - \nabla^2 C\right). \end{aligned} \tag{5.4}$$

It is crucial to note that when dealing with more than one separable medium, such as in the case of DDLCC, it becomes necessary to introduce multiple $N_i(\vec{r}, t)$ terms. Each separable medium in the system is denoted by the index $i = 1, ..., n$, where n represents the total number of such mediums.

5.2.1 Model Simulation

Here is study the numerical simulation of the model 5.4. For this simulations, which necessitates mass conservation in the N equation, a 2D spectral method [53] is employed. The chosen parameters include $\tau = 100$, $\varepsilon = -0.2$, $\alpha = 0.2$, $N_0 = 1$, $\beta = 0$, and $\mu = 0.1$, with homogeneous initial conditions $N(\vec{r}, 0) = 0$ and $S(\vec{r}, 0) = 1$. The colors are selected to facilitate comparison with experimental observations (black, white, and green in gradient). the parameter and variables are in arbitrary units. Evolution of the simulation is presented in Fig. 5.6.

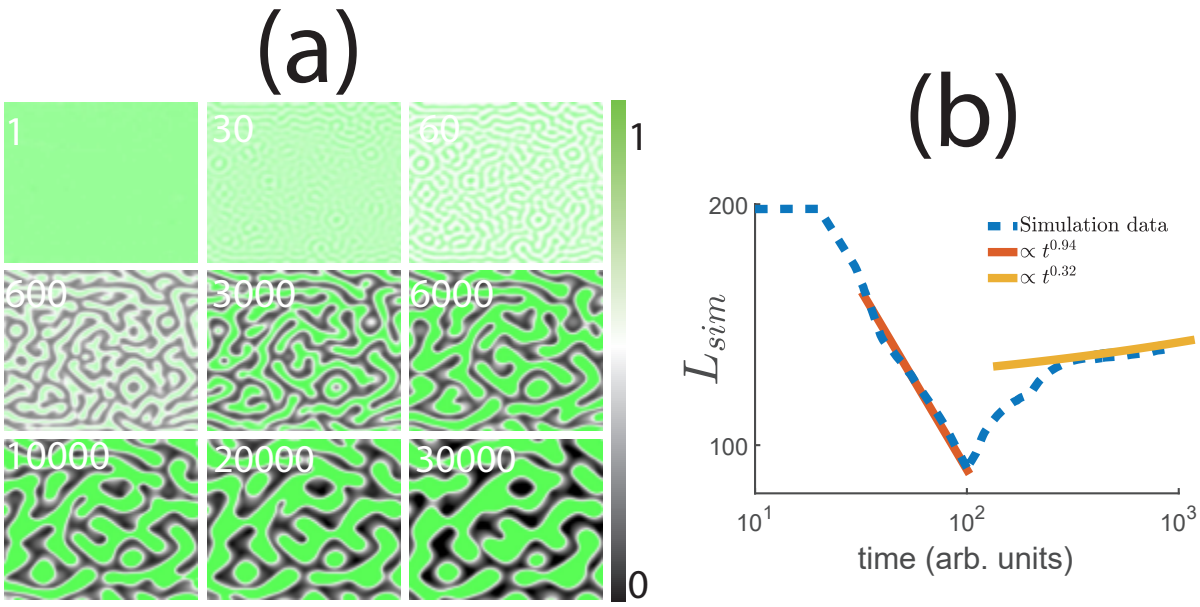

Figure 5.6: Evolution of the S field phase separation coupled model (Eq. 5.4). (a) Snapshots at various time points illustrating the emergence and interaction of structures. (b) Characteristic length calculation, along with the exponential fit depicting front propagation and phase separation regimes (represented by orange, red, and yellow, respectively).

It is crucial that the simulated curve exhibits a behavior similar to the experimental one, revealing a regime change around $t = \tau = 100$. This suggests that this factor could be associated with the timescale between the regimes. In both regimes, the curves display a front propagation law and an approximate Lifshitz–Slyozov law. The calculation of the characteristic length is conducted by excluding the white area around the green structures.

The dynamics presented in this model simulation aligns with experimental observations. However, is important to consider to improve the model, particularly, because the order parameter does not currently affect the concentration equation.

5.2.2 Effect of Non-Homogeneous Parameters in Landau-DeGennes Model

Since both equations in the model have different time scales, it is possible to approximate $N(\vec{r},t) \approx N(\vec{r})$. To comprehend the impact of structures induced by phase separation and the white region around these structures, analyzing the Landau-deGennes equation:

$$\tau\frac{dS}{dt} = -(\mu + \alpha N(r))S + \beta S^2 - S^3 + \vec{\nabla}^2 S \tag{5.5}$$

where

$$N(r) = N_1 + N_2\frac{e^{-(r^2/r_0^2)}}{\delta_0 + e^{-(r^2/r_0^2)}} \tag{5.6}$$

.

In Fig. 5.7(a) is shown the profile of $N(r)$ in radial coordinate. Essentially, this converts into a localized spatial modulation of the linear parameter connecting N_1 with $N_1 + N_2$. It is important to choose $\delta_0 << 1$ to create a function resembling a structure that connects just two states sharply (Figure 5.7(a)).

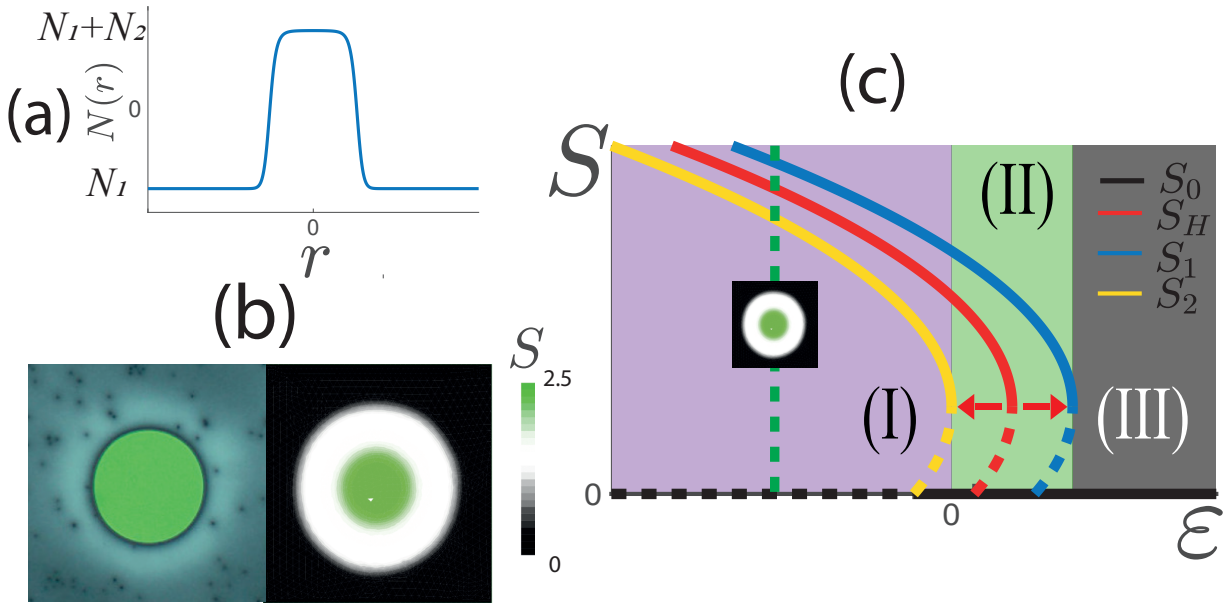

Figure 5.7: Effect of Inhomogeneous Structure: (a) Inhomogeneity connecting two symmetric states, (b) comparison between the experimental structure and the numerical simulation showing a white region around the green structure,(c) splitting in the bifurcation diagram (the red line disappear emerging two possible new curves depending of the local value of concentration).

Analyzing the stability of this solution, is possible to separate it in two regimes, essentially locally changing the effective value of ε in the Landau-deGennes equation, as shown in Figure 5.7(b).

This implies that three different states $S = S_1$, $S = S_2$, and $S = 0$ are coexisting in this simplified model, where:

$$S_1 = \frac{\beta + \sqrt{\beta^2 - 4(\mu + \alpha N_1)}}{2} \tag{5.7}$$

$$S_2 = \frac{\beta + \sqrt{\beta^2 - 4(\mu + \alpha(N_1 + N_2))}}{2} \tag{5.8}$$

In Fig. 5.7 (b), the bifurcation shows three distinct behaviors when the original curve (red one) splits: (I) Depicts the coexistence of two curves (yellow and blue curves), representing the white area around the green structure in both the experiment and simulation. (II) Represents the existence of only a green nematic state and the isotropic one (blue and black curves). (III) Indicates the complete NI transition (black curve). This result is crucial because it implies that the transition depends on concentration. Even when the temperature is close to the NI transition, phase separation allows for the coexistence of nematic and isotropic states.

Chapter 6

Conclusion

Non equilibrium systems usually exhibits coexistence between two or more stable states, multistability, also exhibit domains of patterns between them. The patterns can be controlled and characterized by imposing some characteristics length in the dynamical system. In this dissertation several phenomena involving pattern formation and coexistence between phases in the context of liquid crystals were studied experimental and theoretically. Three topics were studied, in which the topics studied were analyze the molecular order, the pattern formation on the respective system, and the coexistence of different spaces. The main results of this dissertation and future perspectives are summarized below.

6.1 Photoisomerization Process in Dye-Doped Liquid Crystals:

- Experimentally, structures resulting from photoisomerization were observed, with the main result being the emergence, stabilization and characterization of ring patterns.
- The transition is induced by the photoisomerization process, where dye dopant molecules undergo trans-cis transitions upon exposure to light. This transition leads to a random reorientation of liquid crystal molecules, causing the emergence of the isotropic phase, modulated by a characteristic wavelength of the system.
- The interaction between the dopant and the liquid crystal is modeled by a Swift-Hohenberg type model, derived from the adiabatic elimination on a coupled model, where the liquid crystal is described using the Landau-deGennes model and an injection-relaxation model for the cis-state concentration.
- The rings pattern at high light intensities collapses, showing the existence of more intricate patterns, and the behavior in this regime requires meticulous study (theoretically and experimentally).
- The dynamics of Dye-Doped Liquid Crystal Configurations (DDLCC) depend on the light absorbance curve. If the pump light wavelength is far from the absorbance peak,

the sample will not be affected. This property could be utilized to create pixels in digital displays, controlled by light instead of voltage.

6.2 Universal Description of Ring Patterns in Non-Linear Systems:

- Utilizing a Swift-Hohenberg prototype model, the existence of single-modal rings close to the Turing point was theoretically demonstrated. However, these rings are unstable due to higher modal interaction.
- The emergence of stable ring patterns is observed far from the Turing Instability, as modal analysis is not applicable in this regime. The main ingredients for the existence of stable ring patterns were characterized as bistability of states, a characteristic wavelength, and curvature effects.
- Structures generated when the system exhibits angular invariance demonstrate the existence of different mechanisms, termed "inside ringing" and "outside ringing."
- If the system's boundary conditions lack angular invariance (square boundaries as example), the structure will not form a ring pattern when the front reaches the boundaries but will remain stationary .
- Ring patterns with these characteristics can be controlled, enabling the manipulation of specific features, such as choosing the wavelength, by adjusting certain system parameters. This capability allows to the manufacturing of devices, as example, adaptive iris diaphragms.

6.3 Phase Separation in NLC Close to the NI Transition

- The emergence and characterization of coexistence between different nematic structures in an isotropic medium are observed. The characteristic length evolution follows the Lifshitz–Slyozov law.
- The evolution of structures is driven by non-homogeneous concentration locally in the sample, resulting in the coexistence of different stable states.
- Concentration inhomogeneities persist in the sample even after returning to the nematic phase, creating a memory effect. Upon heating, the sample returns to homogeneous concentration. This property could be employed for encryption, such as generating single-use passwords or securing information. The inhomogeneities also induce the propagation of a white front around the structures if the temperature is low enough.
- The critical temperature T_c for the nematic transition, locally change for the different concentration.

- The concentration of the liquid crystal can be explained by coupling a Landau-deGennes equation with a Cahn-Hilliard equation, yielding similar results.
- Dye-Doped Liquid Crystal Configurations (DDLCC) enable multi-phase separation in the sample, leading to the emergence of dopant concentration structures and liquid crystal concentration structures driven by phase separation.

Bibliography

[1] G. Nicolis and I. Prigogine. *Self-Organization in Nonequilibrium Systems: From Dissipative Structures to Order Through Fluctuations*. A Wiley-Interscience publication. Wiley, 1977.

[2] P. Glansdorff and I. Prigogine. *Thermodynamic Theory of Structure, Stability and Fluctuations*. Wiley-Interscience, 1971.

[3] P Manneville. Dissipative structures and weak turbulence.

[4] Pierre-Gilles De Gennes and Jacques Prost. *The physics of liquid crystals*. Number 83. Oxford university press, 1993.

[5] I.C. Khoo and B.E.A. Saleh. *Liquid Crystals*. Wiley Series in Pure and Applied Optics. Wiley, 2007.

[6] S. Chandrasekhar. *Liquid Crystals*. Cambridge University Press, 2 edition, 1992.

[7] P. Oswald and P. Pieranski. *Nematic and Cholesteric Liquid Crystals: Concepts and Physical Properties Illustrated by Experiments*. CRC Press, 1st edition, 2005.

[8] J. D. Murray. *Mathematical Biology I: An Introduction*. Springer, 2003.

[9] Rebecca B Hoyle. *Pattern formation: an introduction to methods*. Cambridge University Press, 2006.

[10] M. Cross and H. Greenside. *Pattern Formation and Dynamics in Nonequilibrium Systems*. Cambridge University Press, 2009.

[11] S.H. Strogatz. *Nonlinear Dynamics and Chaos: With Applications to Physics, Biology, Chemistry, and Engineering*. CRC Press, 2018.

[12] Kwang-Tao Chou, D Lee Dong-yeon, Jian-geng Chiou, Leticia Galera-Laporta, San Ly, Jordi Garcia-Ojalvo, and Gürol M Süel. A segmentation clock patterns cellular differentiation in a bacterial biofilm. *Cell*, 185(1):145–157, 2022.

[13] PH Coullet and Edward A Spiegel. Amplitude equations for systems with competing instabilities. *SIAM Journal on Applied Mathematics*, 43(4):776–821, 1983.

[14] A. Yariv and P. Yeh. *Optical waves in crystals: Propagation and control of laser radiation*. John Wiley & Sons, 2002.

[15] On vegetation clustering, localized bare soil spots and fairy circles. *Dissipative solitons: from optics to biology and medicine*, pages 1–22, 2008.

[16] I. Z. Kiss, Y. Zhai, and J. L. Hudson. Emergence of global wave synchronization in a forced oscillatory medium. *Physical Review Letters*, 88(23):238301, 2002.

[17] Camila Castillo-Pinto, Marcel G Clerc, and Gregorio González-Cortés. Extended stable equilibrium invaded by an unstable state. *Scientific Reports*, 9(1):15096, 2019.

[18] I Andrade-Silva, Umberto Bortolozzo, Camila Castillo-Pinto, MG Clerc, Gregorio González-Cortés, Stefania Residori, and Mario Wilson. Dissipative structures induced by photoisomerization in a dye-doped nematic liquid crystal layer. *Philosophical Transactions of the Royal Society A: Mathematical, Physical and Engineering Sciences*, 376(2135):20170382, 2018.

[19] J. B. Clarke, J. W. Hastie, L. H. E. Kihlborg, R. Metselaar, and M. M. Thackeray. Definitions of terms relating to phase transitions of the solid state (iupac recommendations 1994). *Pure and Applied Chemistry*, 66(3):577–594, 1994.

[20] G. H. Fredrickson and H. C. Andersen. Equilibrium theory of segmental polymers in a homopolymer matrix. *Macromolecules*, 15(2):262–270, 1982.

[21] C. Kittel. *Introduction to Solid State Physics*. John Wiley & Sons, 2005.

[22] P. Alberts, D. Bray, J. Lewis, and et al. *Molecular Biology of the Cell*. Garland Science, 2002.

[23] B. Alberts, A. Johnson, J. Lewis, and et al. *Essential Cell Biology*. Garland Science, 2014.

[24] P. N. Pusey and W. van Megen. Phase behaviour of concentrated suspensions of nearly hard colloidal spheres. *Nature*, 320(6060):340–342, 1986.

[25] Philip Hartman. *Ordinary Differential Equations*. John Wiley & Sons, 1964.

[26] Henri Poincaré. The principles of mathematical physics. *The Monist*, 15(1):1–24, 1905.

[27] John Guckenheimer and Philip Holmes. Nonlinear oscillations, dynamical systems, and bifurcations of vector fields. 1983.

[28] J. Swift and P. C. Hohenberg. Hydrodynamic fluctuations at the convective instability. *Phys. Rev. A*, 15:319–328, Jan 1977.

[29] K Staliunas and Victor J Sanchez-Morcillo. Dynamics of phase domains in the swift-hohenberg equation. *Physics Letters A*, 241(1-2):28–34, 1998.

[30] AM Turing. A reaction-diffusion model for development, the chemical basis of morphogenesis. *Phil Trans. Roy. Soc. of London, Series B*, pages 37–72.

[31] Raymond E Goldstein, Gemunu H Gunaratne, L Gil, and P Coullet. Hydrodynamic and interfacial patterns with broken space-time symmetry. *Physical Review A*, 43(12):6700, 1991.

[32] Hai Chi, Mykhailo Potomkin, Lei Zhang, Leonid Berlyand, and Igor S Aranson. Surface anchoring controls orientation of a microswimmer in nematic liquid crystal. *Communications Physics*, 3(1):162, 2020.

[33] Ana Mouquinho, Mara Saavedra, Alexandre Maiau, Krasimira Petrova, M. Teresa Barros, J. L. Figueirinhas, and João Sotomayor. Films Based on New Methacrylate Monomers: Synthesis, Characterisation and Electro-Optical Properties. *Molecular Crystals and Liquid Crystals*, 542(1):132/, June 2011.

[34] M. Elouali, C. Beyens, Fatima Elouali, Oleg Yaroshchuk, Abbar Boucif, and U. Maschke. Dispersions of diamond nanoparticles in nematic liquid crystal/polymer materials. *Molecular Crystals and Liquid Crystals - MOL CRYST LIQUID CRYST*, 545, 06 2011.

[35] Edina Rusen, Aurel Diacon, Raul-Augustin Mitran, Adrian Dinescu, Cristina Nistor, Raluca Șomoghi, Aurelian Cristian Boscornea, and Doina Mănăilă-Maximean. E7 nematic liquid crystal encapsulated in a polymeric photonic crystal. *European Polymer Journal*, 175:111374, 2022.

[36] I. Jánossy and A. D. Lloyd. Low-power optical reorientation in dyed nematics. *Molecular Crystals and Liquid Crystals*, 203(1):77–84, 1991.

[37] Marcel G Clerc, Gregorio González-Cortés, Paulina I Hidalgo, Lucciano A Letelier, Mauricio J Morel, and Jorge Vergara. Light-induced ring pattern in a dye-doped nematic liquid crystal. *Applied Sciences*, 11(11):5285, 2021.

[38] Dylan J Kahl, Kim M Hutchings, Erika Mathes Lisabeth, Andrew J Haak, Jeffrey R Leipprandt, Thomas Dexheimer, Dinesh Khanna, Pei-Suen Tsou, Phillip L Campbell, David A Fox, et al. 5-aryl-1, 3, 4-oxadiazol-2-ylthioalkanoic acids: a highly potent new class of inhibitors of rho/myocardin-related transcription factor (mrtf)/serum response factor (srf)-mediated gene transcription as potential antifibrotic agents for scleroderma. *Journal of medicinal chemistry*, 62(9):4350–4369, 2019.

[39] Iam Choon Khoo. Nonlinear optics of liquid crystalline materials. *Physics Reports*, 471(5-6):221–267, 2009.

[40] IC Khoo, S Slussarenko, BD Guenther, Min-Yi Shih, P Chen, and WV Wood. Optically induced space-charge fields, dc voltage, and extraordinarily large nonlinearity in dye-doped nematic liquid crystals. *Optics Letters*, 23(4):253–255, 1998.

[41] V Odent, MG Clerc, C Falcón, U Bortolozzo, E Louvergneaux, and S Residori. Photoisomerization fronts in dye-doped nematic liquid crystals. *Optics letters*, 39(7):1861–1864, 2014.

[42] A Petrossian and S Residori. Surfactant enhanced reorientation in dye-doped nematic liquid crystals. *Europhysics Letters*, 60(1):79, 2002.

[43] Francesco Simoni, Liana Lucchetti, Daniele Eugenio Lucchetta, and Oriano Francescangeli. On the origin of the huge nonlinear response of dye-doped liquid crystals. *Optics Express*, 9(2):85–90, 2001.

[44] Lars Onsager. Reciprocal relations in irreversible processes. i. *Phys. Rev.*, 37:405–426, Feb 1931.

[45] Herman Haken. Synergetics. *Physics Bulletin*, 28(9):412, 1977.

[46] Bei Wei, Jian Hou, Dejun Wu, Huiyu Wang, and Hao Liu. Pore scale simulation of surfactant flooding by lattice boltzmann method. 12 2018.

[47] John W Cahn and John E Hilliard. Free energy of a nonuniform system. i. interfacial free energy. *The Journal of Chemical Physics*, 28(2):258–267, 1958.

[48] I.M. Lifshitz and V.V. Slyozov. The kinetics of precipitation from supersaturated solid solutions. *Journal of Physics and Chemistry of Solids*, 19(1):35–50, 1961.

[49] Carl Wagner. Theorie der alterung von niederschlägen durch umlösen (ostwald-reifung). *Zeitschrift für Elektrochemie, Berichte der Bunsengesellschaft für physikalische Chemie*, 65(7-8):581–591, 1961.

[50] Björn König, Olivier JJ Ronsin, and Jens Harting. Two-dimensional cahn–hilliard simulations for coarsening kinetics of spinodal decomposition in binary mixtures. *Physical Chemistry Chemical Physics*, 23(43):24823–24833, 2021.

[51] PDE Solutions Inc. FlexPDE, 2022.

[52] G. Backstrom. *Simple Fields of Physics by Fe*. GB Publishing, 2012.

[53] W.H. Press. *Numerical Recipes 3rd Edition: The Art of Scientific Computing*. Numerical Recipes: The Art of Scientific Computing. Cambridge University Press, 2007.

[54] Claudio Canuto, M Yousuff Hussaini, Alfio Quarteroni, and Thomas A Zang. *Spectral methods: fundamentals in single domains*. Springer Science & Business Media, 2007.

[55] Luigi A Lugiato, Paul Mandel, and LM Narducci. Adiabatic elimination in nonlinear dynamical systems. *Physical Review A*, 29(3):1438, 1984.

[56] Marcel G Clerc, Artem Petrossian, and Stefania Residori. Bouncing localized structures in a liquid-crystal light-valve experiment. *Physical Review E*, 71(1):015205, 2005.

[57] Gregory Kozyreff and Mustapha Tlidi. Nonvariational real swift-hohenberg equation for biological, chemical, and optical systems. *Chaos: An Interdisciplinary Journal of Nonlinear Science*, 17(3), 2007.

[58] K. Staliunas and V.J. Sánchez-Morcillo. *Transverse Patterns in Nonlinear Optical Resonators*. Springer Tracts in Modern Physics. Springer Berlin Heidelberg, 2003.

[59] Gregory Kozyreff, S Jon Chapman, and Mustapha Tlidi. Interaction of two modulational instabilities in a semiconductor resonator. *Physical Review E*, 68(1):015201, 2003.

[60] Marcel G Clerc and Nicolas Verschueren. Quasiperiodicity route to spatiotemporal chaos in one-dimensional pattern-forming systems. *Physical Review E*, 88(5):052916, 2013.

[61] John Burke and Jonathan HP Dawes. Localized states in an extended swift–hohenberg equation. *SIAM Journal on Applied Dynamical Systems*, 11(1):261–284, 2012.

[62] N Verschueren, U Bortolozzo, MG Clerc, and S Residori. Spatiotemporal chaotic localized state in liquid crystal light valve experiments with optical feedback. *Physical review letters*, 110(10):104101, 2013.

[63] I. Newton. *Philosophiae naturalis principia mathematica*. Early English books online. Jussu Societas Regiæ ac typis Josephi Streater, prostant venales apud Sam. Smith, 1687.

[64] Len M Pismen. *Patterns and interfaces in dissipative dynamics*, volume 30. Springer, 2006.

[65] James D Murray. Mathematical biology ii: Spatial models and biomedical applications. *Monographs on Applied and Computational Mathematics*, 3, 1973.

[66] F Tito Arecchi, Stefano Boccaletti, and PierLuigi Ramazza. Pattern formation and competition in nonlinear optics. *Physics Reports*, 318(1-2):1–83, 1999.

[67] David Lloyd and Björn Sandstede. Localized radial solutions of the swift–hohenberg equation. *Nonlinearity*, 22(2):485, jan 2009.

[68] L. E. Blumenson. A derivation of n-dimensional spherical coordinates. *The American Mathematical Monthly*, 67(1):63–66, 1960.

[69] Linkam. LINK Software, 2021.

[70] Thorlabs. ThorCam Software, 2017.

[71] Martino Bardi, Michael G Crandall, Lawrence C Evans, Halil Mete Soner, Panagiotis E Souganidis, and Panagiotis E Souganidis. Front propagation: theory and applications. *Viscosity Solutions and Applications: Lectures given at the 2nd Session of the Centro Internazionale Matematico Estivo (CIME) held in Montecatini Terme, Italy, June 12–20, 1995*, pages 186–242, 1997.

[72] Simcha Lev-Yadun, Vladimír Račko, Monika Kardošová, and Jaroslav Ďurkovič. Indented growth-rings (hazel wood) deserve more attention. *Dendrochronologia*, 79:126073, 2023.

[73] Sergio Falcon and Angel Plaza. On the 3-dimensional k-fibonacci spirals. *Chaos, Solitons & Fractals*, 38(4):993–1003, 2008.

[74] Richard FitzHugh. Impulses and physiological states in theoretical models of nerve membrane. *Biophysical Journal*, 1(6):445–466, 1961.

[75] Isaac A Klein, Ann Boija, Lena K Afeyan, Susana Wilson Hawken, Mengyang Fan, Alessandra Dall'Agnese, Ozgur Oksuz, Jonathan E Henninger, Krishna Shrinivas, Benjamin R Sabari, et al. Partitioning of cancer therapeutics in nuclear condensates. *Science*, 368(6497):1386–1392, 2020.

[76] AJ Alvarez-Socorro, MG Clerc, and Mustapha Tlidi. Spontaneous motion of localized structures induced by parity symmetry breaking transition. *Chaos: An Interdisciplinary Journal of Nonlinear Science*, 28(5), 2018.

[77] SM Houghton and Edgar Knobloch. Swift-hohenberg equation with broken cubic-quintic nonlinearity. *Physical Review E*, 84(1):016204, 2011.

Annexes

Annex A: Light-Induced Ring Pattern in a Dye-Doped Nematic Liquid Crystal

This sections presents our results about Light-Induced ring patterns on a dye-doped liquid crystal cell.

Publication details:

- **Title**: Light-Induced Ring Pattern in a Dye-Doped Nematic Liquid Crystal
- **Authors**: M. Clerc, G. González, and P. Hidalgo, L. Letelier and M. Morel, and J. Vergara.
- **Corresponding author**: M. Clerc.
- **Journal**: Applied Sciences.
- **DOI**: https://doi.org/10.3390/app11115285

applied sciences

MDPI

Article

Light-Induced Ring Pattern in a Dye-Doped Nematic Liquid Crystal

Marcel G. Clerc [1,*], Gregorio González-Cortés [1], Paulina I. Hidalgo [2], Lucciano A. Letelier [1], Mauricio J. Morel [3] and Jorge Vergara [2]

[1] Departamento de Física and Millennium Institute for Research in Optics, Facultad de Ciencias Físicas y Matemáticas, Universidad de Chile, Casilla 487-3, Santiago 851, Chile; gregorio.gonzalez@ug.uchile.cl (G.G.-C.); lucciano.letelier@ug.uchile.cl (L.A.L.)
[2] Departamento de Química Orgánica, Facultad de Ciencias Químicas, Universidad de Concepción, Concepción 129, Chile; pauhidal@udec.cl (P.I.H.); jovergar@udec.cl (J.V.)
[3] Departamento de Química y Biología, Facultad de Ciencias Naturales, Universidad de Atacama, Ave. Copayapu, Copiapó 485, Chile; mauricio.morel@uda.cl
* Correspondence: marcel@dfi.uchile.cl; Tel.: +56-2-29784676

Abstract: The use of dye-doped liquid crystals allows the amplification of the coupling of light and liquid crystals. Light can induce the self-organization of the molecular order. The appearance of ring patterns has been observed, which has been associated with phase modulation. However, the morphology and dynamics of the ring patterns are not consistent with self-modulation. Based on an experimental setup with two parallel coherence beams orthogonal to a liquid crystal cell, one of which induces photo-isomerization and the other causes illumination, the formation of ring patterns is studied. To use these two coherent beams, we synthesize methylred methyl ester as a dye-dopant, which is photosensitive only to one of the light beams, and a commercial E7 liquid crystal as a matrix. Based on a mathematical model that accounts for the coupling between the concentration of the *cis*-state and the order parameter, we elucidate the emergence of the rings as forming patterns in an inhomogeneous medium. The bifurcation diagram is analytically characterized. The emergence, propagation of the rings, and the establishment of the ring patterns are in fair agreement with the experimental observations.

Keywords: photo-isomerization in liquid crystals; pattern formation; light-induced phenomena; azo-dye-dopant

Citation: Clerc, M.G.; González-Cortés, G.; Hidalgo, P.I.; Letelier, L.A.; Morel, M.J.; Vergara, J. Light-Induced Ring Pattern in a Dye-Doped Nematic Liquid Crystal. *Appl. Sci.* **2021**, *11*, 5285. https://doi.org/10.3390/app11115285

Academic Editor: Gaetano Assanto

Received: 14 May 2021
Accepted: 1 June 2021
Published: 7 June 2021

1. Introduction

The interaction between light and matter has played a fundamental role in the understanding and characterization from the early stages of research [1]. Likewise, the interaction between light and matter has also been the basis of the development of technological elements such as mirrors, lenses, telescopes, microscopes, lasers, and waveguides, among others. The development of more coherent and monochromatic light sources (lasers) accompanied by materials that present stronger nonlinear responses has allowed the creation of a great variety of devices [2–6]. Liquid crystals are one of the most versatile materials, because of their strong nonlinear response and reorientation capacity through the application of electromagnetic waves and electric and magnetic fields [7–11]. Liquid crystals are a state of matter in which the molecules have a preferential orientation and can have or not have a positional order; this organization is also known as soft matter [7–11]. Indeed, this state of matter shares features of solids and liquids. In particular, fluidity, molecular reorientation, and birefringence are characteristic properties of liquid crystals. One of the most studied types of liquid crystals used in technological applications are nematic liquid crystals (NLC). This state is composed of rod-like organic molecules [7–11]. Because of an intermolecular interaction, these molecules are arranged to have a similar molecular

orientation without positional order for specific temperature ranges. This results in a sharp anisotropy of all their physical properties, especially regarding elastic and optical characteristics. Likewise, the ability to reorient the molecular order has allowed the development of many applications, mainly liquid crystal displays (LCDs) and sensors [12]. The LCD is perhaps the best known liquid crystal application by the public today. However, in most of these applications, the control of molecular reorientation is done through electric fields. LCDs therefore require transparent or reflective electrodes, power sources, and other elements. Another manner of achieving molecular reorientation is to consider the application of electromagnetic waves through the liquid crystal sample [13–17]. However, this type of strategy requires the use of strong electromagnetic fields, which typically need a power on the order of 100 W/cm^2. For these powers, the nonlinear response of the medium is activated [11,18]. The previous scenario can change radically when one considers the dye-dopant inside the liquid crystal matrix. Indeed, when nematics are doped with azo-dyes, their nonlinear response to opto-electrical perturbations is increased by several orders of magnitude [11,18]. Indeed, azo-dyes mediate the origin of the coupling of the electromagnetic waves with the liquid crystal; when these molecules are irradiated, they present an isomeric transition. This phenomenon is known as the Jánossy effect [19]. This transition is characterized by the fact that the molecule changes from an elongated structure (*trans*-state) to one with a boomerang shape (*cis*-state) when the molecule absorbs a photon. Figure 1 illustrates the typical structure of these molecules.

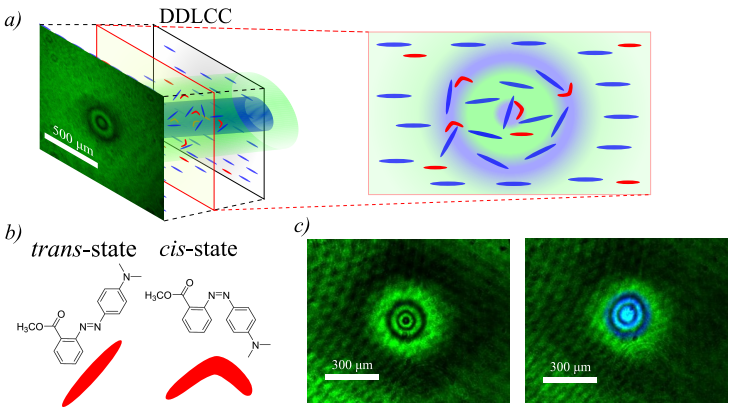

Figure 1. Ring patterns induced by light in a dye-doped liquid crystal cell (DDLCC). (**a**) Schematic representation of the experimental system. The blue and red bars, respectively, account for the molecules of the liquid crystal and azo-dye. The cell is illuminated by a blue and green beam. The snapshot accounts for the observed ring patterns. A transversal plane in the DDLCC is schematically represented. The areas under higher blue laser irradiation are more disordered, while the zones less illuminated preserve the nematic order. (**b**) Isomers of the molecule methyl red methyl ester. (**c**) Two snapshots showing the observed pattern (upper panel) and snapshot with the beam that induces photo-isomerization superimposed (bottom panel).

When a sufficiently intense light beam illuminates a thin film of dye-doped nematic liquid crystal, this can induce molecular disorder, generating a transition from a nematic phase to an isotropic one [20]. This type of transition is characterized by the emergence of a front between phases [20]. These fronts are characterized by being a circular spot that gathers in the center of the beam and spreads outwards and stops in the region where both states are energetically equivalent, Maxwell point. For intermediate light intensities, which do not induce isotropic liquid phase, the emergence of a pattern with a stripe shape has been reported [21,22]. In fact, these patterns correspond to regions that alternate higher and lower orientational molecular order. This phenomenon is understood as a result of the different scales in the transport processes of the concentration of the *cis* state and the orientational order of the liquid crystal. Thin films of liquid crystals without dye-

dopants subjected to strong electromagnetic fields in their cross section exhibit diffraction rings [14,23]. The above phenomenon is associated with phase modulation or autofocusing of light when is diffracted in the NLC. This medium is a good approximation to a Kerr medium [2–6,24], that is, the envelope of the light is under the effect of phase modulation, a cubic term for the envelope and diffraction. Hence, the conjunction of diffraction and phase modulation produces the emergence of diffraction rings. Note that the thickness of the observed rings decreases with the square distance from the center of the light beam. A similar phenomenon is observed in dye-doped liquid crystals when subjected to a coherent light with a moderate and low light intensity [25–27]. Because of the presence of dye-dopants, the nonlinear response can be achieved for light power of a few milliwatts [28]. The emergence of these rings has been associated with phase modulation. However, the morphology and dynamics of the ring patterns are not consistent with that expected for self-modulation rings observed for large intensities of light [14,23]. Furthermore, in this type of description, the dynamical behavior of the *cis* state concentration is passive. In other words, this concentration is enslaved to the system dynamics.

The article aims to elucidate and characterize the origin of the ring patterns observed when illuminating a dye-doped nematic liquid crystal cell with a light beam and planar anchoring. Based on an experimental setup with two parallel coherent beams, one of which induces photo-isomerization and the other the illumination, the formation of ring patterns is studied. Figure 1 illustrates the typical observed ring patterns. This type of setup allows us to separate the induction of the photo-isomerization and the observation of the self-organized patterns. To use these two coherent beams, we have synthesized methyl red methyl ester as dye-dopant, photo sensitive only to one of the light beams, and a commercial E7 (Instec Inc., Boulder, CO, USA) as a liquid crystal matrix. The methylred methyl ester was used as a dye-dopant (cf. Figure 1). Unlike methylred, the methylred methyl ester is more soluble and less viscous in E7 due to the absence of hydrogen bonds from the carboxylic acid group of the methylred. In addition, this structural modification prevents an intramolecular hydrogen bonding interaction with one of the nitrogens of the azo group, causing a faster *cis-trans* isomerization [29]. Theoretically, based on a mathematical model that accounts for the coupling between the concentration of the *cis* state and the order parameter, we elucidate the emergence of the rings as forming patterns in an inhomogeneous medium. The bifurcation diagram is analytically characterized. The emergence, propagation, and establishment of the ring patterns are in fair agreement with the experimental observations.

2. Experimental Observations of the Ring Patterns

The conventional phototropic transition detection is performed by sampling the excitation laser beam and extracting the reorientational order parameter with polarized optical microscopy [19–23,30]. The main inconvenience with those setups arises from the loss of information of the liquid crystal dynamics outside of the central Gaussian illuminated zone. Hence, the impossibility of differentiating between polarization changes in the light filtered out by the analyzer and the absorbed light by the sample. To overcome these difficulties, we developed an experimental setup with two parallel coherent beams applied to the dye-doped liquid crystal sample, which is only photo-sensitive to one beam (excitation beam) while the other is harmless (probing beam).

2.1. Experimental Setup

Figure 2 shows the experimental setup diagram. The dye-doped liquid crystal cell (DDLCC) undergoes a phototropic transition when it is irradiated by a light source in the absorption band of the guest dye [19,31]. We used a concentration of methylred methyl ester 1 wt% as azo-dye guest doping a commercially available E7 NLC (host). The chemical structure and isomers of methylred methyl ester are illustrated in Figure 1c. The absorption spectrum of the methylred methyl ester is depicted in Figure 2b (for details about the chemical synthesis and depuration of the azo-colorant, see Section 2.2).

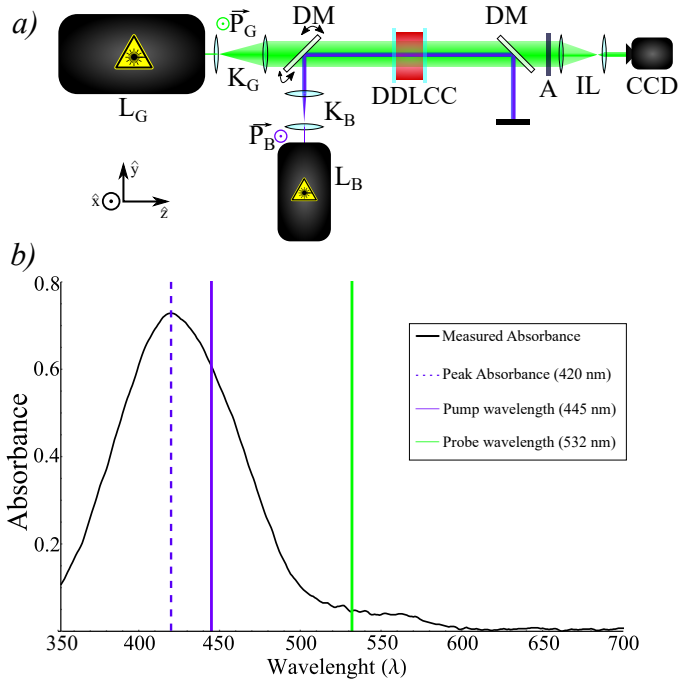

Figure 2. Experimental setup for the dye-doped nematic liquid crystal phototropic transition with a harmless external illumination. (**a**) A dye-doped liquid crystal cell (DDLCC) is irradiated by a 445 nm blue laser (excitation light beam) L_B and illuminated by a 532 nm green laser (probing light beam) L_G. Two pairs of lenses are placed in a Kepler telescope configuration K_B and K_G to expand the laser beam while preserving the collimation. $\vec{P}_B$ and $\vec{P}_G$ are the polarization of the laser sources. A long-wave pass dichroic mirror DM is used to set both excitation and probing on the same optical line. After the DDLCC, another long-wave pass dichroic mirror is used to filter out the excitation beam. An analyzer in a crossed configuration with respect to $\vec{P}_G$. A set of imaging optics IL consisting on a $\times 2$ Kepler telescope and a $\times 7$ zoom lens is used to enhance the image captured by the 1/2" CCD camera. (**b**) Absorption spectrum of methyl red methyl ester in dichloromethane 2.0×10^{-5} mol/L. The solid vertical lines account for the wavelength of the exciting and probing light, respectively. Vertical dashed lines account for the absorption maximum.

The mixture was injected into an antiparallel planarly aligned liquid crystal cell with a thickness of 25 µm (Instec Inc., Boulder, CO, USA). A 445 nm Cobolt 90 nW Polarized Laser was used as an exciting irradiation source to generate a phototropic transition. The polarization $\vec{P}_B$ was fixed, and the laser power was used as a tuning or bifurcation parameter. Note that the blue laser wavelength was close to the absorbance peak at 420 nm, enabling us to trigger the isomerization and increase the amount of *cis* methyl red methyl ester isomer. There was no relevant temperature change in the DDLCC. The experiment was conducted at room temperature, approximately 20 °C. This meant that only an increase of the *cis*-isomer concentration was responsible for a decrease of birefringence on the liquid crystal. A Kepler telescope K_B with a magnification of $\times 1/5$ was used to change the waist of the blue laser. The orientational molecular order in the dye-doped liquid crystal interacted with the blue light, making blue light sampling unsuitable for scanning the optical response of the liquid crystal sample.

To uncouple the excitation and probing fields, we provided illumination with a 532 nm Verdi V-2 polarized green laser as a probing light. Indeed, the absorbance at 532 nm is negligible for methyl red methyl ester, as seen in Figure 2. Both the green laser polarization $\vec{P}_G$ and its intensity were set fixed. A Kepler telescope with a magnification of $\times 2$ was used to expand the beam and obtain a more homogeneous illumination. A long-pass dichroic mirror DM (cutoff wavelength at 500 nm) was mounted in a pitch-yaw kinematic mount to

control the reflection angle and thus the position of the blue laser on the DDLCC. A second dichroic mirror was used to filter out the excitation light from the optical path to the 1/2″ CCD camera. To record the images, a set of illumination optics was used to enhance the image quality. A first pair of lenses in a Kepler telescope configuration with an optical zoom of $\times 2$ and a secondary zoom lens with a magnification of $\times 7$ was used. This system allowed s to achieve diffractionless recordings on the elements in the DDLCC plane, ensuring no diffractive rings on the images were recorded. Likewise, we displaced the liquid crystal cell parallel to the optical axis with respect to the dichroic mirrors, and no changes were observed in the ring patterns. This guaranteed that the observed phenomenon was not diffractive in nature. Figure 1b shows the probing illumination field in the upper panel, and the lower panel shows both the excitation and probing fields obtained by the CCD camera, respectively. The dynamical behavior of the order parameter could not be completely sampled only by measuring the excitation field. A set of imagining lenses was used to enhance the recorded images. In particular, we used a $\times 2$ magnification telescope coupled with a zoom lens and density filters. Notice that both excitation and probe illuminations were collimated when reaching the DDLCC. Thus, diffractive effects induced by changes in the position along the optical axis of the DDLCC were negligible. This meant that the position of the DDLCC was not a parameter of the experiment. The dynamics of the *cis* concentration and nematic order parameter did not depend on the cell position along the $\hat{z}$ axis, which was the axis of light propagation on the dye-doped liquid crystal cell.

2.2. Synthesis and Preparation of Dye-Dopant and Liquid Crystal Mixture

Dye-dopant: The methylred methyl ester was obtained from a Fischer–Spier esterification between methyl red (Sigma-Aldrich Inc., St. Louis, MO, USA) and methanol (Merck). The methanol was used as a reagent and solvent at reflux for 6 h with sulfuric acid (Merck) as a catalyst [32]. The final compound was characterized by Fourier Transform Infrared Spectroscopy, and the purity was confirmed by thin layer chromatography. The absorption spectrum of methyl red methyl ester was measured by employing a Spectroquant Pharo 300 spectrometer with a 1 cm optical path quartz cuvette in dichloromethane (Merck) solutions. The absorption spectrum is reported in Figure 2b).

Mixture preparation: The 1 wt% mixture was prepared by weighing each component and dissolving them separately into dichloromethane. The solutions were combined and homogenized by sonicating for 5 min. The solvent was removed by slow evaporation at room temperature.

2.3. Light-Induced Ring Patterns

When the dye-doped liquid crystal cell was illuminated with a probing light, the monitoring CCD camera showed a homogeneous dark greenish color throughout the cell, as illustrated in the snapshot of Figure 3b at t_0. When applying the blue light beam, we observed that the illuminated area immediately began to transmit more light. Figure 3a illustrates how the total transmitted intensity measured in the green channel of the CCD camera (ΔI_g) evolved over time with respect to the transmitted light without the blue light beam ($I_{g,0}$). The temporal evolution of the detected light intensity was characterized by growth and subsequent saturation. Figure 3a shows two regions in which the growth (region I) and saturation region (II) could be distinguished. In order to describe the growth and saturation process, we modeled it using the following expression: $\Delta I_g(t)/I_{g,0} = A(1 - e^{t/\tau})$, where $A = 2.79$ and $\tau = 55.71$ s. Namely, the establishment of the stationary ring pattern required a time period on the order of one minute.

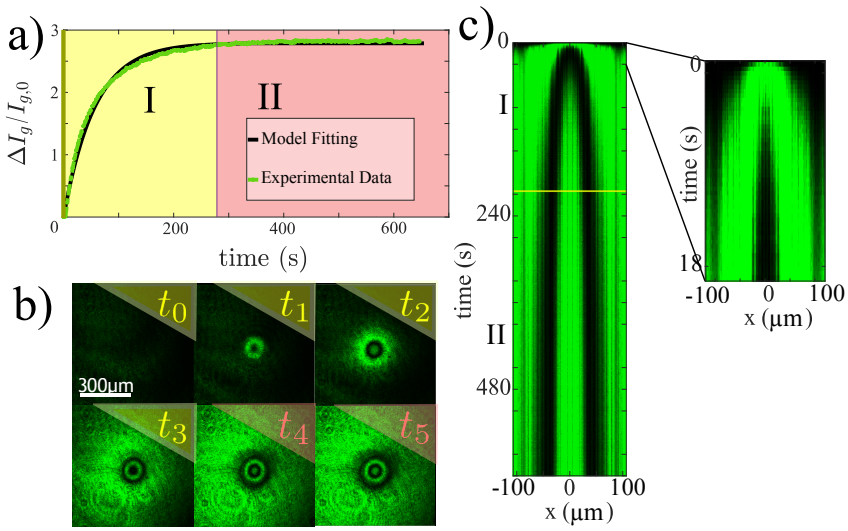

Figure 3. Experimental ring pattern emergence induced by a blue light (with a 445 nm wavelength) applied to a dye-doped liquid crystal cell, E7 NLC with azo-dye methyl red methyl ester at a concentration of 1 wt%. (**a**) Temporal evolution of transmitted total intensity, measured in the green channel of the CCD camera (ΔI_g) with respect to the transmitted light without the blue light beam ($I_{g,0}$). The points were obtained experimentally, and the continuous curve was acquired using the expression $\Delta I_g(t)/I_{g,0} = A(1 - e^{t/\tau})$, where $A = 2.79$ and $\tau = 55.71$ s. Painted areas I and II account for the growth and saturation regions, respectively. (**b**) Temporal sequence of snapshots in the ring pattern formation process ($t_0 = 0$ s, $t_1 = 1$ s, $t_2 = 5$ s, $t_3 = 84$ s, $t_4 = 360$ s, and $t_5 = 570$ s). (**c**) Spatiotemporal diagram evolution of a diameter cut section.

When the blue light was applied, a region of light green with a darker center emerged; as time elapsed, this dark spot became a propagative ring. Note that the lightened region continued to grow, becoming even larger than the waist of the blue laser. Figure 1b compares the light green region to the waist size of the blue laser. As time continued to elapse, the dark ring continued to move away from the center, and a new dark spot emerged in the center, which then became a new dark ring. Figure 3b summarizes the temporal sequence of snapshots in the ring pattern formation process. In order to determine the process of spot emergence and ring propagation, we consider the spatiotemporal evolution of a diameter cut section. Figure 3c illustrates the observed spatiotemporal diagram evolution. From this chart, we see how the dark rings emerge, spread, and stop.

When we applied low powers of the blue laser (few mW, cf. Figure 4), the system did not show the formation of ring patterns, and we only observed the emergence of a light green spot. As the power was increased, this light green spot increased in size. With powers close to 40 mW, we began to observe the emergence of a dark spot in the center of the illuminated region (see Figure 4). Physically, we interpreted this region as a region of greater orientational disorder due to the consideration of the dye-doped liquid crystal sample between crossed polarizers. When we further increased the power of the blue laser, we observed the emergence of the first ring. Figure 4 shows the observed equilibrium ring. As the power increased, the diameter of the equilibrium ring grew. For powers close to 70 mW, we observed the emergence of a ring with a dark spot in the center as a state of equilibrium. As the power of the blue laser continued to increase, we observed that the central dark spot grew, and at a higher power, it became unstable, generating a new ring. Figure 4 summarizes the equilibria found for different blue laser powers.

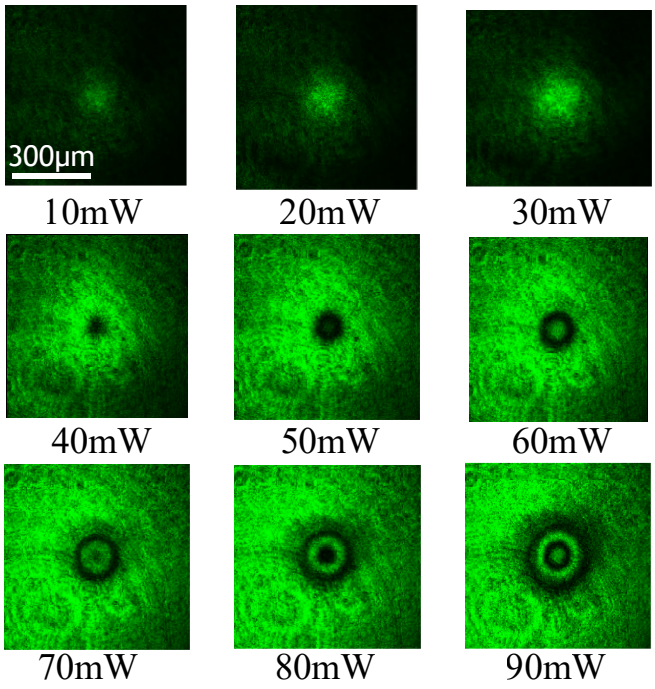

Figure 4. Equilibria ring patterns were experimentally observed for different powers of the blue light beam. After a long period of evolution, snapshots were observed for different powers, as denoted in the lower part of each snapshot.

3. Mathematical Modeling for Photo-Isomerization in Dye-Doped Liquid Crystals

Nematic liquid crystals are formed by rod-shaped molecules that—in a temperature range—can present an orientational rather than positional order. Then, the dynamics of the NLC can be described by a scalar order parameter $S(\vec{r};t)$ that accounts for the alignment of the molecules along a given direction [7–9], defined by

$$S(\vec{r};t) \equiv \frac{(3\langle\cos^2\theta\rangle - 1)}{2}, \tag{1}$$

where the brackets $\langle\cdot\rangle$ mean the spatial average in a microscopic element volume at position $\vec{r}$ and time t, and θ is the angle between the molecules and the local preferred direction [7–9]. Thus, S accounts for the dispersion of the molecules with respect to their average direction. The scalar order parameter for a perfectly aligned nematic phase is $S = 1$, and that for an isotropic phase is $S = 0$. Note that a negative and large S shows that the molecules are oriented, but the choice of the current orientation does not coincide with the molecular average orientation. Close to a phase transition, Landau conjectured that the free energy can be written as a polynomial expansion of the order parameter [33]. Based on this type of approach, in the Landau–de Gennes theory, the transition between a nematic and an isotropic liquid state in a thin film is described by the dimensionless equation [7]

$$\partial_t S(r_\perp, t) = -AS + BS^2 - S^3 + \nabla^2 S, \tag{2}$$

where $r_\perp$ accounts for the transversal coordinate of the liquid crystal layer and A is the bifurcation parameter, which is proportional to the difference between the current and critical temperature. Note that for large values of A, the isotropic state is favored in comparison to the nematic state. B is a parameter that characterizes the size of the region of coexistence between the nematic and isotropic liquid state. The third and fourth terms on the right-hand side account for the nonlinear response of the medium and the spatial coupling of the order parameter, respectively. This coupling is diffusive in nature. Namely,

the flow of the order parameter is proportional to its gradient. This model predicts that the nematic and the isotropic liquid transition is of a subcritical nature. On the other hand, the concentration of molecules in the *cis*-state $C(\vec{r},t)$ at position $\vec{r}$ in time t satisfies a relaxation and diffusion equation of the form [19]

$$\partial_t C = -\lambda[C - C_0(I)] + \delta\nabla^2 C, \tag{3}$$

where λ is the decay rate related to the transition from a *cis* to *trans* state by thermal relaxation. $C_0(I)$ is the equilibrium concentration of molecules in the *cis* state that is proportional to the total intensity of the incident light I. Indeed, $C_0(I) \equiv \gamma I/(1+\eta I)$, where γ and η are dimensional parameters [19]. δ is the diffusion coefficient of the concentration of the *c*is state. As a result of the propagation of light, the intensity of the light has the following form:

$$I = I_0 e^{-r_\perp^2/w^2}, \tag{4}$$

where w and I_0 are the light beam waist and the light intensity at the beam's center, respectively.

As we have mentioned, the incorporation of dye-dopants increases the nonlinear response of liquid crystals under the excitation of external fields [11,18–20,34]. Since the dye-dopant is not a liquid crystal and may even be immiscible, its excessive inclusion can prevent the mixture from being a liquid crystal; thus, a dye-dopant should be used in small amounts. We note that one of the reasons for considering methyl red methyl ester is that it is more miscible in E7 than other dopants; for example, methyl red. To describe the dynamics of the photo-isomerization process in the dye-doped nematic layer with planar anchoring, let us consider the concentration of molecules in the *cis*-state $C(\vec{r}_\perp,t)$ and the scalar order parameter $S(\vec{r}_\perp,t)$, which satisfy the dimensionless rate equations [21,22]

$$\begin{aligned} \partial_t C &= -\lambda[C - C_0(I) + \alpha S] + \delta\nabla^2 C + D\nabla^2 S, \\ \partial_t S &= -(A + \beta C)S + BS^2 - S^3 + \nabla^2 S + D\nabla^2 C. \end{aligned} \tag{5}$$

The α parameter accounts for the reduction of the *cis*-state concentration when the liquid crystal molecules are more aligned (larger S) because the dye-dopants tend to be oriented in the direction of the molecules (transition from *cis* to *trans*) [19]. Indeed, the liquid crystal matrix tends to make the dye-dopants orient and stretch in the direction of the molecular order. The parameter β stands for the entropic effect of the photo-isomerization process; that is, by increasing the concentration of the *cis* molecules, the disordered or non-oriented state is favored. Then, the linear term in S must decrease if the dye-dopant concentration increases. The parameter D accounts for the mutual transport process; namely, a gradient in the dopant concentration induces the propagation of the order parameter [35].

In the limit of the large-scale separation between the order parameter S and the concentration of the *cis*-state ($\lambda \gg 1$) and for small α and intensity I, the cis-state concentration satisfies

$$C = C_0(I) \approx \gamma I = \gamma I_0 e^{-r_\perp^2/w^2}. \tag{6}$$

Therefore, the cis-state concentration acquires a Gaussian profile. Using this expression in the equation of the order parameter, S satisfies the Landau–De-Gennes model for the nematic to isotropic transition induced by photo-isomerization [20]. Indeed, the bifurcation parameter $A(I) \equiv A + \beta\gamma I$ is controlled by the light intensity profile. When the sample is not illuminated, the system is in a NLC phase (S_+). When the sample is illuminated, the light can induce front propagation from the isotropic (S_{IS}) to the nematic phase [20].

3.1. Adiabatic Elimination and Effective Model

To determine the dynamics described by Equation (5), one can consider the adiabatic elimination of the *cis*-state concentration [36]. Indeed, by assuming that the temporal evolution of the *cis*-state concentration is rapid compared to the dynamics of the order

parameter—i.e., $\lambda \gg 1$—and by using Neumann series, one can approach, in a dominant order, the *cis* concentration by

$$C \simeq C_0(I) - \alpha S + \frac{D - \alpha\delta}{\lambda}\nabla^2 S. \tag{7}$$

Introducing this expression in the equation for the order parameter S, at a dominant order, we obtain

$$\begin{aligned} \partial_t S &= -[A + \beta C_0(I)]S + (B - \alpha\beta)S^2 - S^3 + (1 - D\alpha)\nabla^2 S \\ &+ \frac{D(D - \alpha\delta)}{\lambda}\nabla^4 S + \frac{\beta}{\lambda}(D - \delta\alpha)S\nabla^2 S + D\nabla^2 C_0(I). \end{aligned} \tag{8}$$

Renormalizing the space $\vec{r} = \vec{r}'[\lambda/D(\delta\alpha - D)]^{1/4}$, the effective model reads

$$\partial_t S = -\tilde{A}S + \tilde{B}S^2 - S^3 - \nu\nabla^2 S - \nabla^4 S + bS\nabla^2 S + \tilde{\eta}, \tag{9}$$

where

$$\tilde{A}(\vec{r}') \equiv A + \beta C_0(I(\vec{r}')), \tag{10}$$

$$\tilde{B} \equiv (B - \alpha\beta), \tag{11}$$

$$\nu \equiv D\alpha - 1\sqrt{\frac{\lambda}{D(\delta\alpha - D)}}, \tag{12}$$

$$b \equiv \frac{\beta(D - \delta\alpha)}{\sqrt{\lambda D(\delta\alpha - D)}}, \tag{13}$$

$$\tilde{\eta}(\vec{r}') \equiv D\sqrt{\frac{\lambda}{D(\delta\alpha - D)}}\nabla^2 C_0(I). \tag{14}$$

The model in Equation (9) corresponds to a non variational Swift–Hohenberg-type equation [37,38]. This model has been used to study patterns [39,40], localized, stationary [37,41], and propagative structures [42,43], and spatiotemporal chaotic extended [40] and localized structures [44]. These phenomena have been studied in different contexts ranging from physics and chemistry to biology. The physical origin of the formation of spatial structures is due to the anti-diffusion coefficient ($\nu > 0$), which represents the different scales of the transport processes of the *cis* order and state parameter, which introduces an intrinsic characteristic scale: the Turing mechanism [45]. Namely, by having two transport processes with different scales, the system cannot propagate the order parameter and the *cis*-state homogeneously; thus, it self-organizes, forming patterns.

3.2. Homogeneous Illumination and Bifurcation Diagram

Considering a spatially homogeneous illumination—that is, C_0 is a constant—the parameters that characterize the nematic and isotropic liquid transition are renormalized and independent of the space. The effective model has the form

$$\partial_t S = -\tilde{A}S + \tilde{B}S^2 - S^3 - \nu\nabla^2 S - \nabla^4 S + bS\nabla^2 S. \tag{15}$$

The homogeneous phases of this model have the form $S_0 = 0$ and

$$S_\pm = \frac{\tilde{B} \pm \sqrt{\tilde{B}^2 - 4\tilde{A}}}{2}, \tag{16}$$

where S_0 and $S_\pm$ account for the liquid isotropic and nematic phase. For high temperatures—i.e., a large $\tilde{A}$—it is expected that the only stable state is the isotropic liquid phase S_0. When decreasing $\tilde{A}$, the system presents a coexistence between the isotropic and nematic phase for $\tilde{A} = A_{sn} \equiv \tilde{B}^2/4$. This bifurcation occurs due to the emergence of two new equilibria:

the saddle-node bifurcation causes the emergence of a stable nematic state (S_+) and an unstable state (S_-). Figure 5 shows the bifurcation diagram of the model in Equation (15). As $\tilde{A}$ continues to decrease, the isotropic liquid state S_0 is as favorable as the nematic phase S_+ for $A = A_M \equiv 2\tilde{B}^2/9$—the Maxwell point [46]. Then, a flat wall between these two phase states at this critical point is characterized by being motionless. When further decreasing $\tilde{A}$, the isotropic liquid phase presents a spatial instability. We can study this instability by linearizing Equation (15) around the isotropic liquid state $S_0 = 0$, and considering the ansatz $S(\vec{r}, t) = S' e^{i\vec{k}\vec{r}+i\sigma t}$, we obtain the growth rate equation:

$$\sigma = -\tilde{A} + \nu\vec{k}^2 - \vec{k}^4, \tag{17}$$

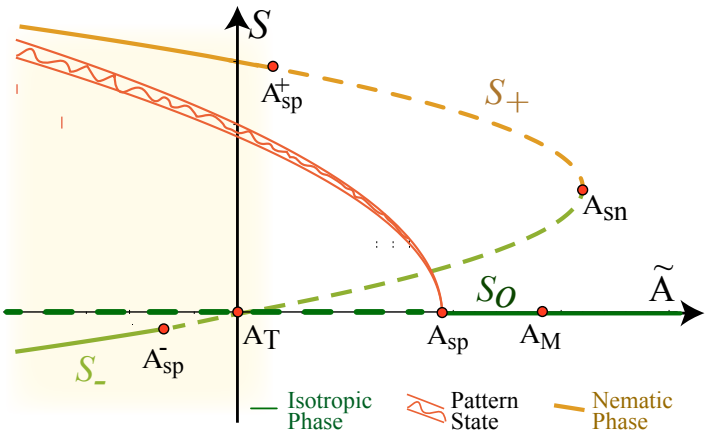

Figure 5. Schematic representation of the bifurcation diagram of the effective model in Equation (15) with constant coefficients. The order parameter S as a function of the bifurcation parameter $\tilde{A}$. S_0, S_+, and S_- account for the isotropic liquid and nematic phases, respectively. The continuous and dashed lines account for stable and unstable states respectively. A_{sn}, A_M, and A_T are the critical points that account for the emergence of the nematic phase; both phases are equally favored, with a transcritical bifurcation of the isotropic liquid phase. A_{sp}, A^+_{sp}, and A^-_{sp} account for the spatial instabilities of the homogeneous phases. The painted area shows the region of coexistence between the periodic state and the homogeneous state. The decorated curve explains the amplitude of the patterns.

The instability condition is $d\sigma(k_c)/dk = 0$ and $\sigma(k_c) = 0$. The first condition determines the critical length $k_c = \sqrt{\vec{k}^2} \equiv \sqrt{\nu/2}$, and the second defines the critical relation of the parameters for the spatial instability, which has the form $\tilde{A} = A_{sp} \equiv \nu^2/4$. Weakly nonlinear analysis shows that this instability is of a supercritical nature for a small $\tilde{B}$. Thus, despite the fact that the linear term is positive, $0 < \tilde{A} < A_{sp}$, the isotropic liquid state is unstable. For $\tilde{A} = A_T \equiv 0$, the system presents a transcritical bifurcation between unstable states.

To study the stability of the nematic phase, we use a similar strategy as in the study of the spatial stability of the isotropic liquid phase. Let us consider the linear perturbation $S = S_\pm + \chi$, where χ is a small variable that satisfies the equation

$$\partial_t\chi = (-\tilde{A} + 2\tilde{B} - 3S_\pm^2)\chi - (\nu + bS_\pm)\nabla^2\chi - \nabla^4\chi. \tag{18}$$

Introducing the ansatz $\chi(\vec{r}, t) = \chi' e^{i\vec{k}\vec{r}+i\sigma t}$ in the above equation, we obtain

$$\sigma = -\tilde{A} + 2\tilde{B} - 3S_\pm^2 + (\nu + bS_\pm)\vec{k}^2 - \vec{k}^4. \tag{19}$$

Imposing the spatial instability conditions, we obtain $k_c = \sqrt{\vec{k}^2} = \sqrt{(\nu + bS_\pm)/2}$ and

$$2\tilde{A} + \tilde{B}S_\pm = -\frac{(\nu + bS_\pm)^2}{4}. \tag{20}$$

From this expression, we obtain two critical conditions for spatial instability A_{sp}^{+} and A_{sp}^{-} corresponding to each of the nematic states (see Figure 5). Therefore, the effective model predicts a region of coexistence between a pattern state and a nematic phase. Figure 5 shows this region of coexistence with a painted area.

3.3. Light-Induced Ring Pattern

Figure 5 summarizes the different behaviors presented by the model in Equation (15). From this chart, we conclude that the system has a coexistence region between the nematic state and the pattern. Note that this pattern alternates between areas of higher and lower orientation order [21,22]. This affects the sample's refractive index; therefore, if a light beam passes through the sample in a patterned state, one expects to observe interference fringes. As the light intensity increases, the bifurcation parameter $\tilde{A}$ grows. Then, if one considers a light intensity with a Gaussian profile, the parameter $\tilde{A}(I)$ is characterized by being inhomogeneous, with a bell-like shape. Thus, if the cell is in a nematic phase when the sample is illuminated, the central part of the light beam can induce the cell to leave the coexistence region, and only the pattern will be stable. For this type of region, we would expect to find that the illuminated area shows patterns because the central area of the light beam is circular, and for a small-waist beam, one would expect to see ring-like patterns. Figure 6 shows the typical equilibrium ring pattern observed numerically for the model Equation (9). All numerical simulations presented are obtained by considering finite differences coded with the Runge–Kutta order-4 algorithm.

If the system is not illuminated, $I_0 = 0$, the uniform nematic phase is the equilibrium of the system. By illuminating the system with a low intensity, we found numerically that there was a slight decrease in the reorientation order and an increase in the *cis* concentration in the central part of the Gaussian (cf. Figure 7). As the intensity I_0 increased, the size of the central spot showed greater orientation disorder; that is, the order parameter S decreased in the central zone as I_0 increased. Note that the spot of the orientational disorder was smaller than the waist of the Gaussian forcing. As I_0 increased in the central zone, the parameter of order S approached zero (isotropic liquid). When it hit zero, it generated a new dynamical behavior; the central point expanded, creating a ring. The origin of the clearing out of the central zone was due to the fact that the order parameter S became negative. This could be interpreted as two ordered regions separated by a circular interface of the disordered state. A dark ring in Figure 7 represents this region. As I_0 increased further, the ring continued to expand. By further increasing the intensity of the Gaussian forcing, we observed the emergence of a new central spot surrounded by a ring. Note that for this parameter region, when beginning with a uniform nematic state and applying Gaussian forcing, a central spot of disorder state initially emerged that expanded, forming a ring that continued to propagate; later, another central spot of disorder state emerged, and finally the ring pattern stopped and remained in a stationary state. Experimentally, we observed a similar behavior to that observed numerically (see Figure 3). As the intensity of the Gaussian forcing I_0 increased further, new central spots emerged, which became new rings of disordered states (see Figure 7). The waist of the light beam limits the above process. This process is similar to the experimental process (see Figure 3).

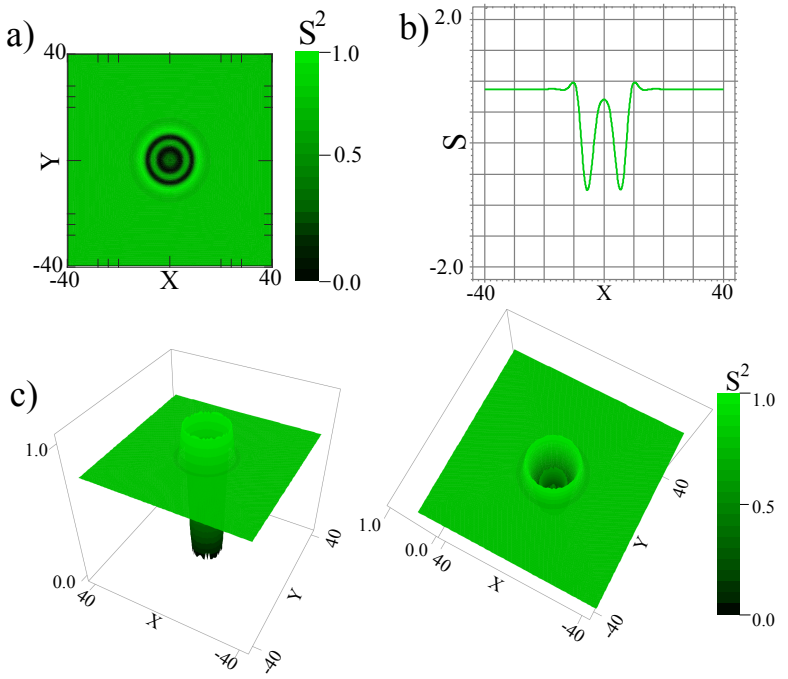

Figure 6. Numerical stationary ring pattern in a dye-doped nematic liquid crystal using the effective model in Equation (9) for $\tilde{A} = -0.5$, $\tilde{B} = 0.3$, $\nu = 1.05$, $b = 0.1$, $I_0 = 1.45$, and $w = 4$. (**a**) Contour plot of the squared order parameter S. (**b**) Profile of the cut of the order parameter S in the diameter of the ring pattern. (**c**) Surface plot of the squared order parameter S.

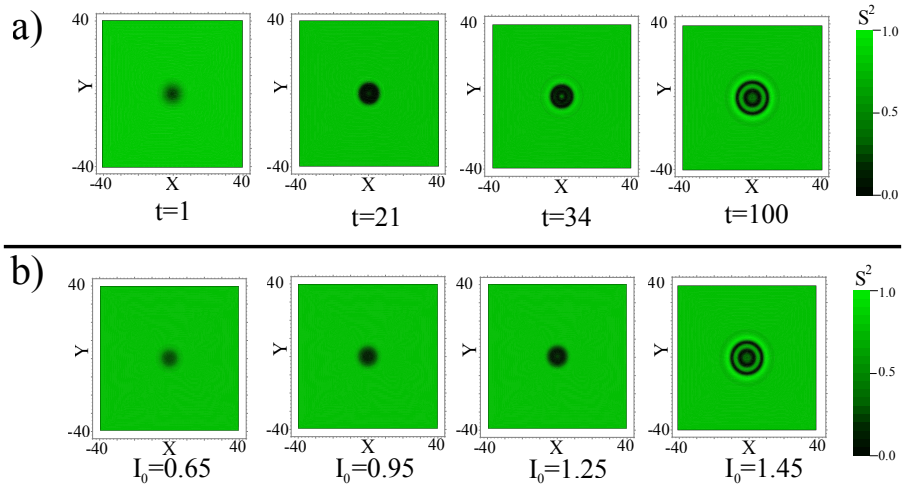

Figure 7. Numerical light-induced ring pattern in a dye-doped nematic liquid crystal using the model in Equation (9). (**a**) Temporal evolution of ring pattern using the effective model in Equation (9) for $\tilde{A} = -0.5$, $\tilde{B} = 0.3$, $\nu = 1.05$, $b = 0.1$, $I_0 = 1.45$, and $w = 4$. (**b**) Equilibrium of ring patterns numerically obtained for a different forcing strength I_0, and the other parameters are $\tilde{A} = -0.5$, $\tilde{B} = 0.3$, $\nu = 1.05$, $b = 0.1$, and $w = 4$.

In brief, the effective model in Equation (9) described the dynamics of the light-induced ring pattern in a dye-doped nematic liquid crystal well in qualitative terms.

4. Discussion

The emergence of ring patterns from an illuminated dye-doped nematic liquid crystal cell was initially attributed to the phase modulation of the diffractive light [27]. The light diffraction process is mathematically described by the nonlinear Schrödinger equation, which corresponds to the paraxial equation with a nonlinear correction associated with phase modulation. A local disturbance of the homogeneous state is characterized by the emergence of propagative rings towards the outside of the disturbance; these propagative rings are concentric with different thicknesses and decay with the square of the distance. In turn, the outer ring generates the emergence of outer rings with an increasingly smaller thickness. This type of pattern is similar to those reported for liquid crystal samples subjected to intense light rays [23]. The morphology of the ring pattern and the exhibited dynamics are different from those observed experimentally in the dye-doped nematic liquid crystal sample (see Figures 3 and 4).

The patterns found may allow manipulable interferometric patterns for light rays outside the absorption range of the dye-dopant. To illustrate the manipulability of the ring patterns, we adjusted the pitch and yaw of the dichroic mirror. Figure 8 schematizes the modification of the dichroic mirror, the effect on the light beam, and the observed ring patterns. Then, the light beam inside the doped liquid crystal sample could be shifted. Experimentally, we observed from the ring pattern in equilibrium that it moved almost rigidly. Figure 8b shows the light path scheme used and the ring patterns observed at the points marked on the path by discs. Likewise, it is important to note that the previous results showed that an interference mechanism does not cause the observed ring patterns. Note that the ring patterns caused by phase modulation were deformed with the angle of incidence [14], which is different from the observations in our setup (see Figure 8).

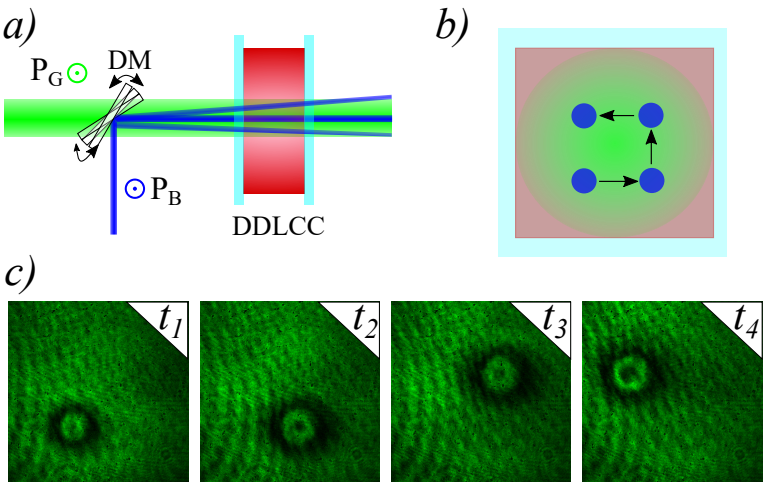

Figure 8. Manipulable ring patterns induced by illumination on a dye-doped liquid crystal sample. (**a**) Schematic representation of the mechanism for applying the light beam to the dye-doped liquid crystal sample. (**b**) Schematic representation of the path made by the light beam by adjusting the pitch and yaw of the dichroic mirror. (**c**) Snapshots of ring patterns observed at different times ($t_1 < t_2 < t_3 < t_4$).

5. Conclusions

Experimentally and theoretically, we have elucidated and characterized the origin of the ring patterns observed in a dye-doped nematic liquid crystal cell with planar anchoring under a light beam in the absorption band of the dye-dopant. To shed light onto the effect of the coherent excitation beam, we designed an experimental setup that considered two parallel beams—exciting and probing light—in which the probing light was monitored.

Based on a mathematical model that accounted for the coupling between the concentration of the *cis*-state and the orientational order parameter, we established the emergence of the rings as forming patterns in an inhomogeneous medium. Namely, the origin of the formation of pattern rings is due to the different scales and transport mechanisms of the concentration of the *cis*-state and the orientational order parameter. The formation of spatial structures induced by light can open up new applications such as the harnessing of diffraction gratings, masks, and irises. Work in this direction is in progress.

Author Contributions: Conceptualization, M.G.C. and G.G.-C.; methodology, G.G.-C., P.I.H., M.J.M. and J.V.; numerical analysis, L.A.L.; validation, G.G.-C. and L.A.L.; formal analysis, M.G.C. and L.A.L.; writing—original draft preparation, M.G.C.; improvement and verification of the manuscript, all authors. All authors have read and agreed to the published version of the manuscript.

Funding: This research was funded by FONDECYT grant number 1210353, the National Agency for Research and Development (ANID) Scholarship Program Becas Doctorado Nacional 2017211716, and ANID–Millennium Science Initiative Program-ICN17_012.

Institutional Review Board Statement: Not applicable.

Informed Consent Statement: Not applicable.

Acknowledgments: The authors acknowledge the fruitful discussions with Raouf Barboza.

Conflicts of Interest: The authors declare no conflict of interest.

References

1. Newton, I. *Opticks, or, a Treatise of the Reflections, Refractions, Inflections & Colours of Light*; Sam. Smith and Benj. Walford, Printers to the Royal Society: London, UK, 1704.
2. Boyd, R.W. *Nonlinear Optics*; Academic Press: San Diego, CA, USA, 2003.
3. Shen, Y.R. *The Principles of Nonlinear Optics*; Wiley-Interscience: New York, NY, USA, 1984.
4. Mills, D.L. *Nonlinear Optics: Basic Concepts*; Springer Science & Business Media: Berlin/Heidelberg, Germany, 2012.
5. New, G. *Introduction to Nonlinear Optics*; Cambridge University Press: Cambridge, UK, 2011.
6. Lugiato, L.; Prati, F.; Brambilla, M. *Nonlinear Optical Systems*; Cambridge University Press: Cambridge, UK, 2015.
7. De Gennes, P.G.; Prost, J. *The Physics of Liquid Crystals*, 2nd ed.; Oxford Science Publications, Clarendon Press: Oxford, UK, 1993.
8. Chandrasekhar, S. *Liquid Crystal*; Cambridge University Press: New York, NY, USA , 1992.
9. Oswald, P.; Pieranski, P. *Nematic and Cholesteric Liquid Crystals*; CRC Press: Boca Raton, FL, USA, 2005.
10. Vertogen, G.; de Jeu, W.H. *Thermotropic Liquid Crystals, Fundamentals*; Springer Science & Business Media: Berlin/Heidelberg, Germany, 2012.
11. Khoo, I.C. *Liquid Crystals*; John Wiley & Sons: Hoboken, NJ, USA, 2007.
12. Takatoh, K.; Sakamoto, M.; Hasegawa, R.; Koden, M.; Itoh, N.; Hasegawa, M. *Alignment Technology and Applications of Liquid Crystal Devices*; CRC Press: Abingdon, UK, 2005.
13. Zel'Dovich, B.Y.; Pilipetskii, N.F.; Sukhov, A.V.; Tabiryan, N.V. Giant Optical Nonlinearity in the Mesophase of a Nematic Liquid Crystal. *JETP Lett.* **1980**, *31*, 263–267.
14. Zolot'ko, A.S.; Kitaeva, V.F.; Sobolev, N.K.N.; Chillag, L. The effect of an optical field on the nematic phase of the liquid crystal OCBP. *JETP Lett.* **1980**, *32*, 158–162.
15. Zolot'ko, A.S.; Kitaeva, V.F.; Sobolev, N.N.; Sukhorukov, A.P. Self-focusing of laser radiation in the course of the Fréedericksz transition in the nematic phase of a liquid crystal. *Zh. Eksp. Teor. Fiz.* **1981**, *81*, 933–941.
16. Durbin, S.D.; Arakelian, S.M.; Shen, Y.R. Optical-field-induced birefringence and Freedericksz transition in a nematic liquid crystal. *Phys. Rev. Lett.* **1981**, *47*, 1411–1414. [CrossRef]
17. Frisken, B.J.; Palffy-Muhoray, P. Electric-field-induced twist and bend Freedericksz transitions in nematic liquid crystals. *Phys. Rev. A* **1989**, *39*, 1513–1518. [CrossRef]
18. Khoo, I.C. Nonlinear optics of liquid crystalline materials. *Phys. Rep.* **2009**, *471*, 221–267. [CrossRef]
19. Jánossy, I.; Szabados, L. Photoisomerization of azo-dyes in nematic liquid crystals. *J. Nonlinear Opt. Phys.* **1998**, *7*, 539–551. [CrossRef]
20. Odent, V.; Clerc, M.G.; Falcón, C.; Bortolozzo, U.; Louvergneaux, E.; Residori, S. Photo-isomerization fronts in dye-doped nematic liquid crystals. *Opt. Lett.* **2014**, *39*, 1861–1864. [CrossRef]
21. Andrade-Silva, I.; Bortolozzo, U.; Clerc, M.G.; González-Cortés, G.; Residori, S.; Wilson, M. Spontaneous light-induced Turing patterns in a dye-doped twisted nematic layer. *Sci. Rep.* **2018**, *8*, 1–8. [CrossRef]
22. Andrade-Silva, I.; Bortolozzo, U.; Castillo-Pinto, C.; Clerc, M.G.; González-Cortés, G.; Residori, S.; Wilson, M. Dissipative structures induced by photoisomerization in a dye-doped nematic liquid crystal layer. *Phil. Trans. R. Soc. A* **2018**, *376*, 20170382. [CrossRef]

23. Durbin, S.D.; Arakelian, S.M.; Shen, Y.R. Laser-induced diffraction rings from a nematic-liquid-crystal film. *Opt. Lett.* **1981**, *6*, 411–413. [CrossRef]
24. Assanto, G. *Nematicons: Spatial Optical Solitons in Nematic Liquid Crystals*; John Wiley & Sons: Hoboken, NJ, USA, 2012.
25. Barnik, M.I.; Zolot'ko, A.S.; Kitaeva, V.F. Interaction of light with a dye-doped nematic liquid crystal. *J. Exp. Theor. Phys.* **1997**, *84*, 1122–1130. [CrossRef]
26. Deng, L.; He, K.; Su, W.; Sun, H.; Wang, R.; Zhang, H.; Liu, H.K. Optical limiting performances of the methyl-red-dye-doped nematic liquid crystal films. *Mater. Devices Syst. Disp. Lighting* **2002**, *4918*, 79–89.
27. Li, H.; Wang, J.; Wang, C.; Zeng, P.; Cai, P.; Pan, Y.; Yang, Y. Off-resonant nonlinear optical refraction properties of azo dye doped nematic liquid crystals. *Opt. Mater. Express* **2016**, *6*, 459–465. [CrossRef]
28. Serak, S.V.; Tabiryan, N.V.; Assanto, G. Nematicons in azobenzene liquid crystals. *Mol. Cryst. Liq. Cryst.* **2012**, *559*, 202–213. [CrossRef]
29. Park, H.S.; Oh, K.S.; Kim, K.S.; Chang, T.; Spiegel, D.R. Change of internal hydrogen bonding of methyl red upon photoisomerization monitored by Forced Rayleigh Scattering. *J. Phys. Chem. B* **1999**, *103*, 2355–2360. [CrossRef]
30. Castillo-Pinto, C.; Clerc, M.G.; González-Cortés, G. Extended stable equilibrium invaded by an unstable state. *Sci. Rep.* **2019**, *9*, 1–8. [CrossRef] [PubMed]
31. Kosa, T.; Sukhomlinova, L; Su, L.; Taheri, B.; White, T.J.; Bunning, T.J. Light-induced liquid crystallinity. *Nature* **2012**, *485*, 347–349. [CrossRef]
32. Kahl, D.J.; Hutchings, K.M.; Lisabeth, E.M.; Haak, A.J.; Leipprandt, J.R.; Dexheimer, T.; Khanna, D.; Tsou, P.S.; Campbell, P.L.; Fox, D.A.; et al. 5-Aryl-1,3,4-oxadiazol-2-ylthioalkanoic Acids: A Highly Potent New Class of Inhibitors of Rho/Myocardin-Related Transcription Factor (MRTF)/Serum Response Factor (SRF)-Mediated Gene Transcription as Potential Antifibrotic Agents for Scleroderma. *J. Med. Chem.* **2019**, *62*, 4350–4369. [CrossRef]
33. Landau, L.D.; Lifshitz, E.M. *Statistical Physics (Course of Theoretical Physics, Volume 5)*; Pergamon Press: New York, NY, USA, 1993.
34. Sasaki, T.; Ikeda, T. Photochemical switching of polarization in ferroelectric liquid crystals: Effect of structure of host FLCs. *Ferroelectrics* **1993**, *149*, 343–351. [CrossRef]
35. Bechhoefer, J.; Simon, A.J.; Libchaber, A.; Oswald, P. Destabilization of a flat nematic-isotropic interface. *Phys. Rev. A* **1989**, *40*, 2042–2056. [CrossRef] [PubMed]
36. Haken, H. *Synergetics: Introduction and Advanced Topics*; Springer: Berlin/Heidelberg, Germany, 1977.
37. Clerc, M.G.; Petrossian, A.; Residori, S. Bouncing localized structures in a liquid-crystal light-valve experiment. *Phys. Rev. E* **2005**, *71*, 015205. [CrossRef]
38. Kozyreff, G.; Tlidi, M. Nonvariational real Swift-Hohenberg equation for biological, chemical, and optical systems. *Chaos* **2007**, *17*, 037103. [CrossRef] [PubMed]
39. Kozyreff, G.; Chapman, S.J.; Tlidi, M. Interaction of two modulational instabilities in a semiconductor resonator. *Phys. Rev. E* **2003**, *68*, 015201. [CrossRef] [PubMed]
40. Clerc, M.G.; Verschueren, N. Quasiperiodicity route to spatiotemporal chaos in one-dimensional pattern-forming systems. *Phys. Rev. E* **2013**, *88*, 052916. [CrossRef]
41. Burke, J.; Dawes, J.H. Localized states in an extended Swift?Hohenberg equation. *SIAM J. Appl. Dyn. Syst.* **2012**, *11*, 261–284. [CrossRef]
42. Alvarez-Socorro, A.J.; Clerc, M.G.; Tlidi, M. Spontaneous motion of localized structures induced by parity symmetry breaking transition. *Chaos* **2018**, *28*, 053119. [CrossRef]
43. Houghton, S.M.; Knobloch, E. Swift-Hohenberg equation with broken cubic-quintic nonlinearity. *Phys. Rev. E* **2011**, *84*, 016204. [CrossRef]
44. Verschueren, N.; Bortolozzo, U.; Clerc, M.G.; Residori, S. Spatiotemporal chaotic localized state in liquid crystal light valve experiments with optical feedback. *Phys. Rev. Lett.* **2013**, *110*, 104101. [CrossRef]
45. Turing, A.M. The chemical basis of morphogenesis. *Philos. Trans. R. Soc. B* **1952**, *237*, 37–72.
46. Goldstein, R.E.; Gunaratne, G.H.; Gil, L.; Coullet, P. Hydrodynamic and interfacial patterns with broken space-time symmetry. *Phys. Rev. A* **1991**, *43*, 6700–6721. [CrossRef] [PubMed]

Annex B: Concentric ring patterns beyond Turing instability

This sections presents our results about theoretical description of the main ingredients in ring patterns formation.
Publication details:

- **Title**: Concentric ring patterns beyond Turing instability
- **Authors**: M. Clerc, S. Echeverria, and L. Letelier.
- **Corresponding author**: L. Letelier.
- **Journal**: Physical Review Research.
- **DOI**: https://doi.org/10.1103/PhysRevResearch.5.L012007

Letter

Concentric ring patterns beyond Turing instability

M. G. Clerc, S. Echeverria-Alar, L. A. Letelier, and C. Núñez-Barra

Departamento de Física and Millennium Institute for Research in Optics, Facultad de Ciencias Físicas y Matemáticas, Universidad de Chile, Casilla 487-3, Santiago, Chile

(Received 4 November 2022; accepted 11 January 2023; published 18 January 2023)

Various out-of-equilibrium physical systems exhibit concentric ring patterns. However, these patterns are expected to be unstable due to the interaction of spatial modes. Here, we show that concentric ring patterns are stable beyond Turing instability. Based on a prototype pattern forming model, we show that these solutions are stable and identify the main ingredients for their stability: curvature, characteristic wavelength, and bistability. We further characterize the propagation of stable concentric ring patterns. Experimentally, we observe stable concentric ring patterns in an illuminated dye-doped liquid crystal cell with sufficiently high intensity. The formation of the concentric rings is in agreement with our predicted theoretical findings.

DOI: 10.1103/PhysRevResearch.5.L012007

Physical systems, in thermodynamic equilibrium, are characterized by presenting homogeneous equilibria that are invariant by spatial and temporal translation. Nonequilibrium processes often lead to the formation of dissipative structures in nature [1–4]. These processes are characterized by permanently injecting and dissipating energy, momenta, and particles. When the injection of energy is small compared to the dissipation, equilibria are usually characterized by being uniform and stationary, similar to those observed in thermodynamic equilibrium. From a dynamical system point of view, these equilibria correspond to attractors. Increasing the energy injection, the homogeneous states can become unstable and develop a pattern formation through a spatial symmetry-breaking instability [1–6]. The formation of patterns such as mountains, dunes, plants, clouds, snowflakes, stalactites, and skin of mammalians, insects, fish, and seashells has drawn attention since the beginning of time [3–7]. Also, spatiotemporal effects in patterns have motivated theoretical and experimental studies in nonequilibrium physics [8–11]. The wavelength of the pattern is usually determined by two mechanisms: (i) external, such as the geometric properties of the system under study (width, thickness, etc.) [2–6], or (ii) internal, such as different coupling properties (transport, diffusion, diffraction, etc.) [2–6,12]. This last mechanism, of an intrinsic length, was proposed by Turing [12], and it has been a relevant topic of study in the nonlinear optics community [6,13–17].

At the onset of spatial instability, a general strategy to describe the dynamics of the pattern is achieved through an amplitude equation approach [3,4,6,18], where the amplitudes account for the critical modes that become unstable. As a result of the nonlinear terms, the linearly unstable critical modes become saturated. This balance can give rise to stripe, hexagon, square, superlattice, labyrinthine, or quasicrystal patterns near the instability [3–7,18–20]. The striped patterns are understood, in isotropic systems, as the stable equilibrium of a single mode [3–5,18]. The direction of this pattern depends on the initial condition. Likewise, the square, hexagonal, and superlattice patterns are understood as stable equilibria between two, three, and several resonant modes, respectively [3–5,18,21]. Labyrinthine patterns are understood as a stable equilibrium of many disordered phase critical modes with similar wave numbers and magnitude of the amplitude. The labyrinths are locally dominated by a single mode [19]. Quasicrystals result from higher codimensional instabilities that include modes of different wavelengths [3–6,22]. Patterns with many coherent phase modes with the same wavelength and amplitude can generate concentric ring patterns (see Fig. 1). Patterns with concentric rings are observed in vegetation [23], fluid convection [24], molecular assembling [25], suspended liquid crystal films [26], laser irradiation at the solid/liquid interface [27], gas-discharge systems [28], bacteria colony formation [29], optically pumped semiconductor amplifiers [30], electroexplosion in a needle iron metal plate [31], evaporation-assisted formation of surface patterns [32], evaporation of colloidal nanoparticles in a confined cell [33], the far field of a photorefractive oscillator [20], and the photoisomerization process in liquid crystals [34]. Although concentric ring patterns are observed in various physical systems, they are unstable from the point of view of amplitude equations [35,36]. Therefore, the mechanism of origin of these patterns and their properties is not established.

This Letter aims to show that concentric ring patterns are stable beyond Turing instability, in the sense that the phenomenon occurs after (or before) a Turing instability, but not at the onset. Based on a prototype mathematical model of pattern formation, we show that these solutions are stable and identify the necessary ingredients for their stability.

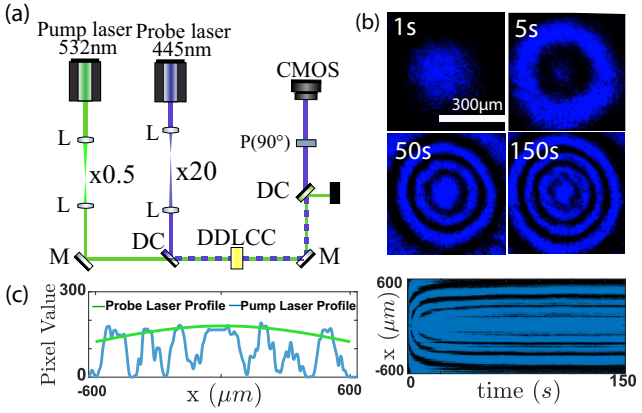

FIG. 1. Experimental observation of concentric ring patterns in a dye-doped liquid crystal sample under the effect of two parallel coherent beams. (a) Schematic representation of the experimental setup. A dye-doped liquid crystal cell (DDLCC) is irradiated by a 445-nm blue laser (BL, probing light beam) and illuminated by a 532-nm green laser (GL, excitation light beam). L, M, DC, and P account for lens, mirrors, dichroic crystals, and polarizer, respectively. DDLCC is monitored by a CMOS camera. (b) A horizontal cut of the spatiotemporal evolution (bottom panel) of an illuminated dye-doped liquid crystal cell. Panels show a temporal sequence of snapshots of the DDLCC cell. (c) Horizontal profile of the equilibrium concentric ring pattern.

Concentric ring patterns are observed in the region of bistability between uniform states and patterns. Close to Turing instability, when unstable concentric rings are forming, they are characterized by spreading so that the outer concentric rings aggregate. However, in the region where concentric ring patterns are stable, propagation is characterized by rings emerging from the center and pushing the ring structure. Hence, the propagation mechanisms of the modulated front are completely different. Notice that front propagation in both cases is controlled by curvature. Experimentally, we observe stable concentric ring patterns in an illuminated dye-doped liquid crystal cell with sufficiently high intensity. The formation and spread of the concentric rings are consistent with our theoretical findings.

Experimental setup and observations. Out-of-equilibrium liquid crystals exhibit complex spatial textures [37]. Traditional methods to keep liquid crystals out of equilibrium are the application of electric and magnetic fields, and thermal gradients. Likewise, they can be kept out of equilibrium with strong electromagnetic fields. In addition, a nonintense light beam can be used to drive liquid crystals out of equilibrium. To do this, liquid crystals can be doped with photosensitive molecules [38], which can change their molecular structure upon receiving a photon with a particular frequency (photoisomerization). In turn, the rotations of these light-sensitive molecules cause the oriented molecules of the liquid crystal to become disordered. Patterns induced by photoisomerization have been observed in a dye-doped nematic liquid crystal layer. This type of self-organization has been modeled by a reaction-diffusion system [34,39,40].

To study concentric ring patterns, we consider a dye-doped liquid crystal cell (DDLCC) under the effect of two parallel coherent beams at room temperature (18 °C). The sample is only photosensitive to one beam (excitation beam), and at the same time, the other is harmless (probing beam). Figure 1 illustrates the experimental setup diagram. The DDLCC undergoes a phototropic transition when it is irradiated by a light source in the absorption band of the guest dye [38]. We used a concentration of methyl red 0.5 wt % as the azo-dye guest doping a commercially available E7 nematic liquid crystal (host). The mixture was inserted into an antiparallel planar-aligned liquid crystal cell with a thickness of 25 μm (Instec). A 532-nm Verdi V-2 (Coherent) and 445-nm Cobolt 90 mW polarized laser were used as an exciting and probing irradiation light source to generate and observe a phototropic transition, respectively. Note that the green laser wavelength was close to the absorbance peak at 496 nm of the mixture, enabling us to trigger the isomerization and increase the amount of *cis* methyl red isomer. Two Kepler telescopes with a magnification of 0.5× and 20× were used to change the waist of the green and blue laser, respectively. A dichroic crystal (DC, high and low bandpass) is used to separate both beams and to monitor the DDLCC with a complementary metal-oxide-semiconductor (CMOS) camera. Before the CMOS camera, a polarizer was placed orthogonal to the polarization of the blue laser.

The camera displays a dark cell due to the polarizer when the DDLCC is illuminated with a blue probing light. When illuminating with the green laser with a power of the order of 300 mW (a waist of 0.56 mm), we initially observe a lightened circular area [see Fig. 1(b) at 1 s], which is later accompanied by a central circular dark spot that afterward becomes a dark propagating ring [see Fig. 1(b) at 5 s]. Then, a second spot appears in the center, which in turn becomes in another propagative ring. This process continues until four dark rings are established [see Fig. 1(b) at 150 s, and the video in the Supplemental Material [41]]. The lower panel of Fig. 1(b) summarizes the spatiotemporal evolution of the observed photoisomerization dynamics. Because the illuminated area is a Gaussian region, the ring patterns eventually stop, giving rise to a bull's-eye shape [cf. Fig. 1(b) at 150 s]. Figure 1(c) shows the horizontal profile of the equilibrium concentric ring pattern.

Theoretical descriptions. A prototype model of pattern formation is the Swift-Hohenberg equation [42], which is an isotropic, reflection symmetry, and real order parameter nonlinear equation deduced originally to describe the pattern formation on Rayleigh-Bénard convection [42]. This equation applies to a wide range of systems that undergo a spatial symmetry-breaking instability—often called Turing instability [2–4]—close to a second-order critical point marking the onset of a hysteresis loop, which corresponds to a Lifshitz point [4]. The Swift-Hohenberg equation reads

$$\partial_t u = \epsilon u - u^3 - \nu \nabla^2 u - \nabla^4 u, \tag{1}$$

where $u = u(x, y, t)$ is a real scalar field, x and y are spatial coordinates, and t is time. Depending on the context in which this equation has been derived, the physical meaning of the scalar field $u = u(x, y, t)$ could be the electric field, deviation of molecular orientations, phytomass density, or chemical concentration, among others. The control or bifurcation parameter ϵ measures the input field amplitude, the

aridity parameter, or the chemical concentration. The parameter ν stands for the diffusion coefficient ($\nu < 0$); when this parameter is positive ($\nu > 0$), it induces an antidiffusion process, which is characterized by the emergence of patterns with a characteristic wavelength.

For sufficiently negative ϵ, the only stable state of this model Eq. (1) is the zero solution $u = 0$. When ϵ is increased or exceeds the critical value $\epsilon_{c1} = -\nu^2/4$, it exhibits a supercritical spatial instability (Turing instability) [3,4], which gives rise to stable stripe patterns with a $\sqrt{\nu/2}$ wave number. The zero unstable state presents a secondary instability for $\epsilon = 0$, giving rise to two new homogeneous uniform states $\pm\sqrt{\epsilon}$, which stabilize for $\epsilon = \epsilon_{c2} \equiv \nu^2/8$. Then, for $\epsilon > \epsilon_{c2}$, the system presents bistability between the uniform solutions $\pm\sqrt{\epsilon}$ and the pattern states. Figure 2(e) depicts the bifurcation diagram of the Swift-Hohenberg equation (1). Numerically, we have considered the uniform state $-\sqrt{\epsilon}$, and we have perturbed it locally with a Gaussian [with a width of the pattern wavelength—see Fig. 2(d)]. Depending on ϵ, we observe different behaviors. In the region where uniform states are unstable ($\epsilon_{c1} \leqslant \epsilon \leqslant 0$), we observe the propagation of unstable concentric rings [cf. Fig. 2(a)] [24]. This propagation is characterized by the appearance of outer rings that are attached. When ϵ is increased, the previous scenario changes. We observe similar propagation, but of stable concentric ring patterns. In Fig. 2(e), we have characterized the parameter space where this behavior is observed and called it *outside ringing*. Further increasing ϵ, and the system being in the bistability region, propagation is characterized by rings emerging from the center and pushing the concentric ring structure [see Fig. 2(b)]. We have termed this region *inside ringing*. When ϵ is increased even more, the system does not exhibit the formation of a concentric ring pattern, but rather the propagation of one homogeneous state over the other. We have named this region *inflation* [cf. Fig. 2(c)]. Further increasing ϵ, the initial perturbation stabilizes in a localized structure [see Fig. 2(d)]. In addition, we have considered numerical simulations in a circular geometry to avoid edge effects, and study the stability of concentric ring patterns. The lower panels (I) and (II) of Fig. 2(e) show stable concentric ring patterns. Note that stable concentric ring patterns are observed beyond Turing instability ($\epsilon > \epsilon_{c1}$, $\epsilon < \epsilon_{c2}$, and $\epsilon > \epsilon_{c2}$). This could be related to a shift of the Turing boundary due to the axisymmetric (radial) restriction on the initial condition. Numerical simulations were conducted with the Runge-Kutta fourth-order algorithm for time integration and a finite-difference scheme for spatial discretization.

To shed light on concentric ring patterns, we consider a one-dimensional model that contains the necessary ingredients (curvature, bistability, and a characteristic wavelength) to observe these patterns and their dynamics. Considering that patterns are rotation invariant, we can propose the following ansatz $u(x, y, t) = u(r, t)$, where r is the radial coordinate. Thus, Eq. (1) reads

$$\partial_t u = \epsilon u - u^3 - \nu\left(\partial_{rr} + \frac{\partial_r}{r}\right)u - \left(\partial_{rrrr} + 2\frac{\partial_{rrr}}{r} - 2\frac{\partial_{rr}}{r^2} + \frac{\partial_r}{r^3}\right)u, \qquad (2)$$

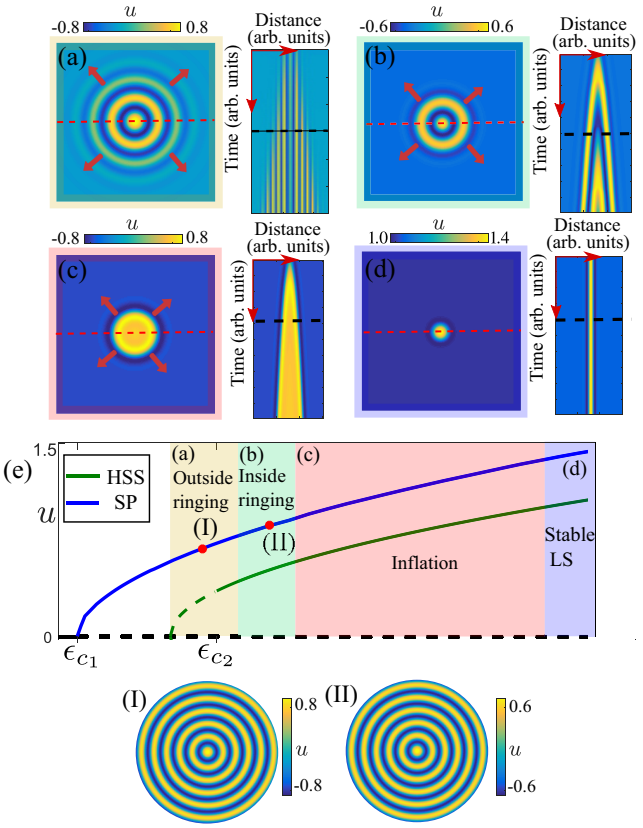

FIG. 2. Numerical observations of concentric ring patterns in the Swift-Hohenberg Eq. (1) for $\nu = 1$. Different concentric ring patterns are observed considering the homogeneous state $-\sqrt{\epsilon}$ and perturbing it with a small Gaussian. (a) Outside ringing: The pattern propagation is characterized by the appearance of attached outer rings. (b) Inside ringing: The pattern propagation is characterized by rings emerging from the center and pushing the concentric ring structure. (c) Inflation: Front propagation of one homogeneous state over the other. (d) Stable localized structures. The right panels illustrate the spatiotemporal evolution of the middle line in the two-dimensional simulations (segmented red line). The left panels depict the surface plots obtained at the instant represented by the black dashed line on the spatiotemporal diagram. (e) Bifurcation diagram of the Swift-Hohenberg Eq. (1): Maximum value of u vs ϵ. The green line corresponds to the uniform state $\sqrt{\epsilon}$ (HSS, homogeneous steady state), the blue curve stands for stripe patterns (SP), and the black line represents the zero solution. Segmented and solid lines indicate that the corresponding state is unstable and stable, respectively. The lower panels (I) and (II), which correspond to the red solid circles, show stable concentric ring patterns.

which is a one-dimensional Swift-Hohenberg model with curvature corrections inherent to two dimensions. The curvature effects are controlled by the terms proportional to the inverse of a power of r in Eq. (2). This model has uniform solutions $\mu = \{0, \pm\sqrt{\epsilon}\}$ and one-dimensional patterns. Note that these patterns correspond to concentric ring states. $\epsilon = \epsilon_{c1} = -\nu^2/4$ accounts for the Turing instability (supercritical spatial instability) for Eq. (2) [3,4]. In the case when one ignores the curvature effects (standard one-dimensional Swift-Hohenberg model), patterns propagate through the emergence of spatial

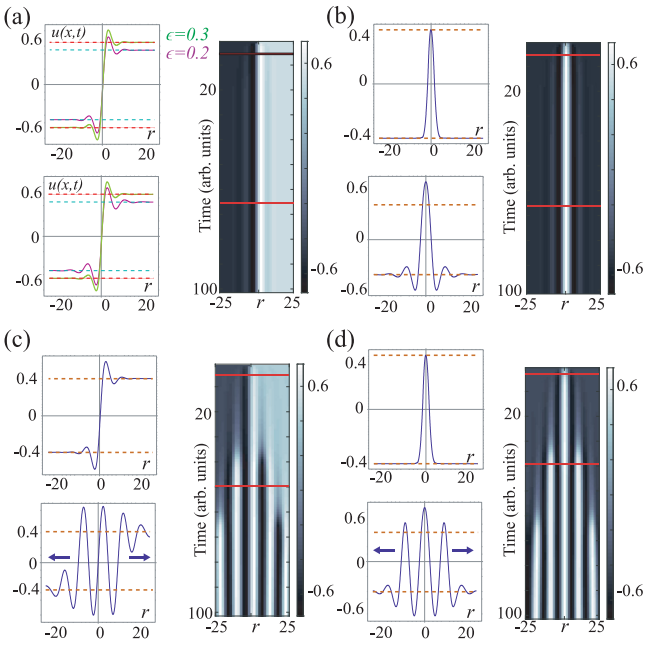

FIG. 3. Domain walls and localized structures of the one-dimensional Swift-Hohenberg Eq. (2) for $\nu = 1$, and without curvature corrections. (a) Domain wall profile and spatiotemporal evolution between symmetrical uniform states $u = \pm\sqrt{\epsilon}$ for $\epsilon = \{0.2, 0.3\}$. (b) Profiles of localized structures and spatiotemporal evolution ($\epsilon = 0.2$). (c) Pattern propagation from a domain wall solution ($\epsilon = 0.15$) or a (d) localized structure ($\epsilon = 0.15$). The red lines on the spatiotemporal diagram show the instant where the profiles are obtained. The dashed horizontal lines account for the homogeneous equilibria. The domain of integration is from $r = -25$ to $r = 25$.

oscillations at the end of the pattern. Figure 3 illustrates pattern propagation in the absence of curvature, by integrating Eq. (2) in the whole spatial range (negative and positive values of r). This behavior is similar to that observed in concentric ring patterns in two dimensions in the outside ringing region; see Fig. 2(e). We consider ϵ in the region of bistability between uniform and pattern states. In this parameter region, the system has a domain wall solution that connects two symmetric states [see Fig. 3(a)]. The damped spatial oscillation amplitudes increase with ϵ. Likewise, the model Eq. (2), without curvature effects, has localized structures, for higher values of ϵ, supported by homogeneous states [see Fig. 3(b)]. For lower values of ϵ, the pattern state becomes more stable than the homogeneous one. Then, the pattern begins to propagate from the domain wall center or from the localized structure [see the bottom panels of Figs. 3(c) and 3(d), respectively].

The above scenario changes radically when one considers the curvature effects. Starting from a localized structure in the center of the numerical integration domain, for ϵ in the outside ringing region, we observe pattern propagation through the emergence of spatial oscillations outside the pattern [see Fig. 4(a)], as in the case without curvature effects. However, by increasing ϵ (inside ringing region), the propagation changes drastically. Now, spatial oscillations created in the center of the integration domain drive the propagation, which propagates outward, and subsequently gives rise to new

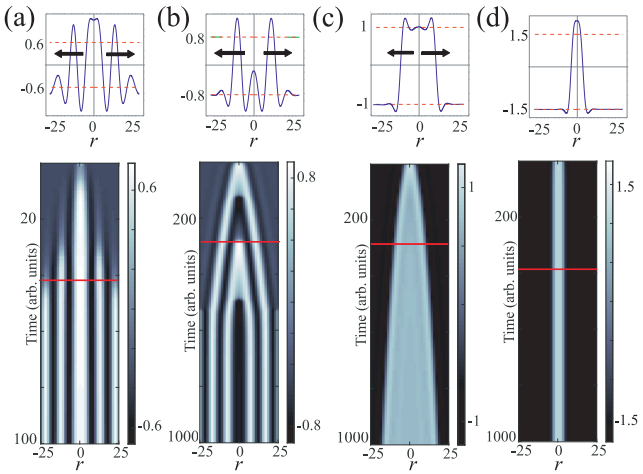

FIG. 4. Pattern propagation and profiles from a localized structure of the one-dimensional Swift-Hohenberg model Eq. (2) for $\nu = 1$. (a) Pattern propagation for $\epsilon = 0.1$ by including spatial oscillations in the outer part of the pattern. (b) Pattern propagation for $\epsilon = 0.2$ characterized by spatial oscillations that emerge from the center and push the pattern structure outward. (c) Front propagation of one homogeneous state over the other, for $\epsilon = 0.5$. (d) Stable localized structures for $\epsilon = 0.9$. The red lines on the spatiotemporal diagrams show the instant where the profiles are obtained. The dashed horizontal lines account for the homogeneous equilibria. The domain of integration is from $r = 0$ to $r = 25$, and then reflected at $r = 0$.

oscillations in the center [cf. Fig. 4(b)]. This type of propagation is similar to the one observed experimentally [see Fig. 1(b)]. When ϵ is increased even more, we observe, as a consequence of the curvature, that one homogeneous state invades the other as illustrated in Fig. 4(c). Notice that the speed of the fronts is constantly decelerating. This observed dynamical behavior is consistent with what we have called the inflation region in Fig. 2(e). By further increasing ϵ, the localized structure is stable, and propagation of patterns or homogenous states is not observed [see Fig. 4(d)]. The solutions of Eq. (2) shown in Fig. 4 were numerically integrated for $r > 0$, and then reflected at $r = 0$. In brief, the effects of curvature and bistability (uniform and pattern state) control and stabilize the propagation mechanisms of concentric ring patterns. The transition between the *inflation* mode and a stationary localized structure has been reported in a previous work [43]. There, a Swift-Hohenberg model was used to explore the phase domain dynamics. By a minimization principle, a local velocity-curvature relationship was proposed. Note that in the cases of *inside* and *outside* ringing [cf. Fig. 2(e)], the local approximation is invalid, and the ring dynamics is governed by nonlocal interactions.

In conclusion, we have shown that concentric ring patterns are stable beyond Turing instability. To observe these concentric ring patterns, the bistability of patterns and homogeneous states in an isotropic medium is required. Based on a prototype model, the Swift-Hohenberg equation, we show that these solutions are stable and identify the ingredients for their stability. Close to the Turing instability, the concentric rings are unstable due to the interaction of spatial modes. Then, beyond the Turing instability, the concentric ring

patterns can be stabilized. We propose a mechanism of pattern formation, inside ringing, which is triggered by curvature. Experimentally, we observed stable concentric ring patterns in an illuminated dye-doped liquid crystal cell with sufficiently high intensity. The formation of the concentric ring patterns is in agreement with our theoretical findings in the inside ringing region.

The authors are thankful for fruitful discussions with P. I. Hidalgo, J. Vergara, and G. González-Cortés. The authors are thankful for the financial support of ANID-Millenium Science Initiative Program–ICN17_012 (MIRO) and FONDECYT Project No. 1210353. S.E.-A. acknowledges the financial support from ANID by Beca Doctorado Nacional 2020-21201376.

[1] P. Glansdorff and I. Prigogine, *Thermodynamic Theory of Structures. Stability and Fluctuations* (Wiley, New York, 1971).
[2] G. Nicolis and I. Prigogine, *Self-Organization in Nonequilibrium Systems* (Wiley, New York, 1977).
[3] L. M. Pismen, *Patterns and Interfaces in Dissipative Dynamics* (Springer, Berlin, 2006).
[4] M. Cross and H. Greenside, *Pattern Formation and Dynamics in Non-Equilibrium Systems* (Cambridge University Press, New York, 2009).
[5] R. B. Hoyle, *Pattern Formation: An Introduction to Methods* (Cambridge University Press, Cambridge, U.K., 2006).
[6] F. T. Arecchi, S. Boccaletti, and P. Ramazza, Pattern formation and competition in nonlinear optics, Phys. Rep. **318**, 1 (1999).
[7] J. D. Murray, *Mathematical Biology* (Springer, New York, 1990).
[8] P. Coullet, T. Frisch, and F. Plaza, Sources and sinks of wave patterns, Physica D **62**, 75 (1993).
[9] P. Coullet, D. Daboussy, and J. R. Tredicce, Optical excitable waves, Phys. Rev. E **58**, 5347 (1998).
[10] T. Frisch, S. Rica, P. Coullet, and J. M. Gilli, Spiral Waves in Liquid Crystal, Phys. Rev. Lett. **72**, 1471 (1994).
[11] P. Coullet, S. Fauve, and E. Tirapegui, Large scale instability of nonlinear standing waves, J. Phys. Lett. **46**, 787 (1985).
[12] A. Turing, The chemical basis of morphogenesis, Philos. Trans. R. Soc. B **237**, 37 (1952).
[13] S. A. Akhmanov, M. A. Vorontsov, and V. Yu. Ivanov, Large-scale transverse nonlinear interactions in laser beams - New types of nonlinear waves, generation of "optical turbulence", Pis'ma Zh. Eksp. Teor. Fiz. **47**, 611 (1988).
[14] S. A. Akhmanov, M. A. Vorontsov, V. Yu. Ivanov, A. V. Larichev, and N. I. Zheleznykh, Controlling transverse-wave interactions in nonlinear optics: generation and interaction of spatiotemporal structures, J. Opt. Soc. Am. B **9**, 78 (1992).
[15] N. N. Rosanov, *Spatial Hysteresis and Optical Patterns* (Springer, Berlin, 2002).
[16] K. Staliunas and V. J. Sanchez-Morcillo, *Transverse Patterns in Nonlinear Optical Resonators* (Springer, Berlin, 2003).
[17] M. Tlidi, K. Staliunas, K. Panajotov, A. G. Vladimirov, and M. G. Clerc, Localized structures in dissipative media: from optics to plant ecology, Philos. Trans. R. Soc. A **372**, 20140101.
[18] A. C. Newell, T. Passot, and J. Lega, Order parameter equations for patterns, Annu. Rev. Fluid Mech. **25**, 399 (1993).
[19] S. Echeverría-Alar and M. G. Clerc, Labyrinthine patterns transitions, Phys. Rev. Res. **2**, 042036(R) (2020).
[20] K. Staliūnas, G. Šlekys, and C. O. Weiss, Nonlinear Pattern Formation in Active Optical Systems: Shocks, Domains of Tilted Waves, and Cross-Roll Patterns, Phys. Rev. Lett. **79**, 2658 (1997).
[21] A. O. Leon, M. G. Clerc, and S. Coulibaly, Dissipative structures induced by spin-transfer torques in nanopillars, Phys. Rev. E **89**, 022908 (2014).
[22] M. C. Walters, P. Subramanian, A. J. Archer, and R. Evans, Structural crossover in a model fluid exhibiting two length scales: Repercussions for quasicrystal formation, Phys. Rev. E **98**, 012606 (2018).
[23] R. Berg, Age determination of eels, *Anguilla anguilla* (L): comparison of field data with otolith ring patterns, J. Fish Biol. **26**, 537 (1985).
[24] Y. Hu, R. E. Ecke, and G. Ahlers, Behavior of Focus Patterns in Low Prandtl Number Convection, Phys. Rev. Lett. **72**, 2191 (1994).
[25] H. Maeda, An Atomic Force Microscopy Study of Ordered Molecular Assemblies and Concentric Ring Patterns from Evaporating Droplets of Collagen Solutions, Langmuir **15**, 8505 (1999).
[26] D. R. Link, L. Radzihovsky, G. Natale, J. E. Maclennan, N. A. Clark, M. Walsh, S. S. Keast, and M. E. Neubert, Ring-Pattern Dynamics in Smectic-C^* and Smectic-C^*_A Freely Suspended Liquid Crystal Films, Phys. Rev. Lett. **84**, 5772 (2000).
[27] K. Katayama, H. Yonekubo, and T. Sawada, Formation of ring patterns surrounded by ripples by single-shot laser irradiation with ultrashort pulse width at the solid/liquid interface, Appl. Phys. Lett. **82**, 4244 (2003).
[28] E. L. Gurevich, A. L. Zanin, A. S. Moskalenko, and H.-G. Purwins, Concentric-Ring Patterns in a Dielectric Barrier Discharge System, Phys. Rev. Lett. **91**, 154501 (2003).
[29] H. Shimada, T. Ikeda, J. Wakita, H. Itoh, S. Kurosu, F. Hiramatsu, M. Nakatsuchi, Y. Yamazaki, T. Matsuyama, and M. Matsushita, Dependence of local cell density on concentric ring colony formation by bacterial species Bacillus subtilis, J. Phys. Soc. Jpn. **73**, 1082 (2004).
[30] S. Barbay, Y. Ménesguen, X. Hachair, L. Leroy, I. Sagnes, and R. Kuszelewicz, Incoherent and coherent writing and erasure of cavity solitons in an optically pumped semiconductor amplifier, Opt. Lett. **31**, 1504 (2006).
[31] Vandana and P. Sen, Concentric ring patterns in needle-plate exploding systems, J. Phys.: Condens. Matter **19**, 016009 (2007).
[32] W. Sun and F. Q. Yang, Evaporation-assisted formation of surface patterns from polymer solutions via copper tubes, Express Polym. Lett. **12**, 699 (2018).
[33] V. K. Vlasko-Vlasov, M. Sulwer, E. V. Shevchenko, J. Parker, and W. K. Kwok, Ring patterns generated by an expanding colloidal meniscus, Phys. Rev. E **102**, 052608 (2020).
[34] M. G. Clerc, G. Gonzalez-Cortes, P. I. Hidalgo, L. A. Letelier, M. J. Morel, and J. Vergara, Light-induced ring pattern in a dye-doped nematic liquid crystal, Appl. Sci. **11**, 5285 (2021).

[35] D. Lloyd and B. Sandstede, Localized radial solutions of the Swift-Hohenberg equation, Nonlinearity **22**, 485 (2009).

[36] C. Castillo-Pinto, M. G. Clerc, and G. González-Cortés, Extended stable equilibrium invaded by an unstable state, Sci. Rep. **9**, 15096 (2019).

[37] I. Dierking, *Textures of Liquid Crystals* (Wiley-VCH, Weinheim, 2003).

[38] I. C. Khoo, *Liquid Crystals* (Wiley, Hoboken, NJ, 2007).

[39] I. Andrade-Silva, U. Bortolozzo, M. G. Clerc, G. Gonzalez-Cortes, S. Residori, and M. Wilson, Spontaneous light-induced Turing patterns in a dye-doped twisted nematic layer, Sci. Rep. **8**, 12867 (2018).

[40] I. Andrade-Silva, U. Bortolozzo, C. Castillo-Pinto, M. G. Clerc, G. Gonzalez-Cortes, S. Residori, and M. Wilson, Dissipative structures induced by photoisomerization in a dye-doped nematic liquid crystal layer, Philos. Trans. R. Soc. A **376**, 20170382 (2018).

[41] See Supplemental Material at http://link.aps.org/supplemental/10.1103/PhysRevResearch.5.L012007 for a video showing the emergence and pattern of concentric rings observed in a dye-doped liquid crystal cell illuminated with two parallel light beams.

[42] J. Swift and P. C. Hohenberg, Hydrodynamic fluctuations at the convective instability, Phys. Rev. A **15**, 319 (1977).

[43] K. Staliunas and V. J. Sanchez-Morcillo, Dynamics of phase domains in the Swift-Hohenberg equation, Phys. Lett. A **241**, 28 (1998).